University of Alberta

MICROPHOTONIC DEVICE FABRICATION IN SILVER PHOTODOPED CHALCOGENIDE GLASSES AND POLYMERS

by

Mahesh M. Pai 

A thesis submitted to the Faculty of Graduate Studies and Research in partial fulfillment of the requirements for the degree of **Master of Science**.

Department of Electrical and Computer Engineering

Edmonton, Alberta
Spring 2006

Your file Votre référence
ISBN: 0-494-13868-8
Our file Notre référence
ISBN: 0-494-13868-8

To
Amma, Appa, Majukki, Santhamav
and
Sarvamam

Abstract

On-chip optical interconnects and microcavity based filters are believed to be critical enablers for multifunctional integrated optics. It is well known that the key for realizing high density chip-scale integrated optical components lies in high-index contrast material systems. Chalcogenide glasses possess many qualities that make them well suited to chip-scale integrated optic systems, and are potentially compatible with the commercial CMOS technology. This work investigates the fabrication of high-index contrast structures in chalcogenide glasses by exploiting their ability to dissolve silver under illumination. The etch resistivity exhibited by silver doped chalcogenide glass is utilized for realizing strip waveguides. High-performance commercial polymer (polyamide-imide) was investigated as a core material for polymer based high-index contrast waveguides. Another partially realized goal of this thesis was to fabricate micro-ring resonators based on chalcogenide glasses and compatible polymers. A controllable stress related buckling phenomenon observed during silver photodoping of $Ge_{33}As_{12}Se_{55}$ glass is also reported.

Acknowledgements

First, I would like to thank my advisor, Dr. Ray DeCorby, for providing me this opportunity to explore the nuances of integrated optics. His level of patience, perseverance and good nature is something I will always strive to attain and keep up.
A big thank you goes to Nakeeran Ponnampalam with his never-say-die philosophy. From paying my damage deposit to burning the midnight oil with me on device characterizations, he has been a big brother figure for me. I would like to thank Hue Nguyen for her help in the Nanofab and all the snacks that used appear on my desk from time to time. I have enjoyed working with Thomas Clement and Trevor Allen, and also enjoyed their good company. Many thanks goes to my buddies Piotr Kursa and Andrzej Tomalik for introducing me to the great Canadian outdoors, skiing, skating, perogies and tons of sushi.
From a well equipped lab to the opportunity to interact with fellow students from diverse backgrounds, the financial assistance and the environment at TRLabs Edmonton has been truly exceptional. I have always gained new insights from every interactions I have had with David Clegg, laboratory manager at TRLabs Edmonton. I would also like to thank Ahmed Allam, one of the 'pillars', for the squash encounters, cooking lessons and especially for sparking my interest in RF.
Last but not the least I would like to thank Amma, Appa, Manjukki, Santhamav and Sarvamam for their love and support.

Contents

List of Tables

List of Figures

List of Symbols

As_2Se_3	Arsenic Triselenide
β	Propagation constant
c_0	Speed of light in vacuum
c	Speed of light in a medium
CMOS	Complementary Metal-Oxide Semiconductor
CWDM	Coarse Wavelength Division Multiplexing
DMAc	N,N-Dimethylacetamide
DWDM	Dense Wavelength Division Multiplexing
E	Electric Field
EIM	Effective index method
ε_0	Electric Permittivity in vacuum
ε_r	Relative Electric Permittivity in a medium
FSR	Free spectral range
FWHM	Full width half maximum
H	Magnetic Field
ICPRIE	Inductively Coupled Reactive Ion Etch
IG2	$Ge_{33}As_{12}Se_{55}$
IG5	$Ge_{28}Sb_{12}Se_{60}$
ITU	International Telecommunication Union
k_0	Wave number
κ	Transverse wave vector
λ	Wavelength
MEA	Monoethanolamine
MFD	Mode field diameter

MMI	Multi-mode interference
μ_0	Magnetic Permeability in vacuum
μ_r	Relative Magnetic Permeability in a medium
n	Refractive Index
∇^2	Laplacian operator
OADM	Optical Add-Drop Multiplexer
ω	Angular Frequency
PAI	Polyamide-imide
PLD	Pulsed laser deposition
PMMA	Polymethylmethacrylate
Q	Quality Factor
RIE	Reactive Ion Etch
RMS	Root mean square
TDM	Time Division Multiplexing
TE	Transverse Electric
TM	Transverse Magnetic
TMAH	Tetra-methyl ammonium hydroxide
WDM	Wavelength Division Multiplexing

Chapter 1

Introduction

This chapter gives a brief background and motivation for the work that is described in this thesis. An outline of the thesis is also provided.

1.1 Brief history of Optics in Communication

The 20^{th} century saw the discovery of semiconductors, and their subsequent use as transistors heralded a new era in electronics. Complex electronic circuits could now be realized on a small planar substrate using microfabrication technology. Further improvements in integrated circuit technology made microprocessors affordable thereby making powerful computers accessible to the masses. As the number of computers grew around the world, so did the need for information sharing. Offices across continents needed to be interlinked. Copper cables couldn't support this increase in data rates and also the economics of laying cables was overwhelming. Not only did optical fibers provide a cost-effective alternative to traditional copper telephone lines but they also future-proofed the bandwidth requirement for applications like video conferencing, music streaming etc.

There are two main components in a telecommunication network: fiber that transmits the data and routers that direct the incoming data to its appropriate destination. In an optical fiber, data is transmitted in specific wavelength bands that are specified by the International Telecommunication Union (ITU) (refer to Table 1.1). S, C and L wavelength bands are the most commonly used for long haul fiber optic networks.

Table 1.1: ITU classified wavelengths for fiber optic communication[1]

Band	Descriptor	Wavelength Range (nm)
O	Original	1260-1360
E	Extended	1360-1460
S	Short	1460-1530
C	Conventional	1530-1565
L	Long	1565-1625
U	Ultra Long	1625-1675

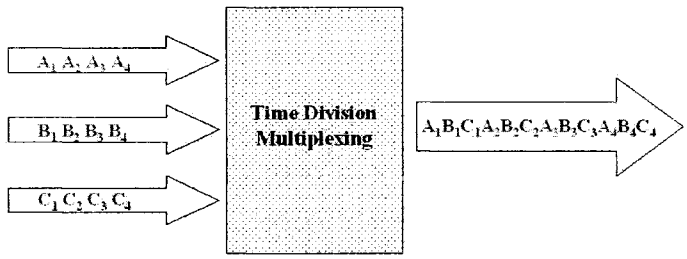

Figure 1.1: Time Division Multiplexing (TDM)

In a fiber optic network there are two common multiplexing methodologies used to increase capacity and utilize the available bandwidth efficiently. These are Time Division Multiplexing (TDM) and Wavelength Division Multiplexing (WDM). In TDM several slower data streams are combined into a single high-speed data stream to be transmitted over a single fiber link. This is shown in Figure 1.1. By conveying information about the time slot that a particular signal occupies the signal can be retrieved at the destination. The transmission order needs to be maintained to reassemble the input streams at the destination.

As opposed to allotting a time slot for each signal in TDM, signals are assigned a wavelength in WDM. WDM allows many signals to be sent over a single fiber link, each using a different wavelength. Figure 1.2 illustrates the WDM methodology. Hence all the signals coexist at the same time but on separate wavelength. Unlike TDM, each of the signals in WDM can use completely different protocols and bit rates on the same fiber.

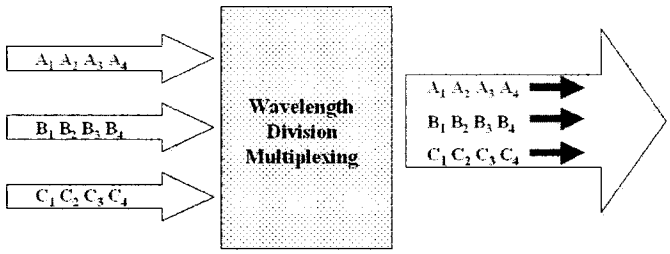

Figure 1.2: Wavelength Division Multiplexing

1.2 Importance of Wavelength Filtering

In WDM, we can increase the capacity of a fiber optic link by increasing the usable wavelength range or decreasing the spacing between two adjacent channels. The first method is very much dependant on the material properties of the fiber that has already been installed. For example, Figure 1.3 shows the fiber attenuation and the water peaks (E-band) rendering the band available for long haul communication discontinuous. The second method squeezes in more channels and thus increasing the capacity. Hence, depending on how many channels are in a particular communication band (for example, the C band), WDM can be termed as Coarse Wavelength Division Multiplexing (CWDM) or Dense Wavelength Divigion Multiplexing (DWDM).

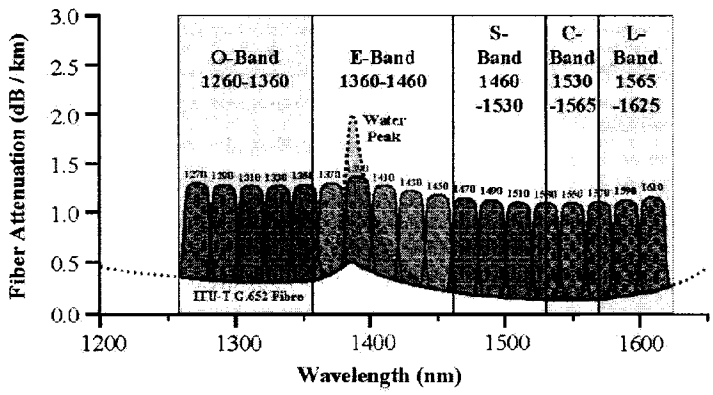

Figure 1.3: ITU-T G.694.2 CWDM Grid and fiber loss (dotted line) [2]

CWDM delivers 17-18 channels spanning all the optical communication bands with spacing of 20 nm between them. This is a big number for channel spacing, accommodating the use of lasers diodes and broadband filters without temperature stabilization. These CWDM wavelengths are standardized as per the ITU grid specifications.

DWDM on the other hand delivers hundreds of channels with a typical channel spacing of about 0.8 nm, thus giving many more densely spaced channels than CWDM and increasing the capacity of the fiber dramatically. DWDM thus demands higher tolerances on filter responses and temperature-stabilized wavelength control of laser diodes to avoid crosstalk. Typically on-off ratios for filter response (Figure 1.4) need to be more than 20 dB [7].

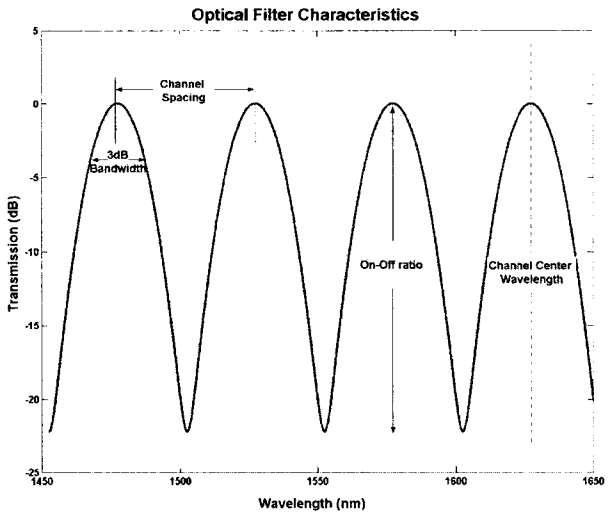

Figure 1.4: Optical filter characteristics

Hence, filters plays a pivotal role in any WDM system. Optical filters can be used for adding or dropping a channel, thus acting as an Optical Add-Drop Multiplexer (OADM). OADM is a more efficient and cheaper alternative to the optical-electrical-optical conversion method. Filters can also be used for wavelength stabilization of laser diodes [8, 9]. Active filters act as optical switches. These are some of the applications of filters in telecommunications. Outside the fiber optic networks realm, optical filters find a huge market in spectroscopy, imaging, high

sensitivity biosensors etc [10].

1.3 Need for high index contrast Integrated Optics

The optical component market faces hurdles similar to those the electronics industry faced before the invention of integrated circuits. Multifunctional optical components are essentially glued and packaged together. They are big and take enormous amounts of skilled labor and time, which in turn makes them very costly. Ways need to be found to mass-produce and lower the capital/operational costs associated with optics. This calls for monolithic, multi-functional integrated optics [11, 12].
High refractive index contrast is very crucial in making tight integrated optic waveguide bends and for achieving high density of integration and smaller footprint devices [11]. There are lots of tradeoffs involved with a high index contrast system. Even though high-index contrast systems allow lower bend radii while keeping the bend-losses tolerable, the losses due to sidewall roughness becomes a major issue. Fabricating single-mode waveguides in high-index contrast material systems also calls for sub-micron lithography and sophisticated etching processes. Even coupling light between two high index contrast devices is challenging and can necessitate novel techniques and the use of index matching and anti-reflecting coatings [13].

1.3.1 Optical Interconnects

The shrinking of transistor gate widths and increase in device speeds and density has made the task of on-chip communication through metal interconnects extremely challenging. Due to the bandwidth limitation of copper interconnects,there are now bottlenecks associated with on-chip data transfer rates [14]. On-chip interconnect delays dominates system performance and signals can take several clock cycles to traverse the whole chip. Hence faster of clocking electronic devices does not necessarily translate to overall higher performance. The heat generated by metal interconnects also compounds the problem for future high-speed electronic chips.
On-chip optical interconnects offer a very high capacity communication channel to

alleviate these problems. Optical global clock distribution architectures to reduce the electrical clock skew have been proposed [15]. On-chip optical waveguides will typically need to be 1 cm long and the fabrication process must be robust and compatible with Complementary Metal-Oxide Semiconductor (CMOS) technology to exploit the profitability of mass production [16].

In the quest for perfect materials to be used as on-chip optical interconnects, CMOS process compatibility and ability to achieve dimensions and density of present day metal interconnects are of utmost importance. To achieve high interconnect density the optical waveguides should be able to traverse sharp bends required for intra-chip communication channels. As mentioned, low loss sharp bends call for high index contrast material systems. High index will also allow for low crosstalk between two interconnects and improves the signal to noise ratio. However careful fabrication is required as scattering losses can be severe in high index contrast systems.

1.3.2 Add drop multiplexers based on micro-rings

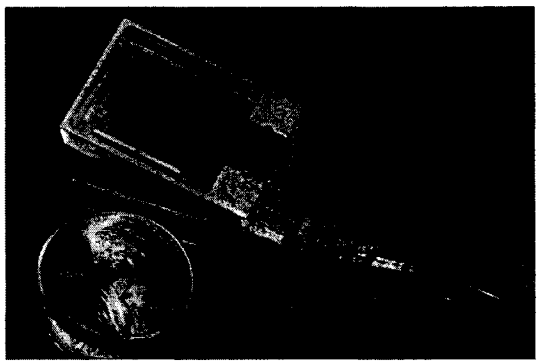

Figure 1.5: Commercial microring based 16 channel demultiplexer [3]

Add-drop multiplexers based on micro-ring resonators are believed to be a unique enabler for future integrated optics [17]. The main element is a ring, which is essentially a waveguide wrapped around itself to act as a traveling wave cavity. The bending radius determines the property of the micro-ring and also the wafer real estate consumed. As discussed above, the smaller the ring radius the higher the index contrast (and tighter mode confinement) required to minimize bend losses.

1.3.3 Photonic Crystals

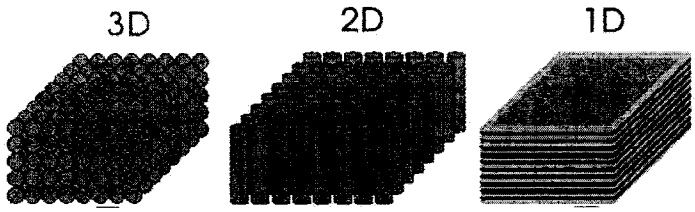

Figure 1.6: 1-D, 2-D and 3-D Photonic Crystal topology

Just as there are semiconductors that allow us to control electrons in many ways, we can also build an optical analog called the photonic crystal [18]. In semiconductors, electrons are forbidden to exist in certain energy bands. Similarly, in a photonic crystal, certain wavelengths of light are not allowed to exist inside the structure due to the periodic distribution of high and low index regions. The bands of wavelengths that are forbidden to exist are called the photonic band gaps.

Any defect, a discontinuity in the periodicity of the lattice, causes the light in the forbidden region to be trapped in the defect. The lattice constant or the periodicity is typically on the order of the wavelength of the light that is forbidden. Figure 1.6 shows the different photonic crystal configurations.

The potential applications for photonics crystals are numerous [19]. For example, low loss optical interconnects, right-angle bent waveguides [20], high quality factor (Q) microcavities, low threshold lasers and sensors [21] and highly dispersive superprisms [22] have been proposed.

1.4 Outline of the thesis

As discussed, the challenges that integrated optics faces are enormous. The task of synchronization, polarization and dispersion compensation among many others in future all optical integrated optic circuits is sure to be stimulating and worthwhile. Many of the underlying principles are well known, and exotic and complex systems built on micro-rings or photonic crystals have been proposed for chip-scale integrated optics. However, sophisticated and novel fabrication techniques are still required in order to make these a reality.

This goal of this work was to investigate novel fabrication methods and materials for high density integrated optics. Chalcogenide glasses and high performance polymers were the focus of the research. Both of these groups of materials hold potential for low temperature, back-end processing of integrated optics on chips. Further, when combined they provide high index contrast ($\delta n > 1$) and can potentially enable micron-scale bend radius in waveguide circuitry.

Chapter 2 and Appendix A provides the relevant theory and principles involved in integrated optics. Chapter 3 discusses the fabrication and characterization of high index contrast structures using As_2Se_3, $Ge_{33}As_{12}Se_{55}$ and $Ge_{28}Sb_{12}Se_{60}$ chalcogenide glasses. The silver photodoping technique that was used to realize strip waveguides in chalcogenide glasses is also described in Chapter 3. Chapter 4 discusses a unique stress related buckling phenomenon that was discovered during the photo-doping process in $Ge_{33}As_{12}Se_{55}$. Chapter 5 describes robust low loss high index contrast polyamide-imide (PAI) strip waveguides that were fabricated and characterized.

Finally, Chapter 6 gives observations and conclusions made in this work. Suggestions for future work are also made.

Appendix B details the mask made to study the buckling phenomenon described in Chapter 4.

Chapter 2

Background

This chapter describes the theory and basic principles involved in integrated optics in relation to the work presented in the subsequent chapters.

2.1 Integrated Optical Wavegudies

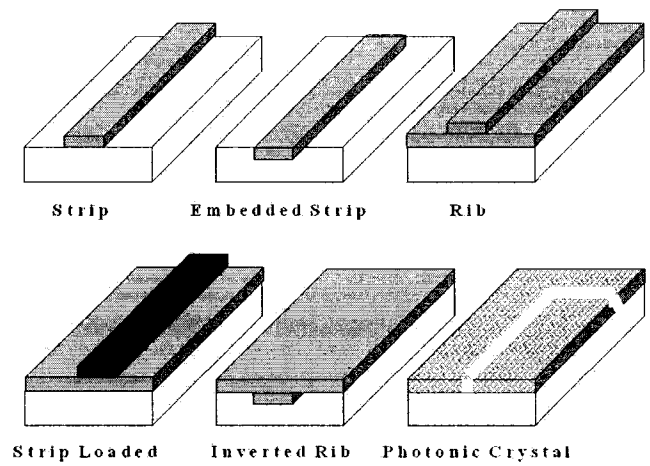

Figure 2.1: Different integrated optic waveguides

Some of the typical waveguide geometries used in integrated optics are shown in Figure 2.1. All of these, except the photonic crystal waveguide, guide light based on the total internal reflection phenomenon. Two common waveguide geometries are the strip and rib waveguide. A strip waveguide allows a tightly confined mode, allowing bends with lower losses compared to the rib waveguide geometry. How-

ever, the sidewall roughness related losses are larger in strip waveguides than in rib waveguides.

Solving the Maxwell's equations analytically is often non-trivial except for a few

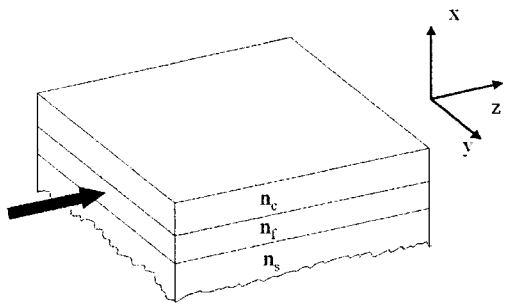

Figure 2.2: A slab waveguide showing the refractive indices ($n_f > n_s > n_c$) in each region.

simplified situations. The planar slab waveguide is one such structure and is a starting point for understanding light propagation in integrated optic waveguides (refer to Figure 2.2). We can solve the wave equation using appropriate boundary conditions. The wave equation that describes light propagation is given by:

$$\nabla^2 E - \frac{1}{c^2}\frac{\partial^2 E}{\partial^2 t} = 0 \tag{2.1}$$

$$\nabla^2 H - \frac{1}{c^2}\frac{\partial^2 H}{\partial^2 t} = 0 \tag{2.2}$$

Before we analyze a slab waveguide it should be noted that there are two possible orientations for the electric field with respect to the interface. When the electric field is perpendicular to the plane of incidence it is called a transverse electric (TE) wave. Similarly, when the magnetic field is perpendicular to the plane of incidence it is called a transverse magnetic (TM) wave.

2.1.1 Slab Waveguide

Let the light propagate along the positive z direction and let n_f, n_s and n_c be the film, substrate and cladding refractive indices respectively. Then, without loss of generality we can assume that $n_f > n_s > n_c$.

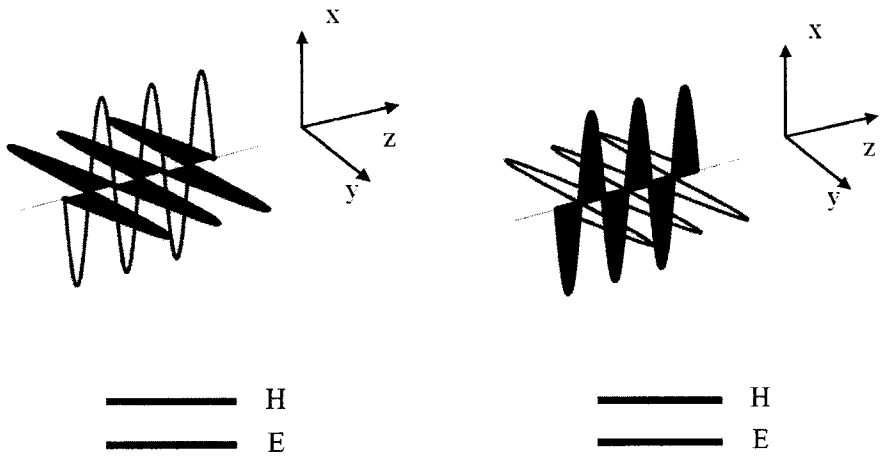

(a) TE polarized electromagnetic wave (b) TM polarized electromagnetic wave

Figure 2.3: TE and TM Polarized electromagnetic wave in a slab waveguide shown in Figure 2.2.

For a light wave which is TE polarized (refer to Figure 2.3(a)), the only non-zero component of the electric field can be expressed as:

$$E_y(x,z) = E_y(x)exp(-i\beta z) \tag{2.3}$$

Substituting the general solution given by equation 2.3 into the wave equation 2.1, we obtain

$$\frac{\partial^2 E_y}{\partial x^2} + (k_0^2 n_i^2 - \beta^2)E_y = 0 \tag{2.4}$$

where n_i is the refractive index in the region in consideration, $k_0(=\frac{2\pi}{\lambda})$ is the free space wavenumber and λ is the free space wavelength. This equation can be solved to get $E_y(x)$ given by

$$E_y(x) = E_0 exp(\pm\sqrt{\beta^2 - k_0^2 n_i^2}x) \tag{2.5}$$

$E_y(x)$ can be oscillatory or exponential depending on the sign of $\beta^2 - k_0^2 n_i^2$.
If $k_0 n_i > \beta$ then we can define a transverse wavevector κ as:

$$\kappa_i = \sqrt{k_0^2 n_i^2 - \beta^2} \tag{2.6}$$

As shown in Figure 2.4, β and κ are the longitudinal and transverse components of the wavevector k respectively.

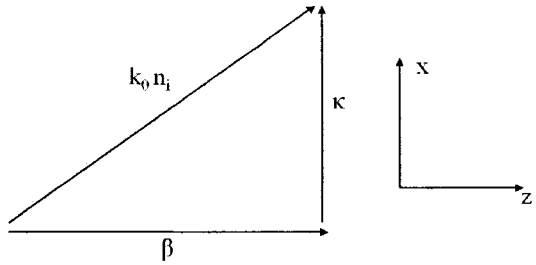

Figure 2.4: Components of Wave Vector

If the wave is to be guided in the core, the longitudinal wavevector β should satisfy the inequality $k_0 n_c < \beta < k_0 n_f$ or else the wave will escape out of the core into the cladding or substrate. Now that we have pinned down a range that β can take, it turns out that there are only discrete values that it can take.

Let the attenuation coefficient in the three regions be defined as $\gamma_i = \sqrt{\beta^2 - k_0^2 n_i^2}$. Thus transverse components of the electric field amplitudes in the three regions become (refer to Figure 2.6)

$$E_y(x) = \begin{cases} Aexp(-\gamma_c x) & x > 0 \\ Bcos(\kappa_f x) + Csin(\kappa_f x) & -h < x < 0 \\ Dexp(\gamma_s(x+h)) & x < -h \end{cases} \tag{2.7}$$

Applying the boundary conditions and simplifying we get the eigenvalue equation for β. For the TE case under consideration it is:

$$tan(h\kappa_f) = \frac{\gamma_c + \gamma_s}{\kappa_f[1 - \frac{\gamma_c \gamma_s}{\kappa_f^2}]} \tag{2.8}$$

Following the same procedure for the TM case we get the following characteristic equation:

$$tan(h\kappa_f) = \frac{\kappa_f[\frac{n_f^2}{n_s^2 \gamma_s} + \frac{n_f^2}{n_c^2 \gamma_c}]}{\kappa_f^2 - \frac{n_f^4}{n_c^2 n_s^2} \gamma_c \gamma_s} \tag{2.9}$$

These transcendental equations can be solved numerically or graphically (refer to Figure 2.5) to any level of desired accuracy.

Every valid β value corresponds to a mode in the slab waveguide [23]. Only a finite number of discrete modes will be guided but there are is a continuum of β values for radiation modes. These modes are unique and orthogonal to each other. One

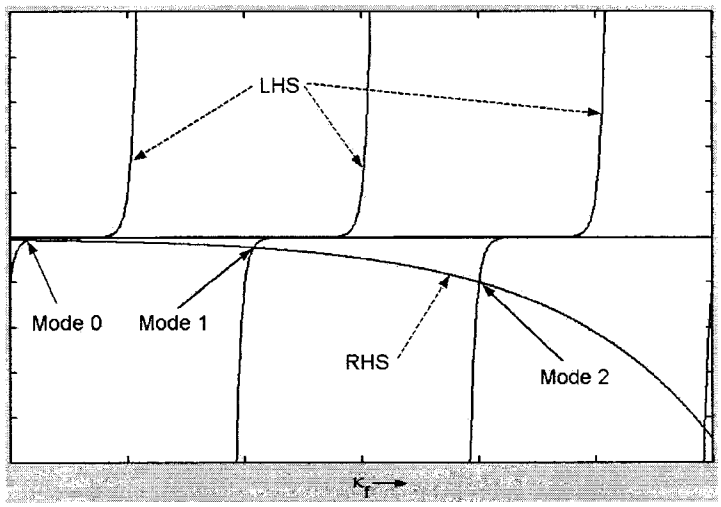

Figure 2.5: Graphical solution of eigenvalue equation 2.8

can draw an analogy to the Fourier series basis functions. Figure 2.6 shows the slab waveguide with different mode field distributions. Figure 2.7 shows the simulation result for an As_2Se_3 (refractive index 2.7) slab waveguide on a benzocyclobutene undercladding (refractive index 1.54). Figure 2.7(a) shows the allowed values of β for different slab thicknesses. Figure 2.7(b) plots the confinement factors for different modes. Figures 2.7(c) and 2.7(d) shows the allowed mode profiles in a 1 μm thick As_2Se_3 slab waveguide.

In practice, rigorous numerical solutions to Maxwell's equations in many planar

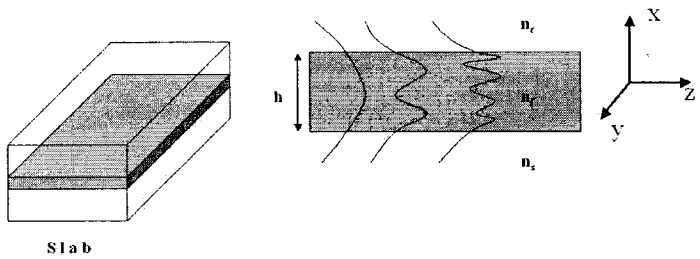

Figure 2.6: Modes in a slab waveguide

integrated waveguides (refer to Figure 2.1) tend to be computationally intensive. The effective index method (EIM) is an accurate and powerful alternative technique that is widely used to analyze such structures.

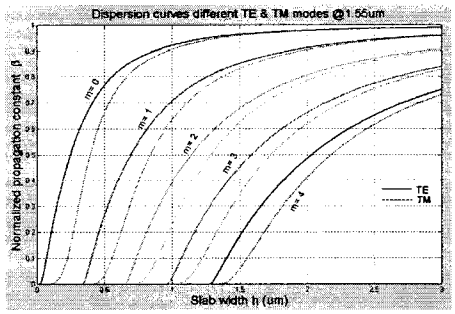

(a) Dispersion curves for different modes at 1550 nm

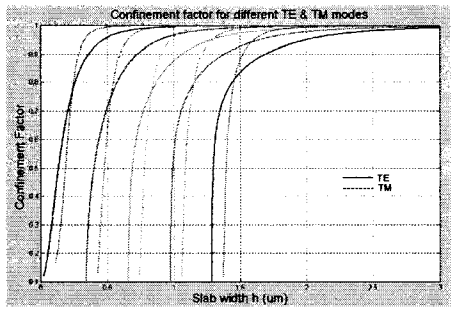

(b) Confinement factor for different modes at 1550 nm

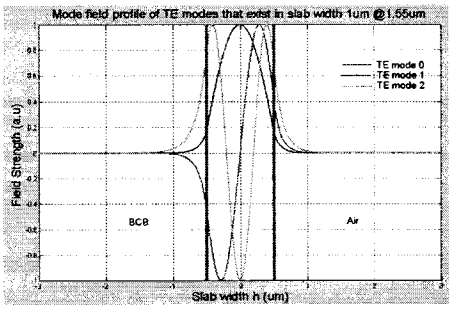

(c) TE modes in a 1 μm thick As_2Se_3 slab

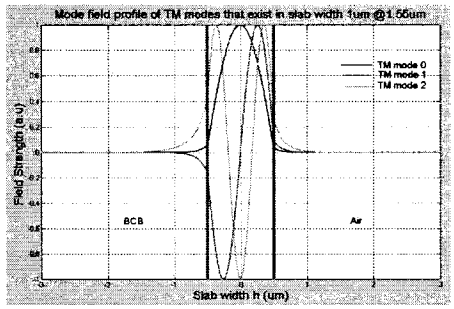

(d) TM modes in a 1 μm thick As_2Se_3 slab

Figure 2.7: As_2Se_3 slab waveguide mode simulations at 1500 nm

2.1.2 Effective Index Method

The effective-index method (EIM) is the most popular method for analyzing integrated optical devices. This method reduces the 2D wave equation for a rib geometry, where there are no analytical solutions, into two 1D problems [24, 25], by converting the rib waveguide problem to two equivalent one-dimensional slab waveguide problems. Figure 2.8 shows this concept [26].

To find the TE modes in the waveguide shown in Figure 2.8 we first analyze the structure from the top view, i.e. in the Z-Y plane. The three regions: I, II and III, are treated as slab waveguides of thickness l, h and l respectively. TE propagation constants are found using standard slab waveguide analysis described in Section 2.1.1. Effective indices for each of the region, N_f and N_l can be found from the propagation constants using equation 2.10

$$n_{eff} = \frac{\beta\lambda}{2\pi} \tag{2.10}$$

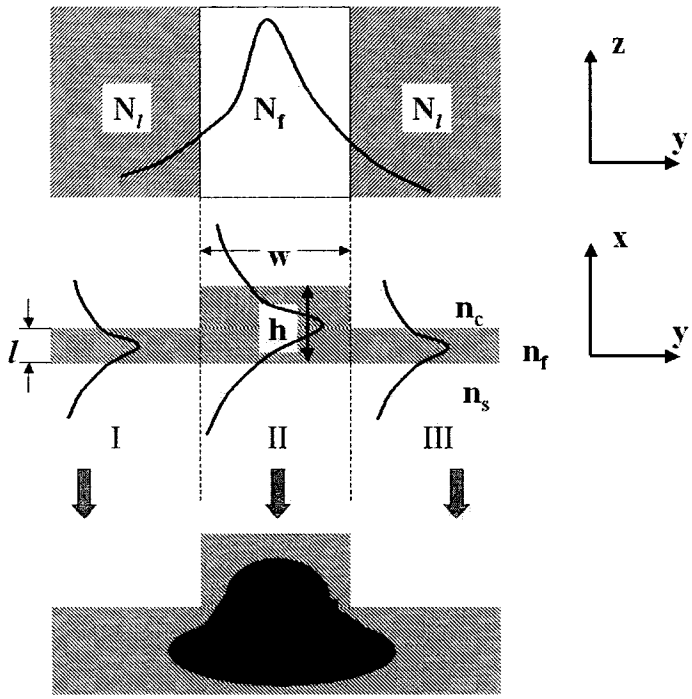

Figure 2.8: Schematic illustration of the EIM

Now, using the equivalent symmetric waveguide in the Z-Y plane having core index N_f and cladding indices N_l we find the TM modes that exist. Combining the field profiles in both views we get the actual mode field distribution. For example, if the field profile in region II is given by $F(X)$ and the field distribution in the N_f region is given by $F(Y)$ then the overall field distribution is described as:

$$\Psi(X,Y) \simeq F(X) * F(Y) \tag{2.11}$$

If upper and lower cladding are different materials, and the thickness of the outer slab is very small such that it cannot support a mode, the effective index method will fail. Hence modeling a strip waveguide by this method is not trivial and commercial numerical mode solvers were used for simulations. Figure 2.9 shows a polyamide-imide strip waveguide encapsulated in benzocyclobutene simulated in commercial OptiBPM modelling software.

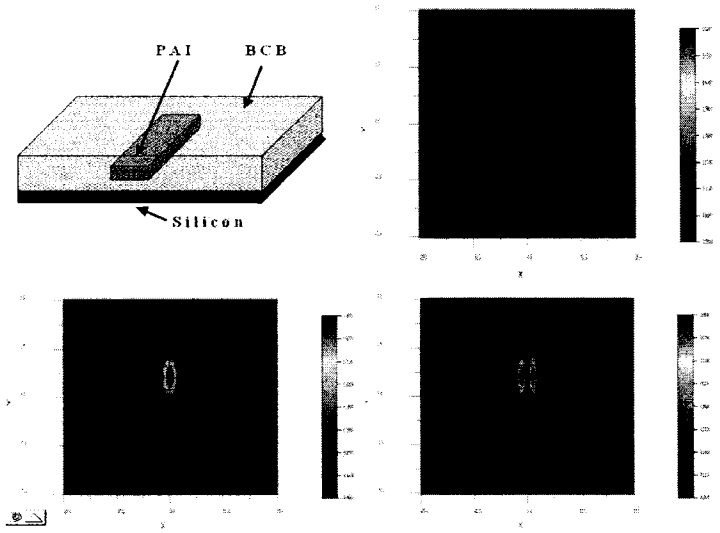

Figure 2.9: Modes simulation in a strip waveguide using OptiBPM modeling software.

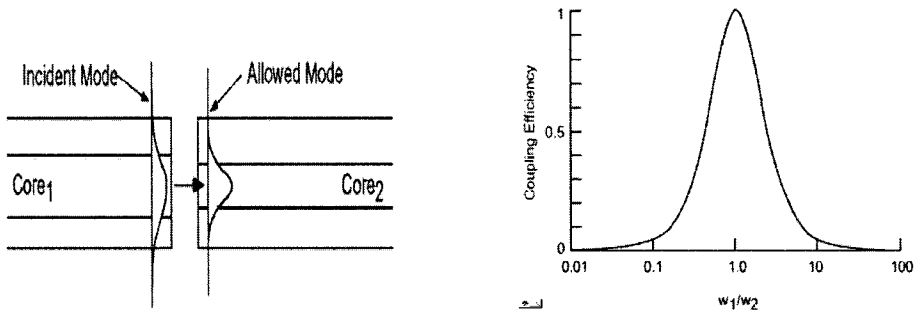

(a) Coupling between two dissimilar waveguides

(b) Coupling efficiency as a function of MFD ratios

Figure 2.10: Dependence of butt coupling efficiency on MFD mismatch

2.1.3 Coupling between waveguides

A signal traversing from one waveguide to another incurs a coupling loss in addition to practical misalignment losses. Figure 2.10 shows two dissimilar single-moded slab waveguides butt-coupled to each other. W_1 and W_2 are the mode field diameters (MFD) of the incident and transmitted mode respectively. Then the coupling efficiency, which is the ratio of the power in the transmitted mode to the incident mode, is shown in the Figure 2.10(a) and Figure 2.10(b).

One of the common methods to reduce the coupling loss is by tapering (vertically

or laterally) one of the waveguide to convert the incident MFD to match that of the second waveguide [27, 28].

Butt-coupling is used to couple light into an integrated optic waveguide while doing loss measurements. Normal single mode fibers have too large a MFD to couple efficiently into integrated optic waveguides. Specialized small tapered or smaller core waveguides were used in our experiments.

Proper cleaving and polishing the samples to get good waveguide end facets is very important to reduce coupling losses. Especially in high index contrast waveguide structures the use of index-matching compounds is necessary.

Another method of coupling power between waveguides is through the evanescent part of the guided mode. This is discussed in section 2.4.4.

2.2 Losses in integrated optic waveguides

Light undergoes attenuation as it travels along a waveguide. Losses can be classified on the basis of their origin into material absorption, scattering losses due to roughness etc., and bending losses. Both core materials used in this work (Polyamide-imide and chalcogenide glasses) exhibit very low material absorption at the wavelengths of interest. The scattering losses are the result of the fabrication process and can be reduced by careful optimization of lithography and etching parameters. Waveguide bend losses can be minimized by proper design. High-index contrast structures allow for lower bend radius while keeping the bend losses tolerable. The total attenuation determines the quality of a waveguide. Two of these losses, scattering losses due to sidewall roughness and bend losses, are analyzed in the following sections.

While sidewall roughness contributions are higher in high index material systems, the bend losses are lower. Waveguides are characterized by measuring the losses that light incurs while propagating through it. Some of the characterization techniques used used to measure waveguide loss are also described in the sections that follows.

2.2.1 Scattering losses due to side-wall roughness

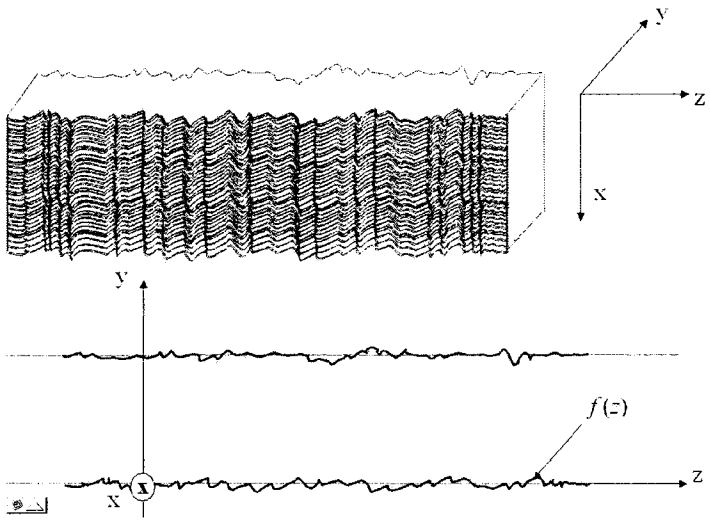

Figure 2.11: Line edge roughness model[4]

Each of the fabrication steps such as photolithography, lift-off, etching etc. can affect the sidewall roughness. It is important to quantify the waveguide roughness to know how to control the fabrication parameters [4]. Equation 2.12 shows the dependence of scattering losses due to line-edge roughness with index contrast. The propagation loss α_{st} due to sidewall roughness is given by [29]

$$\alpha_{st} = \frac{\sigma^2 k_0^2 h}{\beta} \cdot \frac{E_s^2}{\int E^2 dx} \cdot \Delta n^2 \tag{2.12}$$

where σ is the RMS sidewall roughness, k_0 is the free space wavenumber, β is modal propagation constant, Δn is the difference between the refractive indices of the core and cladding, while h is the transverse propagation constant in the core. Hence, Equation 2.12 indicates that the scatter loss is proportional to the normalized electric field intensity at the core-cladding interface and to the square of interface roughness.

It has been shown that knowing only the σ of sidewall roughness (refer to Equation 2.12) is not sufficient for accurate loss measurement. Along with σ, the correlation length (L_c) of the roughness distribution is needed to give a better estimate of the scattering loss [30].

2.2.1.1 Roughness Model

In planar waveguides, only the sidewall walls are considered rough while top and bottom walls are considered smooth. In most cases the roughness on the sidewalls is invariant in the x direction, as shown in Figure 2.11. This reduces the roughness modeling to one dimension.

$f(z)$ is the roughness distribution, that is the perturbation of the real edge with respect to an idealized straight edge. Without of loss of generality $f(z)$ can be taken to have a zero mean. The nature of the roughness can be described by the autocorrelation of $f(z)$.

$$R(u) = \langle f(z)f(z+u)\rangle = \int_{-\infty}^{\infty} f(z+u)\overline{f(z)}dz \tag{2.13}$$

Where $\overline{f(z)}$ is the complex conjugate of $f(z)$. Autocorrelation detects non-randomness in roughness data. This autocorrelation function follows an exponential model in most cases.

$$R(u) \approx \sigma^2 exp(\frac{-|u|}{L_c}) \tag{2.14}$$

Where σ^2 is the variance and L_c the correlation length. The scattering losses are proportional to σ^2 and follows L_c in the range of L_c usually observed.

The spectral density $S(\Lambda)$ of the roughness is obtained by taking the Fourier transform of the autocorrelation function over 2π.

$$S(\Lambda) = \frac{1}{2\pi}\int_{-\infty}^{\infty} \sigma^2 exp(\frac{-|u|}{L_c})exp(-2\pi i\Lambda u)du = \frac{1}{2\pi}\frac{\sigma^2}{\pi}\frac{2\pi}{L_c(1+\Lambda^2 L_c^2)} \tag{2.15}$$

$$S(\Lambda) = \frac{1}{\pi}\frac{\sigma^2}{L_c(1+\Lambda^2 L_c^2)} \tag{2.16}$$

where Λ is the spatial radial frequency.

It should be noted that only those spatial radial frequencies that lie in a specific range will affect scattering loss for any given wavelength [4]. Such an effect is seen in Section 5.3. One way to extract the roughness distribution is to take a high-resolution top view scanning electron micrograph of the waveguide. After filtering out some noise, the edge is detected to obtain the line-edge roughness distribution $f(z)$. Autocorrelation of $f(z)$ is done and fitted to the exponential model derived above. This gives us an estimate of the variance, σ^2 and the correlation length, L_c.

Reference [4] uses a more refined statistical method to estimate the spectral density of the roughness distribution. This is then fitted to the Lorentzian spectral density to obtain σ^2 and L_c.

The quality of the photolithography process and etching process defines the sidewall roughness in the final device. Some of the methods for reducing roughness includes oxidation smoothening in Si/SiO_2 waveguides [31]. In this case the Si waveguides were oxidized first followed by anisotropic etching which is shown to have reduced the sidewall roughness. Another technique especially suitable for polymer based waveguides is the reflow technique [32].

2.2.2 Bend Losses

Bends are very important in integrated optics for changing the optical path direction. Tighter bends means smaller bending radii, which cause the guided mode to leak out into the cladding (refer to Figure 2.12). For a given material system and waveguide dimensions there is a limit to which the bending radius can be reduced before bend losses become significant [33].

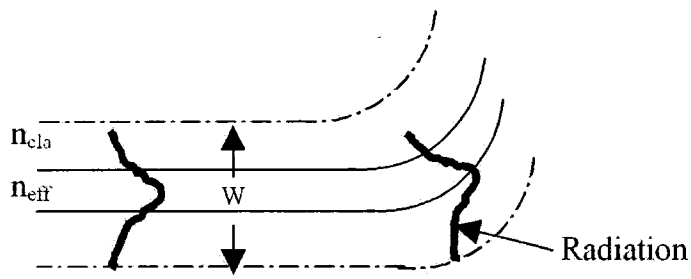

Figure 2.12: Bend losses in a waveguide

The mode profile of a guided mode in a straight waveguide and in a curved waveguide of same dimension is very different. We can visualize this by the method of conformal mapping to treat waveguide bends [34]. In this, a bent waveguide problem is transformed into straight waveguide problem. The rest of the analysis of the guided mode is done in the traditional way, for example, by effective index method.

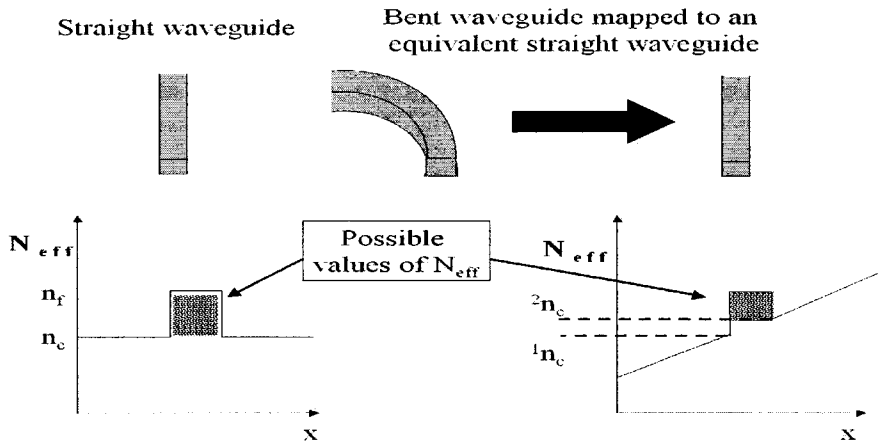

Figure 2.13: Conformal mapping of a curved waveguide to straight waveguide

Figure 2.13 shows the a curved waveguide that is transformed into a straight waveguide by conformal mapping technique [35]. The equivalent effective index distribution for the transformed waveguide depends on the radius of the curved waveguide. The possible effective index space for a guided mode reduces due to the the curvature (refer to Figure 2.13). From Figure 2.13 we also can get an idea about how the center of gravity of the guided mode will be leaning towards the 'higher effective index' region in the curved waveguide case and hence leak out. Outside the core, the mode decays with a large evanescent tail in the direction of the radius.

The bending losses decrease exponentially with increasing radius except for small radius [36]. The bending loss in a channel waveguide can be approximated by [37]

$$\alpha_{bend} \approx C_1 exp(-C_2 R) \tag{2.17}$$

where C_1 and C_2 are constants dependent on the waveguide dimensions.

2.3 Loss Measurement

In simple terms, the waveguide losses at a particular wavelength can be estimated by measuring the input and the output power for a known length of the waveguide.

$$\alpha = -\frac{10log(\frac{P_{out}}{P_{in}})}{L}(dB/cm) \tag{2.18}$$

where α is the attenuation coefficient, P_{in} and P_{out} are the optical powers at the input and the output of the waveguide and L is the length of the waveguide in centimeters. Figure 2.15 shows the setup used for the measurement of losses in an integrated optic waveguide.

2.3.1 Cut-Back Method

This is a straightforward method to measure the attenuation in an integrated optical waveguide. In this method the sample is cut into different lengths and the transmitted powers are measured to estimate the loss per unit length. It is assumed that the coupling efficiency in all cases would remain the same. The above equation is used to calculate the waveguide losses [38].

2.3.2 Fabry-Perot Interferometer Method

A waveguide can be visualized as a cavity with the two end facets acting as partially reflecting mirrors. The losses inside the cavity can be estimated from the peaks and valleys, Tmax and Tmin, of its transmission spectrum [39]. A typical transmission spectrum for a single-moded waveguide is shown in Figure 2.14.
There are two ways to measure the peaks and valleys: by using narrow linewidth tunable lasers or by heating the sample to change its length or refractive index.

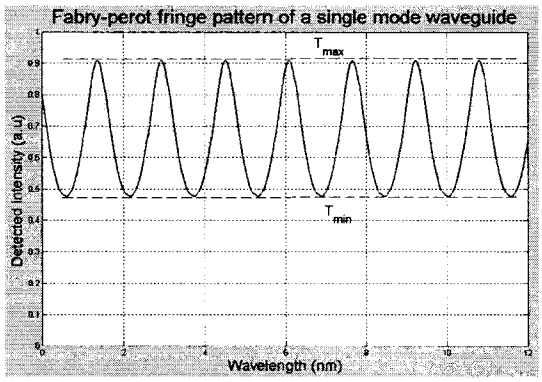

Figure 2.14: Picture of fringe pattern for single mode waveguide

If R, the geometric mean of the reflection coefficients of the two end facets, is

known then we can use the following expression to estimate the loss

$$\alpha = -\frac{10}{L} log(\frac{1}{R}\frac{\sqrt{T_{max}} - \sqrt{T_{min}}}{\sqrt{T_{max}} + \sqrt{T_{min}}})(dB/cm) \tag{2.19}$$

In practice the same equation written in the following way is used to plot the left hand side versus different lengths of samples. The slope of the straight line fit gives the propagation loss. This entirely avoids prior knowledge of R.

$$10log(\frac{\sqrt{T_{max}} - \sqrt{T_{min}}}{\sqrt{T_{max}} + \sqrt{T_{min}}}) = 10log(R) - \alpha L \tag{2.20}$$

This method leads to accurate results for very low loss waveguides (<0.2 dB/cm). Since the reflectivity of the end faces needs to be high, this method is very appropriate for waveguides in high index materials. For lower index materials the end faces of the waveguides can be coated with high-reflection films. It should be noted that this method works only for single mode waveguides. The Fabry-Perot interference pattern of a multimoded waveguide is not uniform and shows a large apparent loss.

2.3.3 Scatter Loss measurement

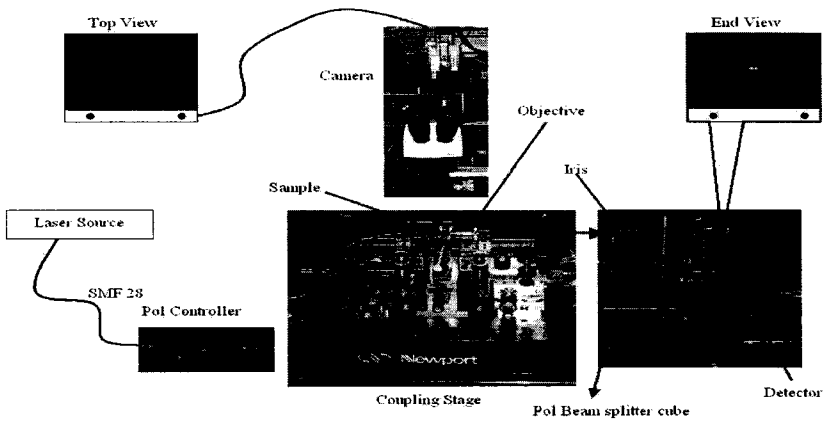

Figure 2.15: Experimental setup for loss measurement

In an optical waveguide the guided mode loses part of its power while traveling along the waveguide due to Rayleigh scattering. This scattered light is proportional

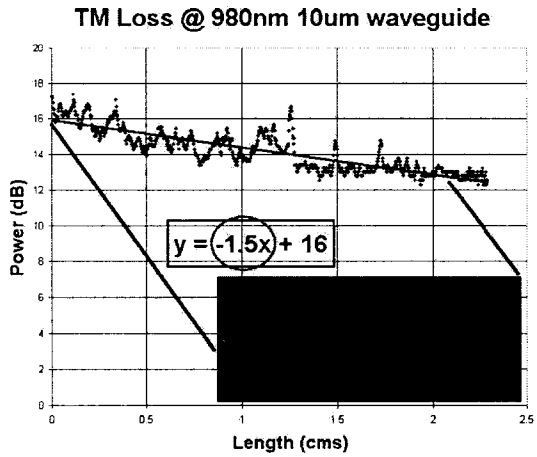

Figure 2.16: Streak for loss measurement

to total guided power. Hence a plot of scattered light with distance will be an exponential function [40].

There are two methods that we have employed to collect the scattered data. One

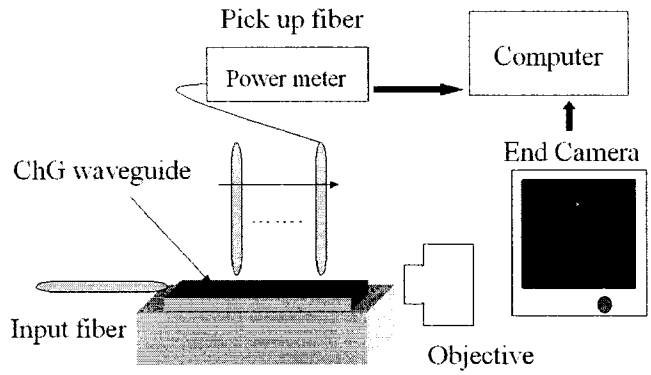

Experimental Setup

Figure 2.17: Experimental setup using a pickup fiber for loss measurement

uses a video camera to capture the scattered light from the top of the waveguide. The pixel value of the light streak is mapped to intensity of the scattered light. In this case we assume that the video camera is linear for the wavelength range we are interested in. Another image of a known distance is taken at the same magnification

to map the pixel spacing and the real length needed to calculate the loss per cm (refer to Figure 2.16). In the other method, a pickup fiber is used to collect the scattered light and the power is measured using a photodetector (refer to Figure 2.17). A micrometer translates the pickup fiber along the light streak, maximizing the power collected at each point. The loss is estimated from the slope of a log plot of intensity measured with distance measured in centimeters.

2.4 Ring Resonator

A ring resonator is a waveguide wrapped around to form a ring. The resonator need not be annular, other geometries like the racetrack resonator also falls into this category. Racetrack resonator includes two straight sections in the ring to aid in coupling light in and out of the cavity. As in any other cavity, the geometry of the ring defines its transmission at a given frequency.

Unlike the Fabry-Perot resonators, ring resonators are a traveling wave cavities.

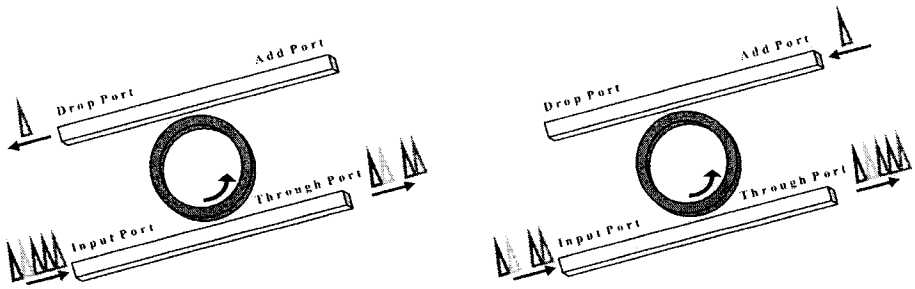

(a) Ring Resonator in Drop configuration (b) Ring Resonator in Add configuration

Figure 2.18: Ring resonator as an add-drop multiplexer

Hence, if only unidirectional propagation is allowed there will be no standing waves created. This is very important for lasing purposes, since in the traveling wave cavity there is no spatial hole burning effects ([41]). A ring resonator in an add-drop configuration consists of a ring and two waveguides that couples light in and out of the ring (resonator). It is a four-port device as shown in the Figure 2.18.

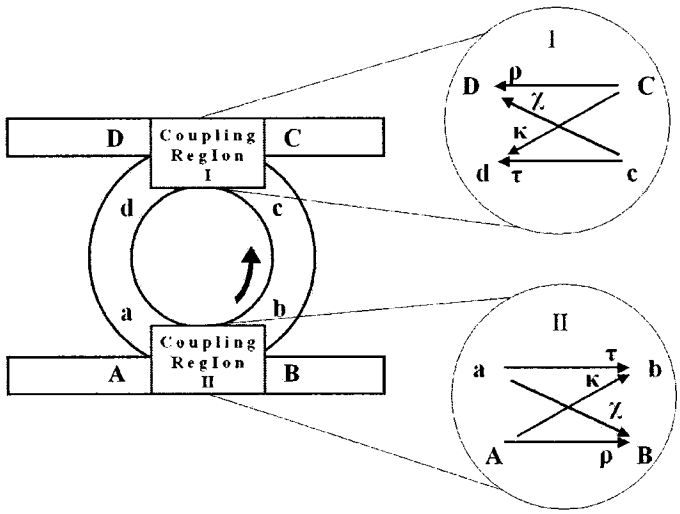

Figure 2.19: Ring Resonator model

2.4.1 Modeling Ring Resonator Add-drop multiplexer

In this section some of the important expressions for a single ring resonator in add-drop multiplexer configuration are derived [8, 42, 43]. It is assumed that the waveguides and the ring are single moded. The back reflections and any nonlinearity are completely ignored. The coupling regions are assumed to be symmetric and lossless. In Figure 2.19, $A_{\pm},B_{\pm},C_{\pm},D_{\pm}$ and $a_{\pm},b_{\pm},c_{\pm},d_{\pm}$ denote the amplitude of the guided modes traveling in the positive/negative z direction in the bus waveguides and the cavity respectively. ρ, τ are the self-coupling coefficients and κ, χ, the cross coupling coefficients. The coupling coefficients are complex numbers. L is the circumference of the ring. If the ring radius is r, $L = 2\pi r$.

$$\begin{array}{ll} A_- = \rho B_- + \chi b_- & B_+ = \rho A_+ + \chi a_+ \\ a_- = \kappa B_- + \tau b_- & b_+ = \kappa A_+ + \tau a_+ \\ C_+ = \rho D_+ + \chi d_+ & D_- = \rho C_- + \chi c_- \\ c_+ = \kappa D_+ + \tau d_+ & d_- = \kappa C_- + \tau c_- \end{array} \tag{2.21}$$

The ring is excited only from one of the ports at a time. In the drop configuration, the ring is excited through the input port A. Whereas, in the add configuration, ring excitation is from the add port C. For the derivation below, we will consider the device in the drop configuration. These expressions can be extended for the add configuration easily by viewing C as the input port instead of A.

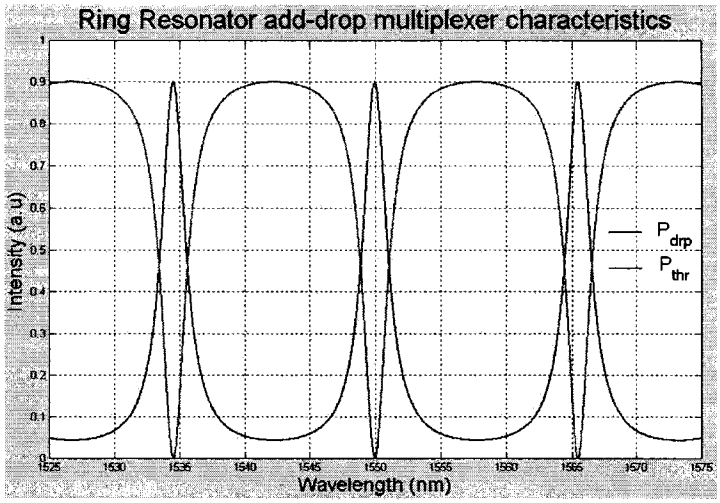

Figure 2.20: Plot of add and through port powers with β

Let the complex propagation constant in the ring be given by:

$$\gamma = \beta - \alpha i \tag{2.22}$$

where $\beta = \frac{2\pi n_{eff}}{\lambda}$ is the wave propagation constant and α the intensity attenuation coefficient in the ring. Then,

$$\begin{aligned} a_+ &= d_- exp(\tfrac{-i\beta L}{2}) exp(\tfrac{-\alpha L}{2}) \\ b_- &= c_+ exp(\tfrac{-i\beta L}{2}) exp(\tfrac{-\alpha L}{2}) \\ c_- &= b_+ exp(\tfrac{-i\beta L}{2}) exp(\tfrac{-\alpha L}{2}) \\ d_+ &= a_- exp(\tfrac{-i\beta L}{2}) exp(\tfrac{-\alpha L}{2}) \end{aligned} \tag{2.23}$$

In the drop configuration the ring is excited only from port A and all back reflections are assumed to be zero. Using Equations 2.21 and 2.23, the power in the drop and through ports is given by:

$$P_{drp} = |D_-|^2 = \frac{|\chi|^2 |\kappa|^2 exp(-\alpha L)}{1 + |\tau|^4 exp(-2\alpha L) - 2|\tau|^2 exp(-\alpha L) cos(\beta L - 2\phi)} P_{inp} \tag{2.24}$$

$$P_{thr} = |B_+|^2 = |\rho|^2 \frac{1 + |\tau|^2 d^2 exp(-2\alpha L) - 2|\tau| d exp(-\alpha L) cos(\beta L \phi - \psi)}{1 + |\tau|^4 exp(-2\alpha L) - 2|\tau|^2 exp(-\alpha L) cos(\beta L - 2\phi)} P_{inp} \tag{2.25}$$

Where, d, ϕ, ψ are real quantities defined by:

$$\begin{aligned} \tau &= |\tau| exp(i\phi) \\ \tau - \tfrac{\chi\kappa}{\rho} &= d exp(i\psi) \end{aligned} \tag{2.26}$$

If we assume that the coupler is symmetric and lossless the two cross coupling coefficients are equal and so are the two self-coupling coefficients. Hence the following relations hold:

$$\rho \approx \tau$$

$$\kappa \approx \chi$$

$$|\rho|^2 + |\kappa|^2 \approx 1 \tag{2.27}$$

$$|\tau|^2 + |\chi|^2 \approx 1$$

$$|\kappa|^2 \approx |\chi|^2 \approx 1 - |\tau|^2$$

2.4.2 The resonance condition

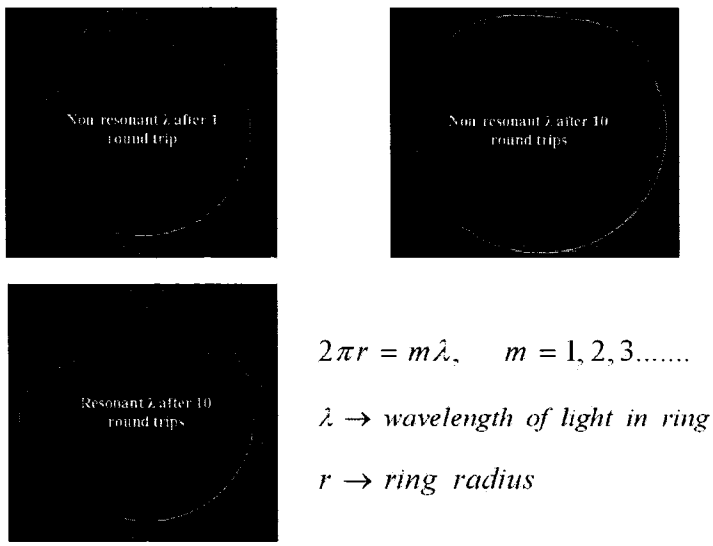

Figure 2.21: Illustration of Resonance in a Ring Resonator

From Figure 2.20 that power dropped is maximized (power transmitted is minimum) the following relation holds:

$$cos(\beta L - 2\phi) = 1$$

$$or \tag{2.28}$$

$$\beta_m \approx \frac{2m\pi + 2\phi}{L}$$

where m is an integer and β_m corresponds to the m^{th} resonance. The peaks in Figure 2.20 represent the ring resonances. Figure 2.21 illustrates the resonance condition

in a ring. The power in the drop port is maximized at resonance, i.e.

$$P_{drp}(\beta = \beta_m) = \frac{|\chi|^2|\kappa|^2 exp(-\alpha L)}{(1-|\tau|^2 exp(-\alpha L))^2} P_{inp} \tag{2.29}$$

2.4.3 Figures of merit for Ring Resonator Add-Drop Multiplexer

The important parameters that represent the quality of a ring resonator are given below. As in any resonator, the quality of response of the ring resonator is represented by it's on-off ratio, full width half maximum, free spectral range, finesse and quality factor.

2.4.3.1 On-off ratio

On-off ratio is the ratio between dropped power at resonance and at anti-resonance. Consider the power dropped at resonance wavelength and half resonance wavelengths. At anti-resonance

$$cos(\beta L - 2\phi) = -1 \tag{2.30}$$

Now from equation 2.24

$$On-off = \frac{P_{drp}(resonance)}{P_{drp}(anti-resonance)} = \frac{(1+|\tau|^2 exp(-\alpha L))^2}{(1-|\tau|^2 exp(-\alpha L))^2} \tag{2.31}$$

2.4.3.2 Full width half maximum

Full width half maximum (FWHM) or 3dB bandwidth is the measure of the wavelength region in which power dropped reduces to half the resonance value.

$$FWHM = 2|\lambda_{3dB} - \lambda_m| = 2|\delta\lambda| \tag{2.32}$$

This can be equivalently expressed in terms of β as:

$$|\delta\lambda| = \frac{\lambda^2 \delta\beta}{2\pi n_{grp}} \tag{2.33}$$

Where $\delta\beta$ and n_{grp}, the group refractive index, is given by:

$$\delta\beta_m = \beta_{3dB} - \beta m \tag{2.34}$$

$$n_{grp} = n_{eff} - \lambda \frac{\delta n_{eff}}{\delta\lambda} \tag{2.35}$$

Without loss of generality, we can assume that the resonance to be corresponding to $m = 0$ case. Then $\beta_0 = \frac{2\phi}{L}$. β_{3dB} can be found from its definition:

$$P_{drp}(\beta_{3dB}) = \frac{P_{drp}(\beta = \beta_m)}{2} \tag{2.36}$$

Making the assumption that β_{3dB} is very close to the resonance value β_0, $\delta\beta$ is found to be:

$$\delta\beta = \beta_{3dB} - \beta_0 = \frac{1}{L}(\frac{1}{|\tau|}exp(\frac{\alpha L}{2}) - |\tau|exp(\frac{-\alpha L}{2})) \tag{2.37}$$

Hence using Equations 2.37 and 2.33 in Equation 2.32, FWHM is given by:

$$FWHM = \frac{\lambda^2}{\pi n_{grp} L}(\frac{1}{|\tau|}exp(\frac{\alpha L}{2}) - |\tau|exp(\frac{-\alpha L}{2})) \tag{2.38}$$

2.4.3.3 Free spectral range

Free spectral range (FSR) is the wavelength spacing between two resonance peaks and is given by:

$$FSR = |\Delta\lambda| = \lambda_{m+1} - \lambda_m \approx \frac{\lambda^2}{n_{grp} L} \tag{2.39}$$

Where n_{grp} is defined in equation 2.35. It can be seen from Equation 2.39 that reducing the radius of the ring resonator translates to an increase in the FSR. Hence high-index contrast integrated optics not only reduces the overall footprint of the ring resonator devices but also increases the FSR.

2.4.3.4 Finesse

Finesse is the ratio between FSR and FWHM. It is a measure of the transmission characteristic of a filter. Using 2.38 and 2.39, Finesse can be expressed as

$$Finesse = \frac{FSR}{FWHM} = \pi \frac{|\tau|exp(-\frac{\alpha L}{2})}{1 - |\tau|^2 exp(-\alpha L)} \tag{2.40}$$

2.4.3.5 Quality factor

Q factor is the ratio of the stored energy to the power lost per power cycle. It is given by the ratio of the operational wavelength to the FWHM. Using 2.38 we have

$$Q = \frac{\lambda}{FWHM} = \frac{\pi n_{grp} L}{\lambda}\{\frac{|\tau|exp(-\frac{\alpha L}{2})}{1 - |\tau|^2 exp(-\alpha L)}\} \tag{2.41}$$

2.4.3.6 Critical coupling

Apart from the parameters described above, for a ring resonator based add-drop multiplexer to perform efficiently, further optimizations needs to be done. We can see that to maximize the on-off ratio given by equation 2.31, we need:

$$\begin{aligned} 1 - |\tau|^2 exp(-\alpha L) &\rightarrow 0 \\ \Rightarrow \qquad |\tau|^2 &= exp(\alpha L) \end{aligned} \tag{2.42}$$

i.e. the losses in the ring should be equal to the coupling losses. This is called the critical coupling condition [44]. This merely means that for a given material system and fabrication process, we can always maximize the on-off ratio (to the extent possible) by tweaking the coupling constant [45]. This kind of tuning or trimming the wavelength of ring is done is several ways for example, using platinum electrodes to thermal tuning [8] or by a UV sensitive polymer overlay [46]. A ring resonator straight from the microfab might exhibit little or no resonance. An on-off ratio of 20 dB or more is required for practical devices while the restriction on FWHM depends on the application.

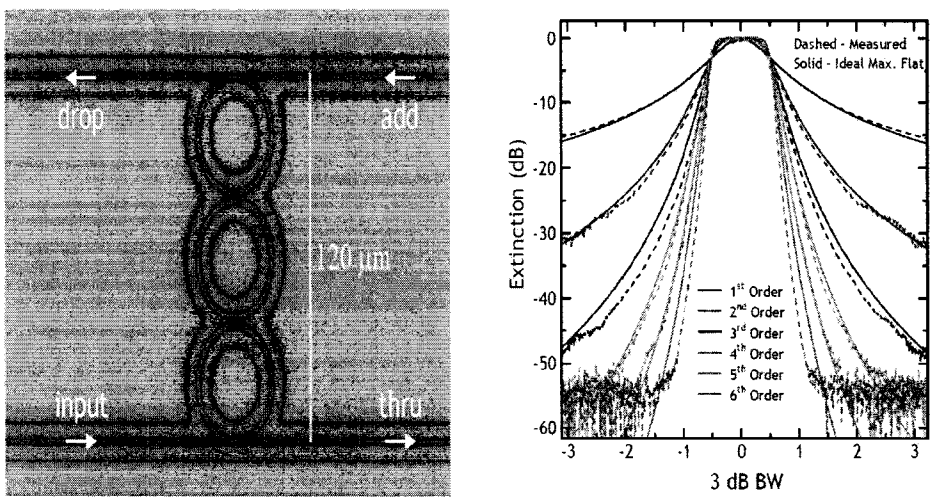

(a) Cascaded 3^{rd} order microrings

(b) Response of cascaded ring resonator

Figure 2.22: Commercial cascaded ring structure with box-like filter response [3]

The physical parameters can be tweaked to achieve desired filter response. The Lorentzian transmission characteristic of a single ring resonator can be made more flat or 'box-like' (refer to Figure 2.22(b)) by cascading multiple rings [3].

2.4.4 Coupler region

Coupling between bus and ring waveguides can be accomplished by the use a of directional coupler or a multi-mode interference (MMI) coupler.

2.4.4.1 Directional coupler

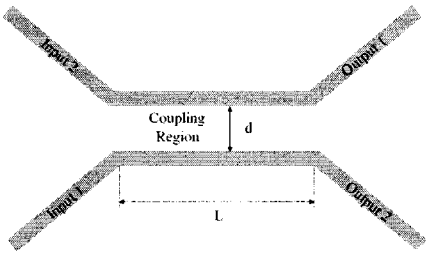

Figure 2.23: Picture of directional coupler

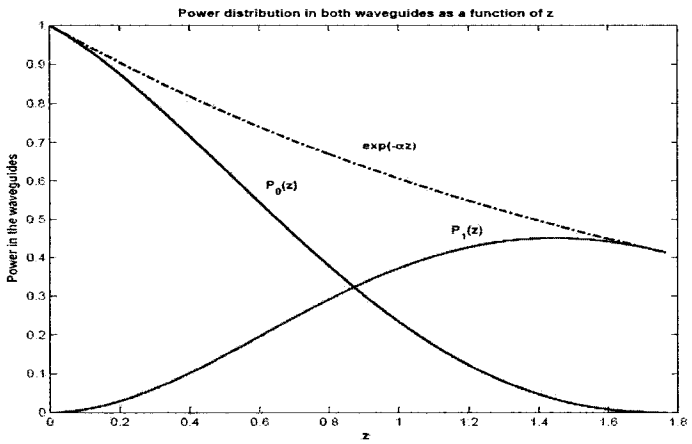

Figure 2.24: Power transfer in a directional coupler

In a directional coupler, two waveguides are placed adjacent to each other so that the evanescent fields of both can interact with each other (refer to Figure 2.23). This interaction causes the optical power to transfer back and forth as a function of the interaction length [47]. This power transfer between the two waveguides is plotted in Figure 2.24.

Consider identical waveguides separated by a distance of d, called the coupling gap. From coupled mode theory [33], the power in each waveguides after an interaction

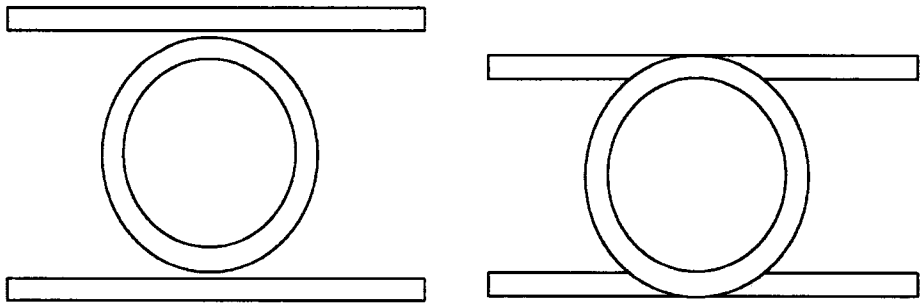

(a) Laterally coupled ring resonator (b) Vertically coupled ring resonator

Figure 2.25: Two ways of using directional coupler in micro-ring devices

length z is given by:

$$P_0(z) = cos^2(\kappa z)exp(-\alpha z)$$
$$P_1(z) = sin^2(\kappa z)exp(-\alpha z) \tag{2.43}$$

Where α is the attenuation coefficient and κ is called the coupling coefficient. κ decreases exponentially with the coupling gap, d and is given by:

$$\kappa = C_1 exp(-qd) \tag{2.44}$$

Where q is the y component of the extinction coefficient in the coupling region. Since the whole aim is to reduce the footprint of the device, the interaction length needs to be kept smallest possible. Smaller coupling gap means there is coupling between the evanescent fields of the two waveguides and this in turn translates to shorter coupler length for same splitting ratio. However in reality reducing the coupling gap is essentially the limiting factor for choosing the lithography system. Coupling gaps are a fraction of the waveguide width and tolerances are very tight to get efficient coupler regions. As will be seen, in Chapter 3, this has been the biggest factor for Ag doped rings that were fabricated.

From Section 2.2.2, we know that the mode profiles in the bent and straight waveguides are very different. Hence actual analysis of coupling between curved and straight waveguide sections is complicated.

Using a directional coupler to couple light in and out of a ring resonator allows us two different geometries as shown in Figure 2.25.

In laterally coupled structure, the waveguides and the ring are placed side by side

in the same plane (refer to Figure 2.25(a)). Laterally coupled structure requires that the gap between the ring and the bus waveguide be very small in order to obtain good coupling. This is especially true for high index contrast systems. Thus we would need to turn to high-resolution electron beam lithography and other techniques [48].

In vertically coupled structure (refer to Figure 2.25(b)) the ring sits on top or below the waveguides. In vertically coupled configuration evanescent coupling is achieved vertically. High coupling efficiency can be achieved by using an appropriate buffer layer between the ring and the waveguide. Vertical coupling of the ring to the bus also reduces the sensitivity to misalignments between the two. However fabrication of this structure requires precise alignment of the ring and the bus waveguides, typically involving specialized wafer-bonding techniques [49].

2.4.4.2 Multi-mode interference (MMI) coupler

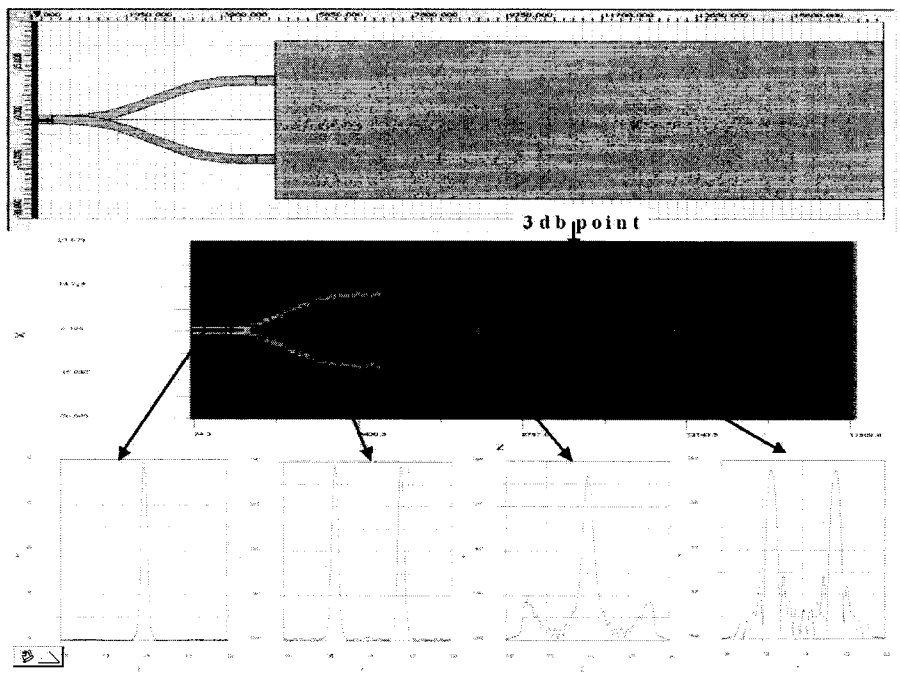

Figure 2.26: Multimode principle of operation

An MMI coupler consists of a broad center waveguide that supports several modes (refer to Figure 2.27). The two input waveguides modes interfere with each

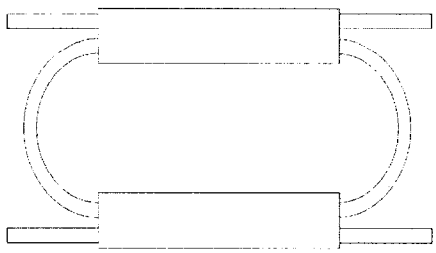

Figure 2.27: Ring resonator with MMI coupler

other in the wider section to produce self-images at particular intervals (refer to Figure 2.26). The MMI coupler is particularly suited to achieve 3 dB-splitting ratio [50].

While designing the MMI coupler, the mode field interference pattern in the wider section is analyzed to find the 3dB point, i.e. the distance from the input where the input power splits into two images with half the power. The fabricated device operation will be based on the length of the MMI region and the similarity of the input modes to the simulations. MMI couplers give a polarization independent performance as compared to directional coupler. The 3dB point in a MMI coupler is also shorter than in a directional coupler case [50].

Chapter 3

Silver doped waveguides in Chalcogenide glasses

This chapter describes silver photodoping experiments in As_2Se_3, $Ge_{33}As_{12}Se_{55}$ (IG2) and $Ge_{28}Sb_{12}Se_{60}$ (IG5) chalcogenide glasses. First, a brief overview of the usefulness of these glasses for integrated optics is given in the following section.

3.1 Chalcogenide glasses for Integrated Optics

The majority of glasses fall into one of the oxide (oxygen is a light atomic weight chalcogen element), halide and heavier chalcogenide families. Glasses containing one or more of the heavier chalcogen elements S, Se or Te populate the chalcogenide glass family. Typical binary glasses are formed from AsS, AsSe, GeS, and GeSe alloys. Ternary and quaternary glasses are often realized by combining these binary compositions or by addition of other elements such as Ga or Sb. Rare-earth elements and other dopants can be incorporated during the bulk glass formation process or during thin film deposition.

Chalcogenide glasses have been a subject of research since the 1950's [51]. The optical usefulness of chalcogenide glasses stems from their transparency in the infrared, a high linear and non-linear refractive index, ability to incorporate large concentration of rare-earth elements and the wide variety of photo-induced and acousto-optic effects they exhibit [52, 53]. These properties and processing compatibility with back-end CMOS processing give chaclcogenide glasses significant promise for integrated optics. This promise is described in more detail in Section

3.1.1 below.

3.1.1 Promise of Chalcogenide Glasses in Integrated Optics

Some of the interesting properties of chalcogenide glasses that made them a subject of research and technological development over the past several decades are as follows:

- Chalcogenide glasses have narrow bandgaps (2 eV) and relatively poor transparency (compared to oxide glasses) in the visible and UV wavelength regions. However, unlike the oxide and halide glasses, which absorb strongly in the IR region, chalcogenide glasses are highly transparent in the mid to far IR ($\sim$ 1 - 15 μm wavelength range). This has made them attractive for commercial IR windows, lenses for night vision devices, IR sensing [54] and fibers [55].

- Chalcogenide glasses have high refractive indices which along with their processing options allows fabrication of integrated optical devices [56] with small bend radii and small footprint as discussed in Section 1.3. This property has also made them attractive for photonic crystal research [57, 58, 59].

- The presence of heavier chalcogen atoms and weak bond strengths results in lower phonon energies ($\sim$ 350 - 450 cm^{-1}), even relative to flouride glasses ($\sim$ 550 cm^{-1}). This enables many mid-IR transitions (by rare earth ions) that are otherwise quenched by non-radiative relaxation in oxide glasses. Together with their ability to uniformly dissolve large concentrations of rare earths ions like Er^{+3}, Nd^{+3}, and Pr^{+3} etc. in their glass matrix, chalcogenide glasses make an attractive option for the use in active devices like amplifiers [60] and lasers [52, 61] in the infrared. Waveguide lasers formed by laser patterning of a bulk sample of Nd-doped GaLaS have already been demonstrated [62].

- Chalcogenide glasses typically have high Kerr nonlinearity ($\sim$ 100 times that of silica) and low two-photon absorption coefficient in the near IR wavelength region, but with similar response times as silica [53]. This makes

chalcogenide glasses interesting for all-optical switching devices [63]. Together with the ability to make small cross-section waveguides (due to the high refractive index), this might enable all-optical processing of signals with less than 1 W peak power in planar waveguide structures [63, 64].

- As a consequence of the the weak bonding arrangements, chalcogenide glasses exhibit an array of photoinduced structural changes [52]. Near bandgap light (typically wavelengths of 514 nm or 532 nm at a fluence of 100 J/cm^2) can be used to induce relatively large changes in glass absorption (photodarkening or photobleaching), refractive index and etch rates in some chemicals. These characteristics make chalcogenide glasses useful as inorganic photoresists [57] and in the patterning of integrated optical devices like gratings and waveguides. As an example, photodarkening of As_2Se_3 produces typically an index change of $\sim$0.05.

- Chalcogenide glasses dissolve metals (Ag, Cu, Zn etc) producing a red-shift in the band edge along with an increase in refractive index, etch resistance etc. The work described in this chapter was a study on exploiting this effect for making high-index contrast waveguides [65]. It has also been applied to the fabrication of infrared diffraction gratings [66, 67], microlenses [68] etc. Further discussion can be found in Section 3.1.3.

- Chalcogenide glasses also exhibit reversible phase change (from amorphous to crystalline state and vice versa) brought about by pulses of electric current or laser absorption [52]. The rewritable CD/DVD is based on this property [69, 70] as is Ovonic unified memory (OUM), which is touted as a replacement for current flash memory and has been successfully commercialized [71].

- Chalcogenide glasses are intrinsically p-type semiconductors and have been investigated along with other amorphous semiconductors for potential use in photovoltaic cells. Elemental selenium, sulfides, selenides and tellurides of cadmium have found use as photoreceptors and in electro-photographic

processes [72].

- Some chalcogenide glasses have high acoustooptic figures of merit and have been used for making bulk acoustooptic cells operating in the near IR [73]. The As_2S_3 chalcogenide glass was first investigated for use as potential acoustooptic beam deflectors [73].

- Chalcogenide glasses such as As_2S_3 have also been investigated as cladding materials in thin-film electrooptic waveguide devices [74].

- Chalcogenide glasses have also been investigated in magneto-optic devices due to their moderate Verdet constants, which is a result of the strong dispersion they exhibit in the infra-red [75].

- Thin films of most Chalcogenide glasses can be made at room temperature by thermal evaporation. In the case of ternary, quaternary glasses and other speciality glasses, where the melting points of the constituents differ considerably, pulsed laser deposition [76] and chemical vapor deposition [77] have been employed for making thin films. Furthermore, refractive index and other properties can be tuned as chalcogenides have a large glass forming region.

- Chalcogenide glasses are not hygroscopic like fluoride-based glasses but are mechanically weaker than oxide glasses [78]. There are several impediments which need to be overcome if chalcogenide glasses are to be successful in integrated optics. Processing issues [60], and thermal and chemical stability [56, 79] require further study. There are also questions surrounding operational and environmental stability [64].

Commercially, chalcogenide glasses for integrated optics were investigated by Texas Instruments in the 1970s [80]. With the rapid growth of fiber networks in the 1990s there has been a renewed interest in materials for integrated optics. Research groups at Lucent recently investigated chalcogenide glasses for all-optical switching devices [63, 63]. To date most patterning has been done using direct laser-writing [79, 63, 81], where waveguides are produced using the photosensitivity of most chalcogenides to light near their band edge. Planar waveguides with

very low losses (< 0.3 dB/cm) have also been reported [82]. Other methods for writing waveguides have been explored including helium implantation and patterning in standard photolithography mask aligners [52]. Table 3.1 summarizes some of the best waveguiding results reported in the literature.

Table 3.1: Low-loss chalcogenide glass waveguides reported in the literature

ChG Alloy	Waveguide Type	Core size (μm)	λ (nm)	Loss (dB/cm)	Ref
As_2S_3	Slab	0.7	1064	2	[80]
$Ge_{10}As_{40}Se_{10}S_{40}$	Slab	1	1060	0.4	[83]
As_2S_3/ $As_{24}Se_{38}S_{38}$	Shallow Rib	1.25 x 5	1300	1	[56]
$Ge_{10}As_{40}Se_{25}S_{25}$	Laser written	1 x 5	1566	0.3	[79]
Ge_2Se_3	Laser written	1.7 x 3	1550	1.6	[63]
As_2S_3	Laser written	2.5 x 3.5	1550	0.2	[81]
As_2Se_3	Shallow Rib	1 x 4	1530	0.26	[82]

3.1.2 Arsenic Triselenide glass system

Most integrated optics work reported in the literature has been in sulfide glasses. Arsenic triselenide (As_2Se_3) chalcogenide glass, chosen for much of this work is a brown colored material with a refractive index $\sim$ 2.7 at 1550 nm and is soluble in bases and hot water. It is commercially available in bulk form and conventional thermal evaporation can be used to produce high-quality thin films chemically identical to the bulk sample. The transparency window of selenide glasses is approximately in the 0.8 - 15 μm wavelength range, while that of sulfide glasses is approximately in the 0.5 - 10 μm wavelength range. However sulfide glasses typically have a wider bandgap, higher glass transition temperature, lower density, greater hardness, and higher thermal conductivity [84]. Selenium based chalcogenide glasses like

As_2Se_3 typically have a high nonlinear figure of merit and a nonlinear Kerr coefficient approximately three orders of magnitude higher than silica glass at 1550 nm wavelength [85].

Arsenic and Selenium are highly toxic elements necessitating proper safety considerations. The thermal evaporator needs to be properly ventilated and masks with appropriate particulate filters should be used. Gloves need to be worn to protect the sample as well as oneself while handling. Annealing, chemical treatment (etching) etc. should be carried out in a fumehood. The glass is also attacked by acids, alkalies and amines. As_2Se_3 is also soluble in hot water and prolonged exposure to any chemical should be avoided.

We have found that As_2Se_3 glass exhibits excellent thermal, mechanical and chemical compatibility with commercial polymers like polyamide-imide or PAI (Torlon, Solvay Advanced Polymers) [86] and benzocyclobutene (BCB) (Cyclotene, Dow Polymers). This allows great versatility in fabrication processes based on chalcogenide glass core layers and polymers claddings.

3.1.3 Photo-Doping of Chalcogenide glasses

Metal doping of chalcogenide glasses has been the subject of much research and technological development over the past several decades [87, 53].

There are variety of ways to dope a film uniformly with silver. For example, thin films can be made by direct evaporation of bulk alloys of Ag doped glass synthesized from elements or compounds in evacuated ampoules [88]. However, for selectively doping silver this method is not appropriate. In a typical photodoping process, a metal film (such as silver, copper, zinc etc.) is deposited on a chalcogenide glass and light near the bandgap wavelength of the chalcogenide glass causes dissolution of the metal by the chalcogenide glass.

Silver is the most common metal used for photodoping studies [53, 89] and is the subject of this work. Silver dissolution in the glass can also be induced by irradiation with an ion beam [90] or electron beam [91] or by heating [92]. Thermal doping of silver is particulary important as it proceeds at all temperatures to some degree. In most silver doping experiments the doping is a result of both thermally

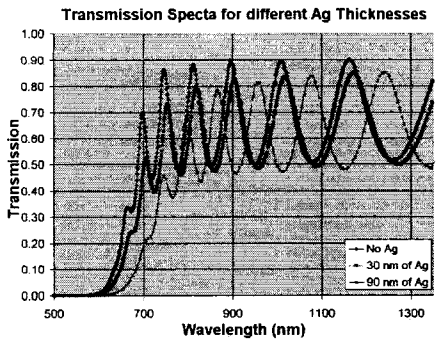

(a) Transmission curve for As_2Se_3 undoped and doped films

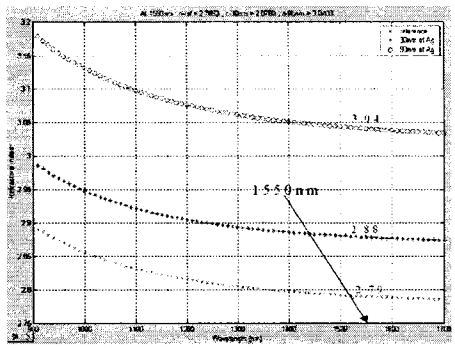

(b) Refractive index dispersion curve for undoped and doped As_2Se_3 films

Figure 3.1: Transmission spectra and refractive indices for different Ag concentrations

activated and light-activated processes [93, 94]. The dissolution can proceed even in dark although the rates are much lower without illumination. We have observed this dissolution in our our work using As_2Se_3. The rate of Ag dissolution depends greatly on composition of chalcogenide and an excess of chalcogen atoms (over the stoichiometric number) is known to affect the reaction [53].

Depending on the amount of silver that is doped into the glass, optical transmittance of doped parts is reduced by some amount (Figure 3.1(a)) and the optical absorption edge (band edge) underdoes a red shift [87]. Associated with this red shift is an increase in refractive index, which can be as high as 0.3 (Figure 3.1(b)) or greater in As_2Se_3 and in many other chalcogenide alloys [95] at a wavelength of 1550 nm. This is a high index change as compared to that produced by photodarkening (typically $\delta n = 0.05$ at $\lambda = 1550$ nm) in As_2Se_3 [53]. The non-linear refractive index of the glass has also been shown to increase [96] with Ag doping. Reference [97] reports up to 28 atomic % of silver can be dissolved in $GeSe_3$ and reference [98] reports that up to 40 atomic % can be dissolved in some chalcogenide glasses.

Compared to photodarkening [82], metal doping of As_2Se_3 films not only gives a higher index change but also results in lower solubility of Ag doped parts in alkaline solvents (as compared to the undoped regions). The silver concentration profile in the glass is typically step-like and follows the gradient of the illumination intensity with a sharp diffusion front [92, 53]. This property enables realizing high-index

contrast, fully etched waveguides in As_2Se_3 [99, 65].

One other phenomenon that goes hand-in-hand with silver dissolution in the vertical direction is the lateral diffusion. This is largely an undesirable process which restricts accurate dimensional control of the microphotonic structures fabricated. It has also been reported that the lateral diffusion is much quicker when a conductive film covers the dielectric substrate [100]. This process is described in Section 3.2.5.

The etch resistivity shown by silver doped glass regions has been investigated for resists for lithography [101], ion selective membranes for chemical sensors [102] and for making integrated optic devices [92, 103, 65]. Photodoped chalcogenide glasses exhibit reduced tendency for photo-oxidation and photodarkening [104], thereby improving their operational and processing stability.

Silver dissolved in chalcogenide glasses also tends to form nanoparticles (silver dots), which can be used for ultrafast optical switching [53]. These silver nanoclusters are also investigated as potential broadband sensitizers to increase the pumping efficiency of rare-earth ions for active application [105].

Pursuing Ag doping for making integrated optic devices was a natural extension to the ongoing chalcogenide glass research at TRLabs-Edmonton. Photodarkened shallow etched waveguides have been demonstrated in a previous work [82]. Although waveguides have been demonstrated using photodarkening, these induced changes can relax, rendering the stability of the devices questionable over a long period of operation. As a result, alternative method to realize high-index contrast strip waveguides using Ag doping and subsequent etching are considered more promising and were investigated in this work.

3.2 Silver doping experiments with As_2Se_3

3.2.1 Process Development

To realize the potential of chalcogenides for integrated optics, a key task is to develop techniques for patterning them into micron-sized low loss optical devices. A typical waveguide fabrication starts with depositing a suitable undercladding, having lower index than the chalcogenide glass, on a silicon substrate by spin coating.

The polymer undercladdings used in this work needed to have excellent chemical, thermal, and mechanical compatibility with As_2Se_3 and $Ge_{33}As_{12}Se_{55}$. It is also important that the polymer is resistant to the wet chemicals used in the fabrication process. These chemicals include acetone needed to perform the lift-off process, photoresist developer, IPA and water used to clean the sample and monoethanolamine (MEA) used in etching the As_2Se_3 glass. Moreover, a reasonably good coefficient of thermal expansion (CTE) match between materials was necessary to avoid film cracking and delamination [59].

Dry etch grade benzocyclobutene or BCB (Cyclotene 3022-63, Dow Polymers) was used as a robust undercladding. It is used in the microelectronics industry as a low-k dielectric, for planarizing, and as a passivating and protective layer [106]. BCB is a high glass transition temperature thermo-setting polymer. As_2Se_3 films were found to adhere very well to BCB undercladdings [59]. The CTE is approximately $21x10^{-6}$ $°C^{-1}$ and $52x10^{-6}$ $°C^{-1}$ for As_2Se_3 and BCB, respectively. The refractive index of BCB is approximately 1.5 as compared to 2.8 for As_2Se_3 at 1550 nm.

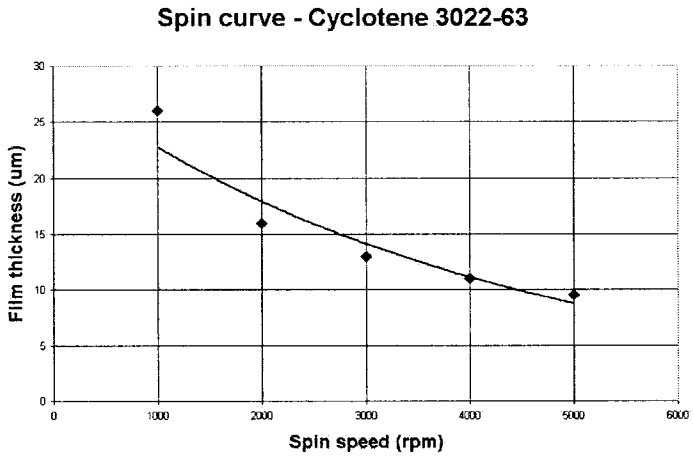

Figure 3.2: Measured spin curve for BCB polymer. The line denotes an exponential curve fit to the measured values.

After the silicon wafer was cleaned using the process described in Appendix A, an adhesion promoter was spin coated onto the silicon wafer so as to improve the adhesion of BCB to the silicon surface. BCB is then spin coated, typically at 5000 rpm. The measured spin curve for BCB is shown in Figure 3.2. Edge bead removal

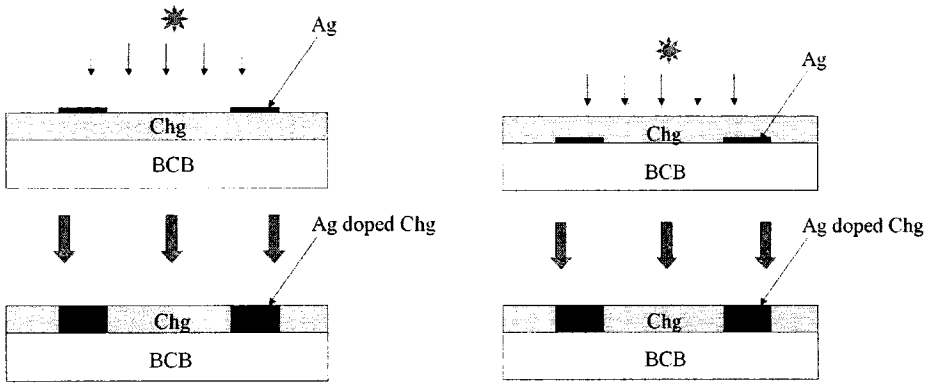

(a) Silver strips on top of the glass (b) Silver strips below the glass

Figure 3.3: Two ways of patterning silver lines for making waveguides.

is important since its presence adversely affects the resolution of the subsequent lithography step. The BCB film is then cured in a nitrogen ambient at 160°C for 1 hour to get a uniform undercladding layer about 10 μm thick. The processing recommendations from the manufacturer emphasize curing the polymer in the absence of oxygen for temperatures above 150°C [106]. The film is allowed to cool slowly to room temperature to avoid thermal shocks.

Typically, a 1 μm film of As_2Se_3 glass was thermally evaporated onto the BCB undercladding. The starting point for thermal evaporation was a commercially obtained bulk glass which was evaporated by resistive heating in molybdenum boats under a pressure of $2x10^{-6}$ Torr with a deposition rate of about 2 nm/s.

It should be noted that there are two ways to go about photodoping the glass, as shown in Figure 3.3. Each has its own advantages and disadvantages.

The first method (Figure 3.3(a)) is to pattern silver (99.99% pure sourced from Kurt J. Lesker Company, Clairton, Pennsylvania) on top of the glass. This has the advantage that the undissolved silver, if any, can be removed at a later time. Removal of any remaining silver will help in reducing the waveguide losses. The disadvantage would be that the high illumination intensity is needed to dissolve the metal into the glass as the light must penetrate the top metal layer and also reach the deepening Ag dissolution front into the glass for process completion. Note that the chemicals used to pattern silver on top of glass should not affect the glass.

The second method (Figure 3.3(b)) is to pattern silver below the glass, before the glass is deposited. This does not allow the removal of undissolved Ag layer after the photodoping process. However, the incident radiation can more easily penetrate the undoped glass and reach the metal dissolution front. This method was also found to lower the adhesion between the glass and the polymer under-cladding. A potential usefulness of this reduction in adhesion is discussed in Chapter 4. Since undercladding polymers chosen for this study showed good chemical resistance, the choice of Ag etchants is wider when patterning Ag on polymer versus on the chalcogenide glasses.

3.2.1.1 Etching Chalcogenide glasses

When it comes to wet etch recipes for chalcogenide glasses, very few papers mention the exact recipe they used. Further, there is considerable variation in the etching chemicals reported. Some of the information regarding etchants mentioned in the literature is summarized below.

- AsGeSeS glass etched with 0.6N NaOH at 22°C produced 1.57 nm/s etch rate for as-deposited films [102].
- Reference [107] reported 0.2N NaOH for etching As_2S_3
- For photodarkened As-S-Se films, commercial alkaline organic solutions produced by Hologramma were used as a negative developer, while aqueous NaOH solution doped by alkyl sulfonate, a surfactant, was used for amorphous As_2S_3 films as a positive developer [108].
- There also have been conflicting reports on the etching properties of NaOH. For example, [109] reports that the undoped regions of GaLaS resisted NaOH etch.
- Reference [110] reports the inability of non polar hydrocarbons to appreciably dissolve As_2S_3 at room temperatures. However, they report that polar etchants dissolved both as-deposited and annealed samples.

- Potassium cyanide has been reported to etch the Ag photo-doped region while NaOH etches the doped region [1].

- It has also been reported that $AgAsS_2$ and $AgGeS_2$ glasses were found to be stable in alkaline non-oxidizing solution, but dissolved in a 0.1M NAOH + 0.9M $NaNO_3$ solution at higher temperatures [53].

For As_2S_3, it has been found that mono-substituted amine like monoethanolamine is more reactive than di-substituted amines, such as di-ethyl amine [111]. In the most relevant literature for our work, an alkaline amine based solution was reported in the etching of Ag-As_2Se_3 [112].

3.2.1.2 Silver Etchant

An appropriate silver etchant is needed for patterning silver without attacking the glass or the photoresist. Acids are known to attack As_2Se_3 so HNO_3 was avoided [113]. Reference [109] used a solution of $Fe(NO)_3$ to remove silver from GaLaS glass.

The silver etchant that was used in this work was a mixture of CH_3OH : H_2O_2 : NH_4OH :: 4 : 1 : 1 by volume [114]. The solution was then aged for 3 hours before performing the silver etch. It was found to be a good choice, as it did not cause noticeable damage to the chalcogenide glasses. Samples were typically immersed in this etchant for 10 seconds to remove Ag films on the order of 30 nm thick.

3.2.2 Ag doped strip waveguides by direct patterning

It is desirable that a fabrication process be simple and use commonly available equipment. In all the experiments described in this work, unless otherwise mentioned, the starting point was cleaning of a prime grade 4 inch silicon wafer using pirahna clean (refer to Section A.2.1). This was followed by spin coating a 10 μm thick BCB undercladding.

Approximately 1 μm of As_2Se_3 was then thermally evaporated onto polymer BCB undercladding. Then, approximately 30 nm of silver was directly sputtered on top

[1] Prof. Tomas Wagner's, University of Pardubice, presentation to TRLabs photonics group

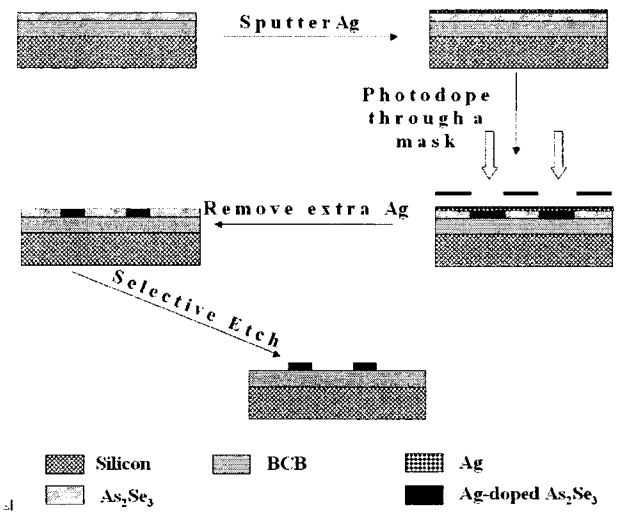

Figure 3.4: Process steps for making Ag doped strip waveguides by direct patterning

of As_2Se_3 film. Up to 40 atomic % can be dissolved in some chalcogenide glasses [98]. However, to minimize the absorption losses we chose to keep the silver concentration to ~4 atomic % which corresponds to dissolving 30 nm of silver in 1 μm of As_2Se_3.

This was followed by UV exposure through a mask for photodoping for 30 mins. A 30 minute UV exposure, with intensity of 17 mW/cm^2 and 41 mW/cm^2 at wavelengths of 365 nm and 400 nm, respectively, was found to be sufficient for complete dissolution of 30 nm of Silver on top of a micron thick As_2Se_3 film [115]. After the photodoping process, the excess silver was removed and undoped As_2Se_3 glass was etched away in MEA to get strip waveguides. The process steps are described in Figure 3.4.

After the photodoping process, the silver layer was etched away using the etchant described in Section 3.2.1.2. The etching of As_2Se_3 was largely unsuccessful in these initial experiments, with no apparent selectivity between the nominally doped and undoped regions. Neither MEA nor 0.6 N NaOH showed any etching action on the glass. Prolonged exposure to NAOH resulted in cracking of the glass film.

The inability to see any etch selectivity was attributed to the very fast reaction between silver and As_2Se_3. As_2Se_3 samples coated with Ag and subsequently kept

in the dark visibly dissolved all the silver within 24 hours. Hence, any part of the As_2Se_3 film that came in contact with Ag at any point in time during processing seems to show high etch resistance to the etchants tested. The importance of protecting the unwanted As_2Se_3 regions from coming in contact with Ag during any part of the process step was very clear. Silver dissolution in As_2Se_3 is reported to be one of the fastest among chalcogenide glasses [116].

3.2.3 Modified 'Lift-Off' process for Ag doped strip waveguides

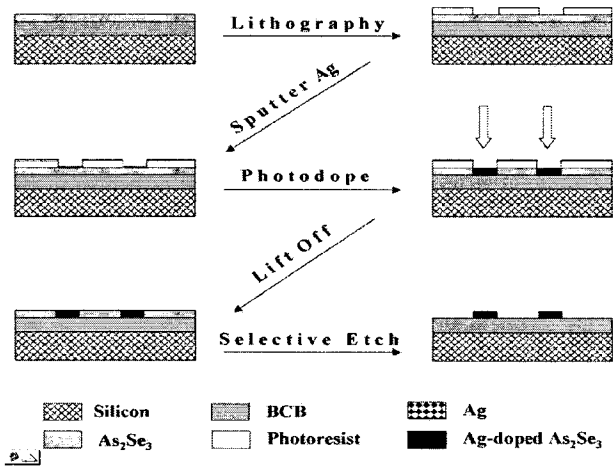

Figure 3.5: Modified Lift-off process used for Ag doped waveguide fabrication.

A more successful process for making Ag doped strip waveguides was found after the observations described in Section 3.2.2. A liftoff process was used to selectively dope Ag in the regions desired. Figure 3.5 shows the complete fabrication steps used for making Ag doped strip waveguides in chalcogenide glass.
Approximately 1 μm of As_2Se_3 was evaporated on a 10 μm thick BCB undercladding layer. Photolithography was performed using HPR504 positive photoresist and 354 developer to define the waveguides of varying widths on the glass. About 30 nm of silver was sputtered followed by photo-doping with UV light on a standard photolithography exposure equipment (ABM) through a mask for 30 mins.
It should be noted that the silver dissolution commences at the time of Ag sputtering on the glass. The sputter glow discharge aids in this process. The most successful fabrication was achieved when a step by step Ag deposition was performed. About

2.5 nm of silver was deposited each time and this process repeated until the desired thickness of silver is deposited (typically 30 nm). Silver dissolution occurs due to the thermal and glow discharge exposure while sputtering.

The photoresist was subsequently washed off with acetone followed by a short dip in a silver etchant, to remove the excess silver on the glass. We had success with MEA as a negative etchant. MEA at 50-65°C was used to etch the undoped glass and produced good quality features. The etching time for 1 micron of glass was about 90 seconds when MEA was kept at 60°C. Proper cleaning of the sample after etching was very important as residual MEA was observed to degrade stored samples. A short dip (5-10sec) in the silver etchant was seen to improve the surface quality of the structures as it acts as cleaning agent for organic compounds. It should be noted that the silver etchant recipe is essentially an RCA clean at room temperature described in Section A.2.2.

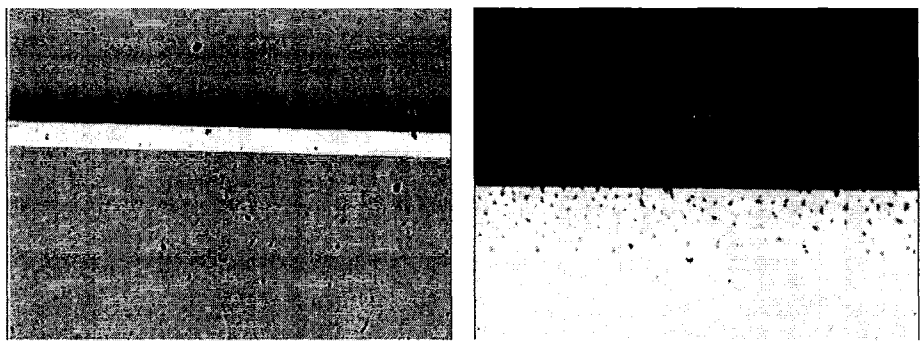

(a) Top View of a silver doped As_2Se_3 strip waveguide.

(b) End view of a silver doped As_2Se_3 strip waveguide. The BCB undercladding layer is $\sim$10 μm thick.

Figure 3.6: Microscope images of a silver doped As_2Se_3 strip waveguide

Figure 3.6 and 3.7 shows typical Ag doped chalcogenide strip waveguides, fabricated by the liftoff process using the 'step by step' doping approach. No upper cladding was deposited on these waveguides. Note that the waveguide sidewalls are quite vertical, and reasonably smooth.

Both the effect of annealing and variations in photodoping time were investigated, in terms of their effect on waveguide feature quality. In this experiment, a 4 inch silicon wafer was first spun cast with BCB followed by thermal evaporation of $\sim$1

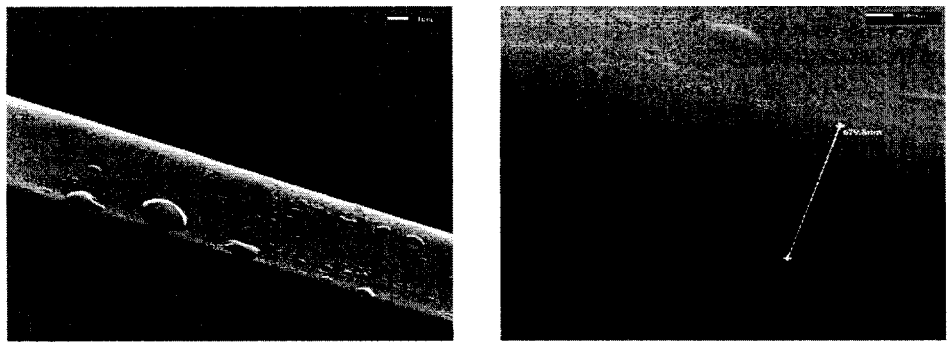

(a) SEM image of top view of a silver doped As_2Se_3 strip waveguide

(b) SEM image of side view of a silver doped As_2Se_3 strip waveguide showing an etch depth of $\sim$ 680 nm.

Figure 3.7: SEM micrographs of the fabricated Ag doped As_2Se_3 Strip waveguide

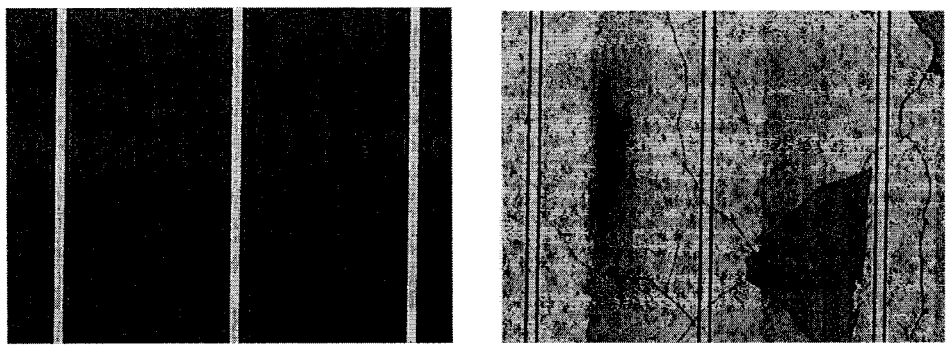

(a) Typical waveguides fabricated using annealed As_2Se_3

(b) Cracking of photodoped, un-annealed As_2Se_3 on MEA etching

Figure 3.8: Typical fabrication result from annealed and un-annealed As_2Se_3

μm of As_2Se_3. The sample was divided into four parts, A, B, C and D. A and C were annealed (and cooled to room temperature gradually) at 165°C for 1 hour in nitrogen ambient, while B and D were un-annealed. A and B were patterned with UV lithography with a positive photoresist, HPR504. Samples C and D were patterned with DUV lithography with a positive DUV resist, UV5. All the samples were then coated with $\sim$30 nm of silver. Each of the samples were now cleaved into 3 pieces (X_i where X = A,B,C and i = 1,2,3) to test the effect of exposure time. X_1's were exposed for 10 seconds, X_2's for 5 mins and X_3's for 15 minutes. After exposure, all samples were dipped in the silver etchant followed by removal of photoresist.

All the annealed samples (A_i's and C_i's), except A_1 survived the full process. All

the unannealed samples (B_i's and D_i's) cracked during etching the chalcogenide in MEA. The results are tabulated in Table 3.2. Figure 3.8 shows typical waveguides fabricated using annealed and un-annealed glass.

Table 3.2: Effect of annealing on waveguide fabrication

	Annealed		Un-annealed	
	A	C	B	D
10 sec	Peeled away	Good features	Film cracked	Film cracked
5 mins	Good features	Good features	Film cracked	Film cracked
15 mins	Good features	Good features	Film cracked	Film cracked

3.2.3.1 Problems with Liftoff Process

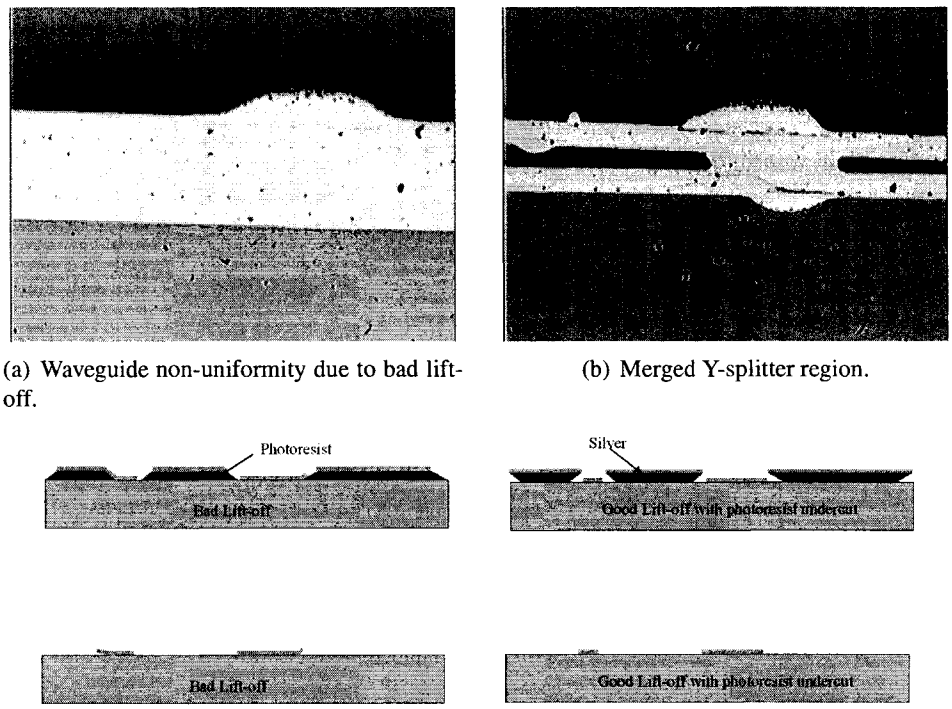

(a) Waveguide non-uniformity due to bad lift-off.

(b) Merged Y-splitter region.

(c) Bad liftoff with numerous silver tendrils.

(d) Good liftoff produced using a good photoresist undercut.

Figure 3.9: Problems with lift-off process in Ag doped waveguide fabrication, indicating the speed of the reaction between Ag and As_2Se_3

Figures 3.9(a) and 3.9(b) show common defects that were observed on the final devices. These defects illustrates the need for a clean lift-off process (Figure 3.9(c)

and 3.9(d)). The occurrence of such defects was considerably reduced by etching off all the silver before removing the photoresist. This step protects the As_2Se_3 from coming in contact with stray silver tendrils after the photo-doping step.

3.2.3.2 Spots on the devices fabricated

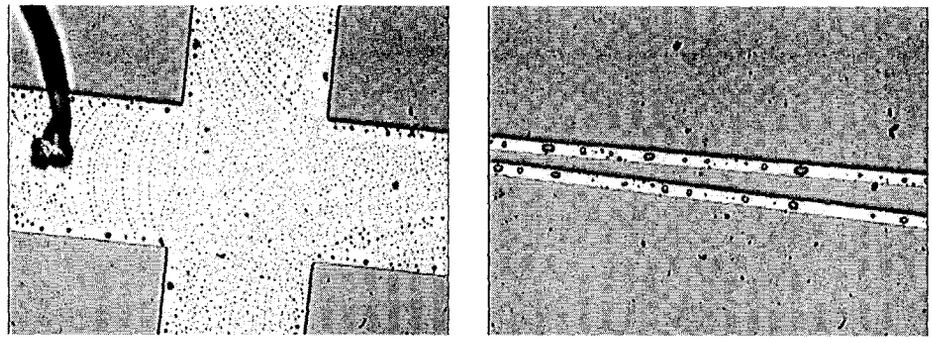

(a) Typical spots observed on an allignment mark

(b) Spots on waveguides

Figure 3.10: These spots were common on the etched structures

Circular spots were observed consistently on most of the waveguides fabricated as shown in Figure 3.10. The nature of these circles was not determined, and remains to be investigated. Formation of silver clustering has been reported in the literature with plausible advantage in non-linear optical application and as broad band sensitizers [105].

3.2.3.3 As_2Se_3 strip waveguides with torlon uppercladding

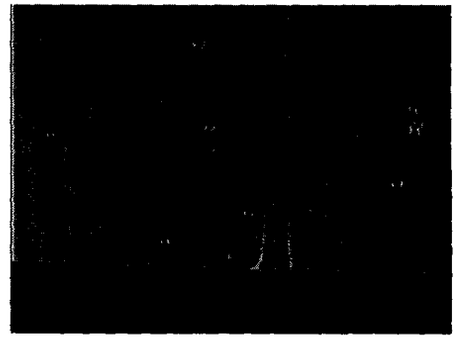

Figure 3.11: Partially etched structures with tapering caused by lithography on rectangular sample

One of the most important, yet mundane, parts of integrated optics research is to obtain well cleaved samples for light coupling experiments. We have found that device facets are perhaps the most crucial part in successful characterization of microphotonic components. In practice, one can't afford to work with full 4 inch wafers all the time. A full wafer would need to be cleaved into smaller samples which might again require fresh cleaves before optical characterization.

To avoid the need for cleaving after waveguide fabrication, small pre-cleaved substrates were used in some experiments. Working with small samples causes other fabrication difficulties, especially related to spin coating of polymer and photo-resist layers. The tapering of a waveguide, as shown in Figure 3.11, is attributed to the non-uniformity (edge bead) that forms while spin coating a small rectangular sample with a photo-resist. One way to avoid such tapering and still work with smaller samples is to spin cast the full wafer with the required resist and then cleave into smaller samples.

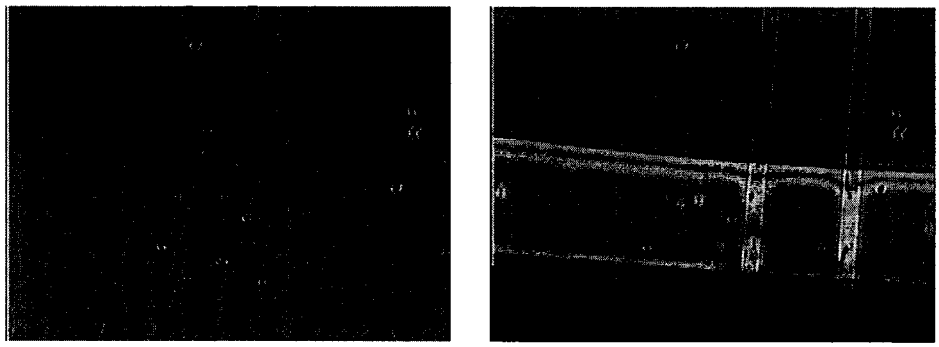

(a) Ysplitters covered with PAI uppercladding (b) Stretching of Torlon uppercladding

Figure 3.12: Strip waveguides with PAI uppercladding

One other way to improve cleaves is to spin a robust uppercladding. An uppercladding will also reduce the scattering loss and act as a protective layer for packaging the final device. The upper cladding we used in this case was polyamide-imide (PAI) polymer, TORLON AI-10, sourced from Solvay Advanced Polymers [117]. PAI has a refractive index of $\sim$ 1.65 at 1550 nm and thin films can be easily made using spin casting. Properties of this polymer are described in Chapter 5.

The Ag doped strip waveguides fabricated in Section 3.2.3 were coated with a 4

μm thick PAI layer. 60 g of AI-10 powder was dissolved in 150 mL N,N-dimethyl formamide (DMF). AI-10 powder dissolved in DMF was stirred continually and kept at room temperature for about 4 hours. The solution was filtered using a 1 μm particle retention filter to remove large impurities [86]. The film was then cured at 160°C in a nitrogen environment for 1 hour and allowed to cool down to room temperature slowly.

Figure 3.12(a) shows the Ag doped As_2Se_3 strip waveguides with PAI uppercladding. Figure 3.12(b) shows the cleaved sample indicating that the PAI layer might not have been cured properly. Upon further investigation it was found that this kind of stretching of PAI occurred even after curing according to the processing manual from the manufacturer [117]. Changing the solvent used to spin cast PAI to N,N-Dimethylacetamide (DMAc) produced consistent cleaves as described in Section 5. SEM pictures were not feasible because the PAI uppercladding planarizes the major waveguide features. By far the best cleaves (Figure 3.6(b)) were obtained when cleaves were made in samples with the cleaved edge longer than $\sim$ 4 cm.

3.2.4 Photodoping using white light source

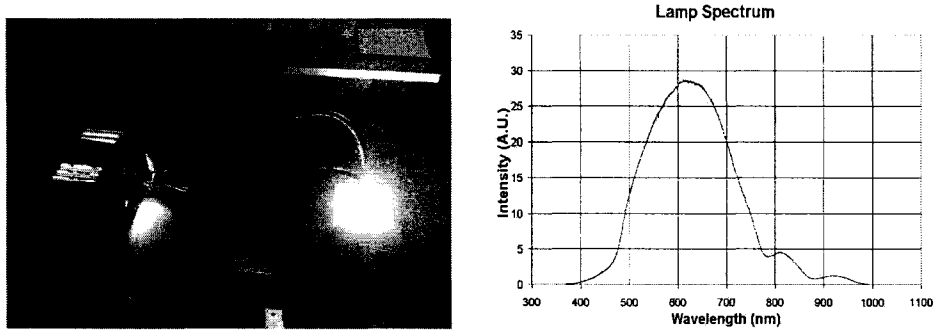

(a) Photodoping using white light source

(b) White light lamp spectrum

Figure 3.13: White light photodping experimental setup

A conventional UV source in a lithography exposure system was used for photodoping in Section 3.2.3. Using the lithography UV source for extended period of time, as in the case of photodoping, affects the exposure dosage for its original intended lithography purposes. The UV lamps also have a short lifetime and replacements

are often costly. Hence, white light was used for the photodoping process. As in the case of UV exposure, 30 minutes was also found to be sufficient to dissolve 30 nm of silver on top of 1 μm thick As_2Se_3 film. Figure 3.13(a) shows the setup used for the photodoping. The spectrum of the white light, Figure 3.13(b), is centered around 632 nm.

(a) Top view of the channel waveguide. The colour contrast between the doped and undoped region can be seen

(b) Waveguiding pictures of the channel waveguides using white-light photodoping

Figure 3.14: Channel waveguides using white light photodoping

An added advantage in using this longer wavelength source is that that the light penetration depth into the chalcogenide is higher. UV light is absorbed in the top surface of the film and prolonged exposure might tend to result in lateral diffusion near the surface rather than driving the silver vertically into the glass. This point is discussed further in Section 3.2.5.3. The end view SEM pictures of waveguides Figures 3.15(b) and 3.21(e) illustrates the lateral diffusion. Widening of waveguide structures is discussed in detail in Section 3.2.5.

Channel waveguides were fabricated using the procedure described in 3.2.3 but using white light for photodoping. The photoresist was removed and silver was etched to realize a channel waveguide. The chalcogenide glass was not etched in this case. Figure 3.14(a) shows the channel waveguide fabricated. The subtle color contrast between the silver doped region and the undoped As_2Se_3 region can be seen in Figure 3.14(a). Light coupling and waveguiding was confirmed at 980 nm wavelength and is shown in Figure 3.14(b). These waveguides exhibited good confinement.

3.2.5 Lateral Diffusion in Ag doped As_2Se_3

Almost all the waveguides fabricated using As_2Se_3 showed widening of the features relative to the features defined in the photoresist. Lateral diffusion in some Ag doped chalcogenide glasses is a well known problem [87]. The lateral diffusion of silver has been monitored by Rutherford back-scattering (RBS) [118] or by reflectance measurements [100]. This section describes attempts to predict the lateral diffusion from our experimental results.

3.2.5.1 Widening of final features

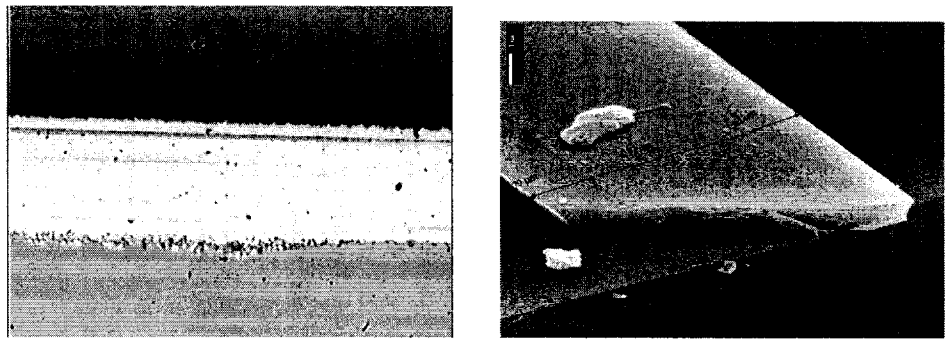

(a) Microscope picture showing intended and final waveguide widths.

(b) Observed lateral diffusion. Patterned waveguide dimension can also be seen here.

Figure 3.15: Lateral diffusion observed in fabricated waveguides.

Figures 3.15(a) and 3.15(b) show typical strip waveguides. A clear demarcation between the intended widths and final widened features is visible. Improper photolithography was initially suspected to be the cause of widened features and was monitored closely for dimensional accuracy. Patterning waveguides of widths less

than 4 μm consistently using conventional UV lithography was non-trivial.

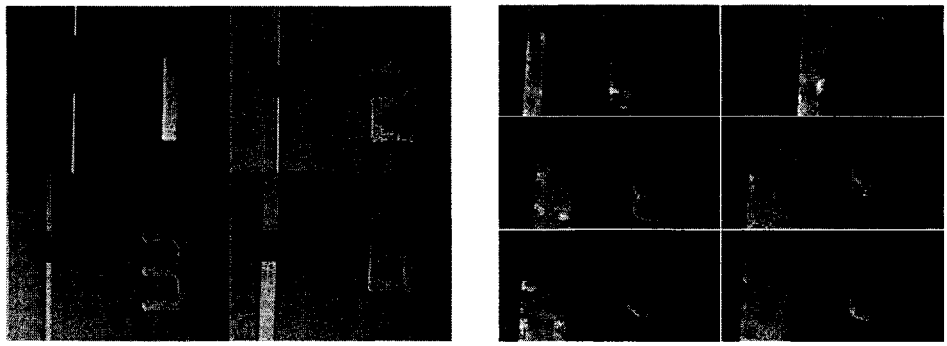

(a) Very good dimension control obtained using DUV lithography

(b) Widening of features observed in As_2Se_3.

Figure 3.16: Comparison of patterned feature dimensions to final waveguide dimension. The spacings between the lines on the inset corresponds to 10 μm.

Deep UV lithography at 248 nm was employed to pattern features accurately as shown in Figure 3.16(a). Photodoping was performed using the white light source and undoped glass was etched away using MEA at 50°C. The widening of waveguides is shown in Figure 3.16(b). This proved the existence of lateral diffusion of silver in As_2Se_3.

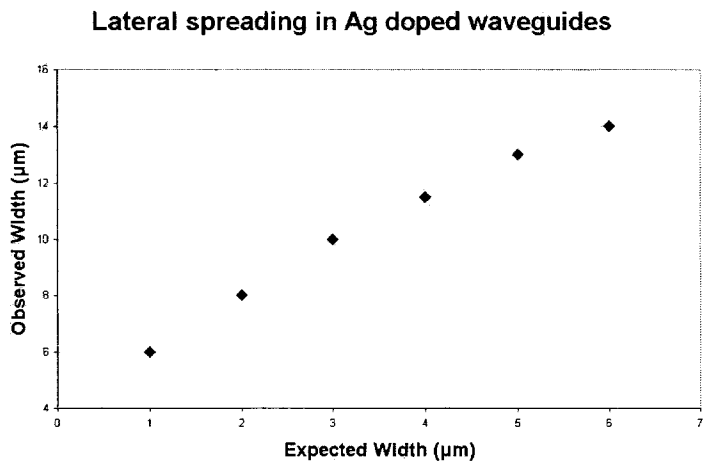

Figure 3.17: Plot of intended and final width

From the plots of the intended versus final width as shown in Figure 3.17, it might be possible to pre-compensate for the lateral diffusion. To a first order approximation the dependence can be considered to be linear. For example, assuming this

is predictable and repeatable, a 0.8 μm patterned structure in photoresist would widen to 1 μm (refer to Figure 3.17). E-beam lithography was utilized to pattern submicron waveguides, bends and ring resonator structures to test this proposition and is described in Section 3.2.6. It should be mentioned that the extent of lateral diffusion is expected to depend on many factors, including light intensity and wavelength, starting thickness of the silver layer, thickness of the chalcogenide film and size of the mask feature. A more detailed study is required to understand the impact of these various factors.

3.2.5.2 Mechanism of Ag dissolution

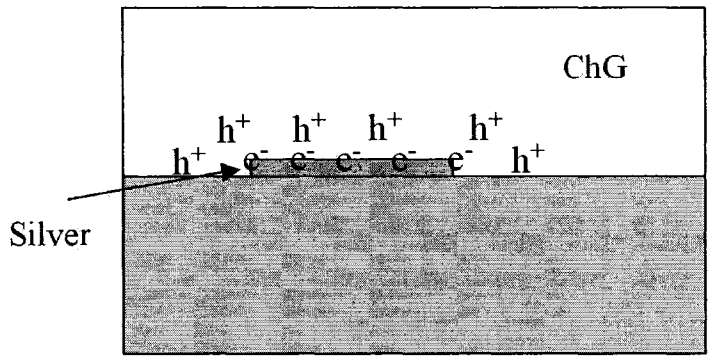

Figure 3.18: Upon illumination electron and hole pairs are created at the interface between metal and glass.

Chalcogenide glasses are amorphous semiconductors. Exposure of the interface of the metal-chalcogenide or of the interface of the doped-undoped part to light of energy close to the band gap of chalcogenide glass creates electron-hole pairs (refer Figure 3.18). Since the glass is a p-type semiconductor the electrons are captured quickly while holes and mobile silver ions move into the undoped region. The field developed by the movement and capture of charge carriers eventually slows down the silver doping front until it reaches equilibrium [53].

In the case of photodoping, the silver dissolution is largely in the direction of illumination (vertically into the As_2Se_3 film) but it also proceeds in the lateral direction to some extent. It should be noted there are other means (such as thermal and ion-

beam) of creating hole-electron pairs. Thermally activated silver diffusion goes hand-in-hand with photodoping even at room temperature [92].

3.2.5.3 Possible explanation of observed widening

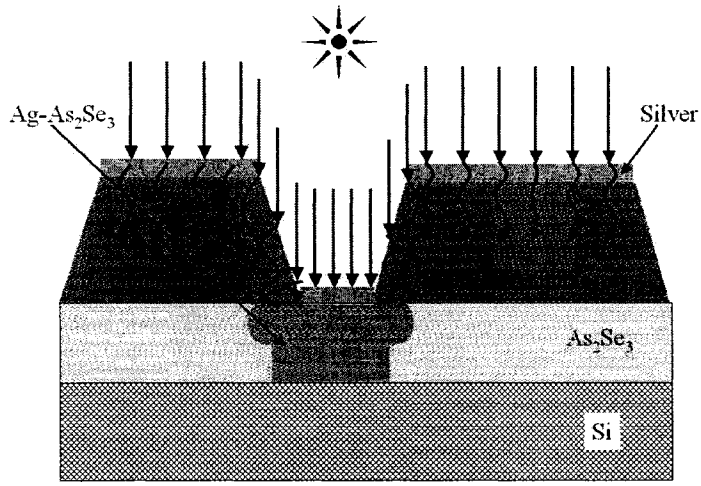

Figure 3.19: Possible explanation for lateral diffusion observed in this work

Several factors might contribute to the widening of the waveguides at the top surface as shown in Figures 3.15(b) and 3.21(e). It is well established that silver diffusion follows the intensity gradient of light. In simple terms, the silver tends to accumulate in regions of highest light intensity [99].

One factor contributing to lateral diffusion might be the photoresist morphology as shown in Figure 3.19. The photoresist with 30 nm silver that is used to block the light from reaching the glass surface outside the intended waveguide area might not be doing a good job. The slanted side-walls of the photoresist would not be able to block all the light from reaching the Ag doped-undoped chalcogenide interface. This results in lateral silver diffusion predominantly in the upper surface of the glass.

3.2.6 Ring Resonators using E-beam Lithography

As mentioned in Section 3.2.5.1, pre-compensating for the lateral diffusion was attempted using E-beam lithography. The 'lift-off' process (refer to Section 3.2.3)

was used to realize Ag doped high index contrast structures in this case.

Conventional contact lithography cannot give the necessary dimensional control required for fabricating high-index contrast ring resonators. The limiting feature size in high index contrast ring resonators is the coupling gap and length of the coupling region. Hence a Raith 150 Scanning electron beam lithography (SEBL) system was used to pattern these structures. Since accurate control over lateral diffusion was not possible, a ring resonator based on MMI couplers was attempted (refer to Section 2.4.4.2).

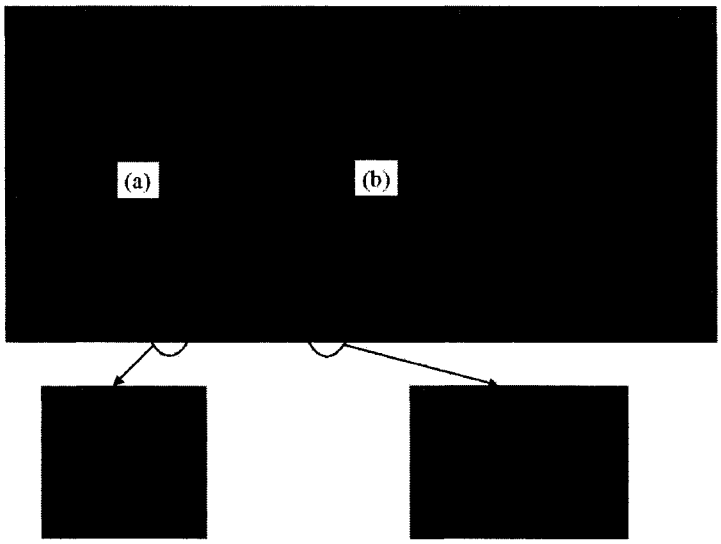

Figure 3.20: Two common types of stitching errors observed during E-beam lithography. (a) shows a gap and (b) shows a misalignment

Silicon wafers were first spin-coated with a 10 μm BCB undercladding. Then, a 1 μm thick As_2Se_3 film was thermally evaporated. Polymethylmethacrylate (PMMA - 950K A2), a positive E-beam resist, was spun cast at 4000 rpm and baked for 30 mins at 180°C. Then, Aquasave, a water soluble conductive polymer from Mitsubishi Rayon was used to prevent charging during E-beam lithography [119] [2]. PMMA was exposed using a Raith 150 SEBL system followed by the removal of the Aquasave. The PMMA was developed and 30 nm of silver was sputtered followed by illumination with white light for 30 mins. After the photodoping process,

[2]A thin layer of gold on top of PMMA also eliminated the charging problem but was found to modify the the E-beam exposure dosage requirements.

excess Ag was etched using the Ag etchant. The PMMA was removed completely and a wet etch was performed using MEA at 50°C to obtain Ag doped As_2Se_3 strip waveguides.

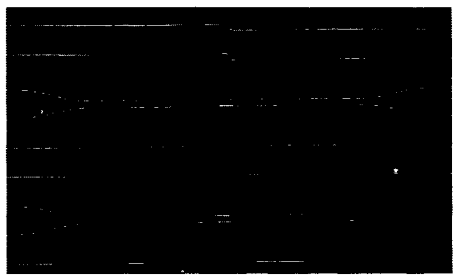

(a) Microring features patterned using E-beam lithography.

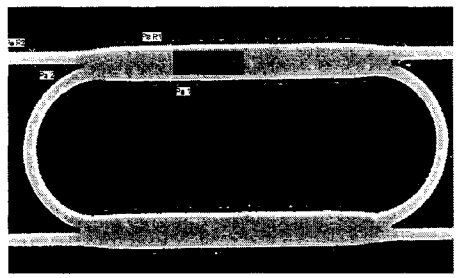

(b) Microring resonator in Add-drop configuration with MMI coupler regions

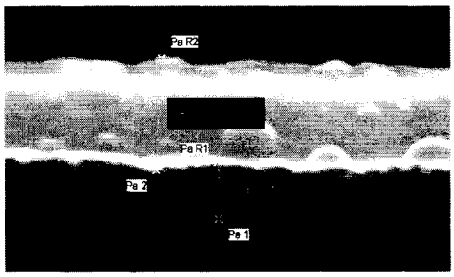

(c) Top view of the bus waveguide

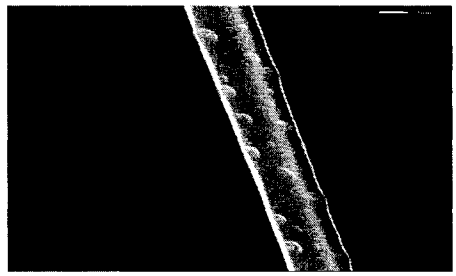

(d) Oblique view of the bus waveguide

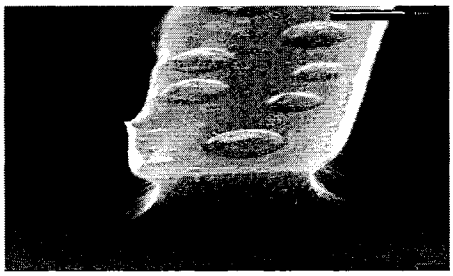

(e) End View of a bus waveguide.

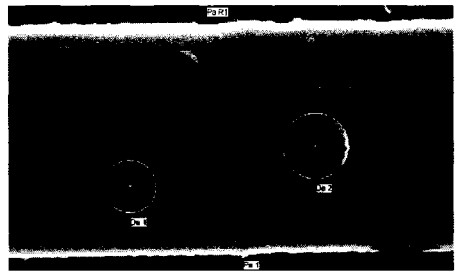

(f) Spots on the waveguide

Figure 3.21: Ring Resonators using SEBL

Although high dimensional control was achieved by E-beam lithography, almost one in every four samples had stitching errors as seen in Figure 3.20.

The fully etched silver doped structures are shown in Figure 3.21. Numerous circular spots as described in Section 3.2.3.2 are also seen in Figure 3.21(f). These waveguides were not of sufficient quality for optical characterization. However, it is expected that further process optimization could reduce the roughness and defects. The Ag doping process clearly shows potential for accurate fabrication of

sub-micron high index contrast waveguide structures.

3.2.7 Loss measurement

Light guiding was studied in silver doped strip waveguides in As_2Se_3, with widths greater than 8 μm, fabricated using the processes described in Section 2.3.3. Fabry-Perot loss measurement was not possible since the waveguides tested were not single moded at 1550 nm. Reasonably good edges were obtained on cleaving samples using a diamond tip as seen in Figure 3.22(a).

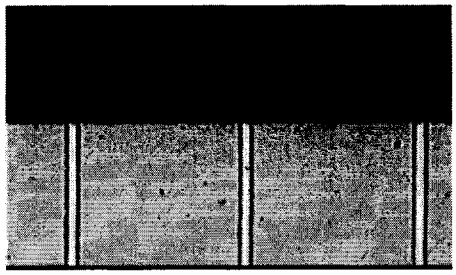

(a) Cleaved waveguide ends

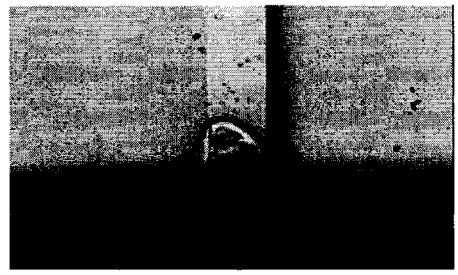

(b) Waveguide end burnt by 1480 nm laser

(c) Top view with end view inset at 1480 nm

(d) Top view with end view inset at 980 nm

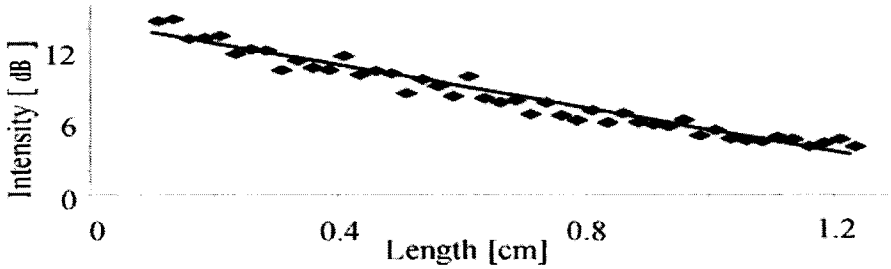

(e) Ag strip waveguides loss measurement at 1480 nm pickup fiber

Figure 3.22: Light coupling and loss measurement of the strip waveguides

A small core, high numerical fiber aperture (Nufern part number) was used to butt

couple to the sample waveguides. A polarization controller at the input end and a polarization beam-splitter cube at the output was used to selectively couple TE or TM modes in the waveguide. An objective lens was used to focus the end facet onto a detector or a camera. A well defined spot is indicative of good coupling and well confined waveguiding.

Figure 3.22(c) shows the top view of a light coupling experiment at a wavelength of 1480 nm. Due to the presence of a large amount of background light in the image an accurate loss measurement using the scattered light image could not be performed. To circumvent these problems, a multimode pick up fiber was used to collect the scattered light (refer to Figure 3.22(e)). This technique, shown in Figure 2.17, also necessitated that the lasers used were sufficiently powerful to get appreciable scattered light picked up by the fiber. Hence only 1480 nm and 980 nm lasers were used for characterizing waveguides in this way. Figure 3.22(b) shows a waveguide facet burnt by the high power 1480 nm laser.

Scattered light intensity along the waveguide length was plotted versus distance to estimate the propagation losses. Bright spots near the input and output ends were neglected to ensure that none of the light scattered near the facets influenced the loss estimation.

As shown in Figure 3.22, the Ag-doped guides show strong guidance of 980 nm (refer Figure 3.22(e)) and 1480 nm (refer Figure 3.22(c)). Analysis of scattered light at 1480 nm, using pickup fiber (Figure 3.22(c)) produced an estimate for the propagation loss of ~ 9 dB/cm. As_2Se_3 exhibits bulk absorption in the 2-4 dB/cm range at 980 nm [116], and Ag-doping is known to decrease the bandgap of the glass. The transmission spectrum undergoes a red-shift leading to an increase in absorption as compared to undoped glass. Thus, some portion of the measured propagation loss can be attributed to material absorption. Side-wall roughness induced scattering losses would also be a major contributor to the high losses observed.

3.2.8 Inconsistencies in Etching the glass

There is very little data in the literature regarding etchants specific to chalcogenide glasses. A prolonged dip in any wet etchant has generally been found to be undesir-

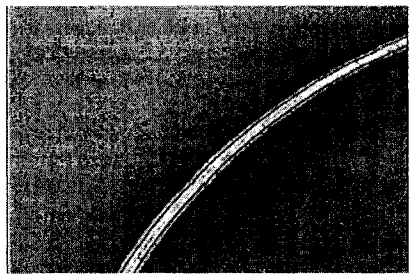

(a) Rough sidewalls after MEA etch on an bent waveguide patterned using E-beam lithography

(b) Rough sidewalls after MEA etch on an straight waveguide patterned using E-beam lithography

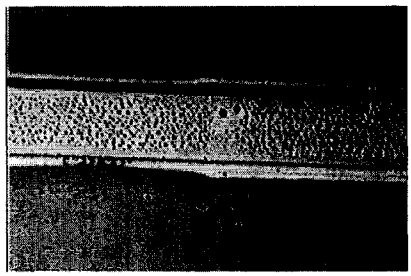

(c) Rough sidewall features remaining after 90 seconds (900 nm) of MEA etching patterned using UV lithography.

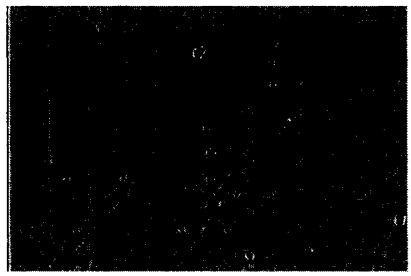

(d) Typical cracking of As_2Se_3 film observed during NaOH and NH_4OH etch

Figure 3.23: Inconsistencies in etching As_2Se_3 glass

able in out work. In one of the earlier works, etching As_2Se_3 more than $\sim$ 100 nm was not possible as the glass was found to crack if left in the etchant for extended periods [120]. NaOH and NH_4OH, some of the commonly mentioned etchants in the literature (refer to Section 3.2.1.1) were tried. The slow etch rate necessitated prolonged dipping in NaOH and NH_4OH resulting in cracking and peeling of the As_2Se_3 film. MEA diluted with water and a 50-50 mixture of MEA and NaOH were also tried without success, as shown in Figure 3.23(d).

By far, MEA at 50°C provided the best results among the etch recipes tested. MEA diluted with water required longer time in the etchant, causing cracking of the film in many places. NaOH, NH_4OH and their mixtures with MEA were the worst in terms of causing cracks in the film (refer to Figure 3.23(d)). It is also known that As_2Se_3 is attacked by hot water, without any evidence of selectivity between doped and undoped regions. Thus, dilution with water only reduces the potency of the MEA etch selectivity. However, it helps in cleaning MEA off the substrate after

etching due to the reduction in MEA viscosity. Nevertheless, pure MEA at 55°C gave the best results and etched 1 μm of As_2Se_3 in about 90 seconds.

It is very important to clean the chalcogenide surface after the MEA etch to avoid surface damage during subsequent storage. On a sample that is not properly cleaned, the surface damage can be observed within 24 hours. It was also found that a short dip in Ag etchant produces cleaner results. As discussed in Sections A.2.2 and 3.2.1.2, the Ag etchant used here is essentially a mild RCA cleaning agent. This Ag etchant seemed to assist in the removal of the viscous MEA. The MEA was otherwise difficult to remove completely when only DI water was used.

3.3 Silver doping experiments with $Ge_{33}As_{12}Se_{55}$ and $Ge_{28}Sb_{12}Se_{60}$

Two other commercially available glasses were subsequently used for similar Ag doped waveguide fabrication. These were $Ge_{33}As_{12}Se_{55}$ (IG2) and $Ge_{28}Sb_{12}Se_{60}$ (IG5) or AMTIR-I and AMTIR-II bulk samples were sourced fom Vitron (Germany).

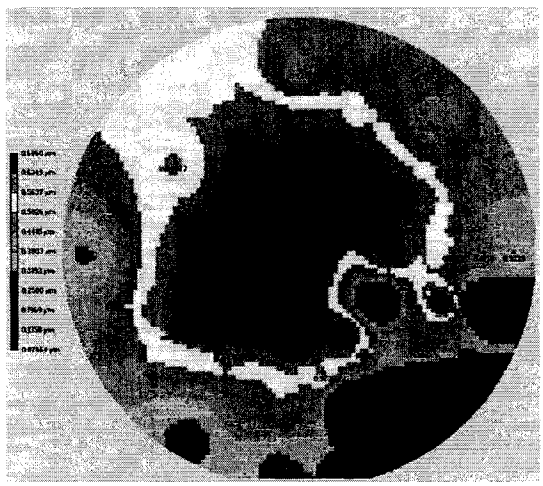

Figure 3.24: Colour map of IG2 film thickness over a 4 inch wafer

Initial IG2 and IG5 film development was performed using PLD (refer to Section A.3.4). Figure 3.24 shows the typical uniformity achieved by PLD. One of the first things observed with IG2 samples deposited by PLD was their robustness on

cleaving compared to As_2Se_3. Ge-based chalcogenide glasses are well known to be mechanically stronger than As-based chalcogenide glasses.

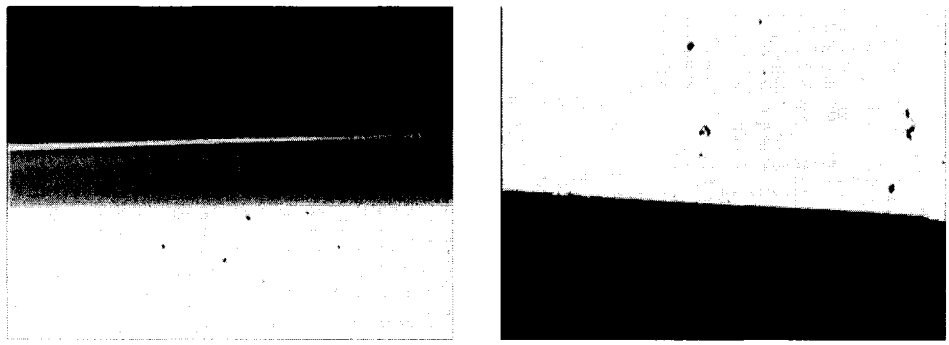

(a) End View of the cleave (b) Top View of the cleave

Figure 3.25: Better cleaves with IG2 film made by PLD

IG2 glass was thermally evaporated on to a silicon wafer that had been spin coated with a BCB undercladding. The IG2 thickness was measured to be $\sim$1.3 μm and was annealed at 250°C for 1 hour in a nitrogen ambient. The wafer was patterned using HPR504 resist by the process shown in Figure 3.5. It was then coated with a 30 nm layer of silver. Photodoping was performed for 1940 seconds with a UV lamp (365 - 400 nm, 20 - 60 mW/cm^2) in a mask aligner. The excess silver and the photoresist were removed. The wafer was then etched for 4 mins in MEA at $\sim$65-75°C was used to etch the undoped region and Ag was removed using brief dip in Ag etchant. A profile of the etched edge gave an estimate for IG2 thickness of 1.3 μm. One of the regions of large opening on the mask and was observed before and after photodoping and after etching in MEA and is shown in Figure 3.26.

Fabrication of Ag doped waveguides was attempted using the same process as in the case of As_2Se_3 (Section 3.2.3). The silver etchant described in 3.2.1.2 was used and was found not to have any visible damage to IG2/IG5 surface. Both IG5 and IG2 showed higher resistance to MEA compared to As_2Se_3. The etchant needed to be heated to about 60°C or greater in order to obtain an appreciable and observable etching of the undoped glass. The results of a basic waveguiding experiment in IG5 glass are shown in Figure 3.27.

After the doping and the strip waveguide development, no waveguiding was ob-

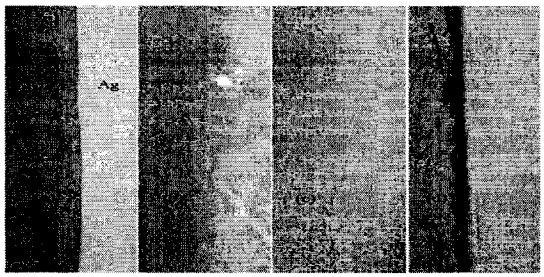

Figure 3.26: Silver dissolution in annealed IG2 glass (a) Before doping, (b) After doping, (c) After removing excess silver, (d) After 4min etch in MEA.

(a) Top view of 980 nm light coupled through IG5 strip waveguide

(b) End view of 980 nm light coupled through IG5 strip waveguide

Figure 3.27: IG5 ($Ge_{28}Sb_{12}Se_{60}$) - Ag doped and etched (390 nm) waveguide - 980 nm light coupling in strip loaded waveguiding

served though the strips. However, only a strip-loaded action was seen. The thickness of the film was measured to be 390 nm which apparently did not support a guided mode. Light propagation experiments using a slab waveguide of IG5 showed that the film did not guide light. Once the thermal evaporator was set up, as a continuation to the As_2Se_3 work, IG2 was chosen for further Ag doping studies.

From what was learnt and inferred from the silver doping experiments in As_2Se_3, it made sense to pattern Ag on the undercladding followed by glass deposition to ensure better light penetration needed for Ag doping. What emerged (Figure 4.6) as a result of this experiment is what is described in the next chapter. Thin film deposition by PLD was abandoned due to the inability to produce reasonable uniformity over a 4 inch silicon wafer (refer to Figure 3.24). To obtain better film uniformity all the subsequent experiments described in Chapter 4 were done using thermal evaporation.

Chapter 4

Patterned delamination in silver doped chalcogenide glasses

In this chapter a method to fabricate self-assembled hollow micro-channels is discussed. The mechanism for this self-assembly is also described.

4.1 Introduction

The path from atoms to the stars is believed to be attributable to some kind of a self organization from simpler constituents under appropriate conditions. The beauty of such complex self-arrangements, for example, atoms, crystals, DNA, the human brain, has fascinated mankind for ages. Even in real life, societies have usually been moving towards a self-consistent, self-organized, stable state. By controlling the amount of stress and adhesion in a chalcogenide thin film layer on top of a pre-patterned layer of silver, uniform buckles can be introduced by photo-illumination. Illumination is the 'suitable condition' for the self assembled 'wrinkles' in the thin films where the extent and shape of such a 'wrinkled' structure can be controlled to some extent.

4.2 Background on Buckling phenomenon

In this section, an overview of the relevant background on the film buckling phenomenon is given. The work described in this chapter is the manifestation of controlled stresses in a thin film (refer to Section 4.2.1).

(a) Tensile stress causes a film to contact (b) Compressive stress causes a film to expand

Figure 4.1: Failure modes due to stresses in a thin film

4.2.1 Stresses in a thin film

Excellent adhesion and low stress thin films are typically considered a must in any semiconductor processes. Broadly speaking, stresses can be intrinsic (arising during film growth) or due to external factors like heat (coefficient of thermal expansion mismatch between two materials), humidity, and pressure. While external stresses can be avoided by ensuring proper material compatibility and packaging, intrinsic stresses are more delicate to control or avoid. Intrinsic stresses caused due to structural ordering arising during thin film deposition can be reduced by annealing in many cases. High intrinsic thin film stress can result in adhesion problems and thus compromise long term reliability of the device [121].

Almost all thermally evaporated films are either under compressive or tensile stress. While tensile stress can cause the film to crack, compressive stress causes buckling. Figure 4.1 illustrates the two types of stress induced 'defects' in a thin-film. In some applications of films, compressive stress is desirable. For example in high speed tool bit coatings compressive stresses indicate stronger bonds between material constituents which in turn increases the wear resistance [122].

4.2.2 Buckling phenomenon

Buckling is caused due to the compressive stresses in a thin film along with weak adhesion with the layer underneath. Figure 4.1 shows the effect of stresses in a thin film. These stresses are dependent on the substrate on which the film is coated,

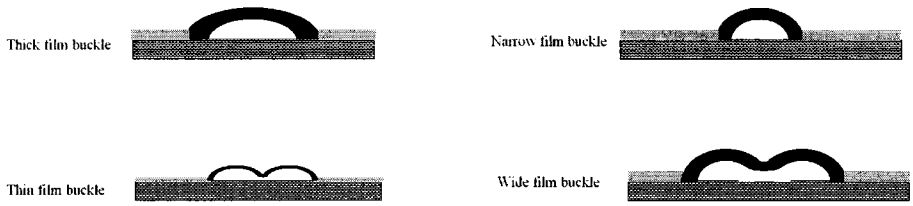

(a) Effect of film thickness on film buckle

(b) Effect of Low adhesion region width on film buckle

Figure 4.2: Effect of film thickness and low adhesion region width on buckle structures

the material itself, the deposition process, temperature variations etc. Buckling is essentially a means for the film to attain the lowest energy configuration and release the accumulated elastic energy.

Buckling in thin films has been studied in detail in [123] and the related references mentioned therein. Depending on the size of the delaminated region and the level of compressive stress, the buckles can be Euler Buckles, telephone cord buckles, or varicose buckles. Figure 4.3(a) shows the different buckle topologies.

Preliminary proof of concept on buckling phenomenon and it's controllability is demonstrated in this work. Another important problem to be solved is to find out a way to consistently create the buckles. This controllability can be achieved by tweaking the thickness of the film and the thickness and width of silver strips patterned underneath the glass. Extreme buckling will lead to fracture of the thin film. Figure 4.2 qualitatively illustrates how the width of the low adhesion region and the thickness of the film affect buckle structures.

Section 4.2.3 describes a potential use of the Euler buckle morphologies as hollow optical waveguides.

4.2.3 Potential use of Buckle structures: Hollow Waveguides

Conventional high index core optical waveguides cannot be used for example, in a biological sample analysis. In such a case, light-matter interaction of light is re-

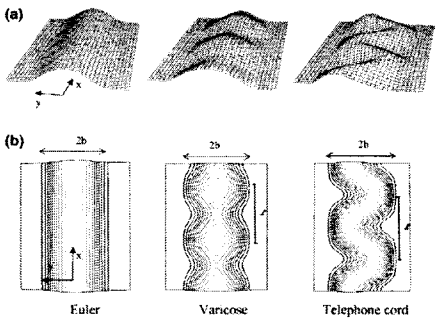

(a) Different types of Buckle modes [123].

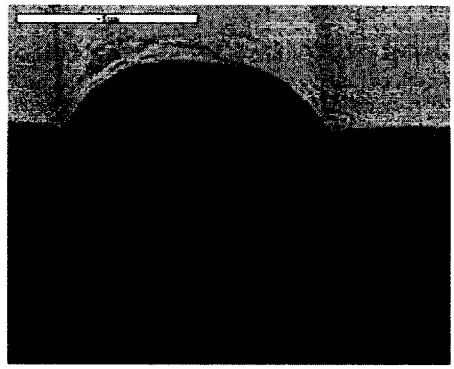

(b) Hollow ARROW waveguide fabricated using sacrificial aluminium core [124].

Figure 4.3: Buckling modes and a potential application of the Euler buckle mode in the literature

quired with the testing media which is normally in liquid or gaseous form. Refractive indices of the tested samples are usually low. For example, aqueous solutions typically have a refractive index of $\sim$1.3-1.35.

Anti-resonant reflecting optical waveguides (ARROW) with a hollow core can be used in such circumstances. ARROW waveguides can be considered as a waveguide made of periodic thin film stacks acting as mirrors for cladding. They are essentially a hollow/low-index media surrounded by a Fabry-Perot reflectors to confine light inside the core. Figure 4.3(b) shows a hollow ARROW waveguide [124].

Hollow waveguides have been realized using wafer bonding[125] and sacrificial core [126] techniques. Reported waveguides of this type are typically 5-10μm in width (refer to Figure 4.3(b)).

The buckling structures we have demonstrated are produced without subjecting the samples to any thermal shocks and is essentially a room temperature process. Due to the natural buckling process to create the hollow core, the inner walls are expected to be much smoother than those made using a sacrificial layer [124].

Figure 4.4 shows an S-bend buckled in an Euler buckle mode and holds promise to form large network of channels on a microfluidic chip.

Figure 4.4: Euler buckles around a s-bend with $L_1 = 250\ \mu m$ (refer to Appendix B)

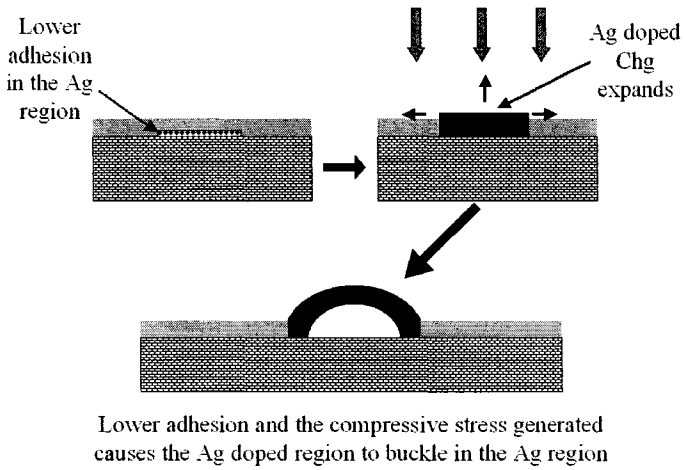

Figure 4.5: Buckling process steps used

4.3 Process Development

The buckling phenomenon described below was initially realized unintentionally during an attempt to fabricate strip waveguides as described in Section 3.2.1.

From the lessons learnt from the silver doping experiments with As_2Se_3 glass in Chapter 3, we decided to test fabrication of silver doped structures by patterning Ag under the glass film (Figure 3.3(b)). Not only would the light used in photodoping have a better penetration into the glass, the lateral diffusion as described in Section 3.2.5.3 might also be reduced. Since only 4 atomic % of silver was intended to be dissolved into the glass, it could be safely assumed that all the deposited silver

would be consumed by the glass. This means that the issue of excess undissolved silver remaining at the interface should not be a huge concern.

A typical fabrication process started with a spin coating 10 μm thick BCB undercladding on top of a silicon wafer. Then, 30 nm of silver film was sputtered followed by patterning strips of widths ranging from 1-10 μm. Different thicknesses of IG2 glass was thermally evaporated and photodoping performed using a white light source (refer to Figure 3.13).

Figure 4.5 illustrates the consequence of the process described above. The following sections describe the experiments in detail.

4.3.1 First Buckling Samples

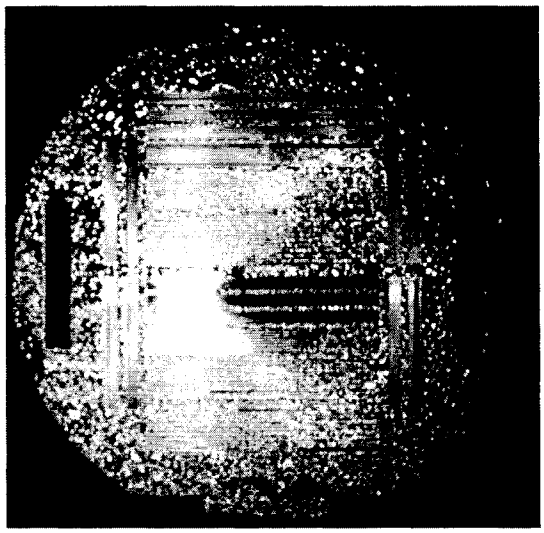

Figure 4.6: Patterned substrate after 1 day

A silver layer of 30 nm thickness was sputtered on a BCB coated silicon wafer. Patterning of Ag was performed using HPR504, a positive resist (illuminated areas are dissolved in developer) and a mask of negative polarity (waveguide is transparent and background is opaque). Developing and etching the silver, using the etchant described in Section 3.2.1.2, produced the reverse of what was intended for Ag strips. For example, Y-splitters on the negative polarity mask will become tapered waveguides when patterning a Ag film using a positive photoresist.

IG2 was then thermally evaporated onto the sample. The expected thickness was 1.2-1.4 μm. The sample was left in ambient light and buckling was observed after a day's delay. Silver dissolution into the glass is accompanied by a volume expansion of the doped region. Such an increase in volume causes a build-up of compressive stresses in the silver doped regions. The reduced adhesion in the patterned regions aids the stress release in the form of buckles.

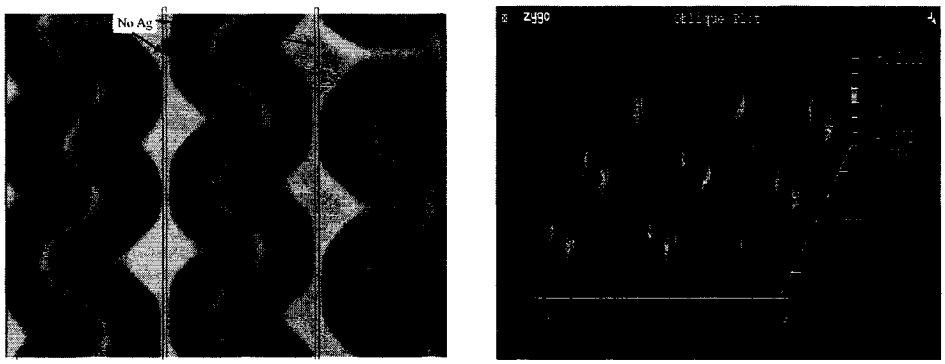

(a) Undulating telephone cord patterns (b) Optical profilometer plot

Figure 4.7: Buckles in First sample. The width of each buckled region is 250 μm

Figure 4.6 shows the full sample where buckling was first observed. Figure 4.7(a) shows the telephone cord buckle modes. Optical profilometer plot can be seen in Figure 4.7(b). The distance between the troughs of the buckles correspond to the waveguide separation in the mask of 250 μm.

Though there are many different ways (modes) in which a film can relieve the stresses we are particularly interested in one of them, namely the Euler mode. The Euler mode is essentially a first order buckle mode among the many other modes in which a film can buckle and can be visualized as analogous to the guided modes in an optical waveguide (refer to Section 2.1.1).

Formation of Euler buckles is very much dependent on the amount of stress developed and the thickness of the chalcogenide film as seen in Section 4.2.2. The tapered structures are a good starting point to learn more about the buckle structures. While the wider areas of silver result in random buckle structures, they evolve Euler buckles as the width tapers downwards. This can be seen in Figure 4.8. Studying tapered sections give many more details regarding the critical width for the formation

of Euler buckles. The taper is more effective in this regard than using a multitude of Ag regions of varying widths for a given thickness of IG2 film.

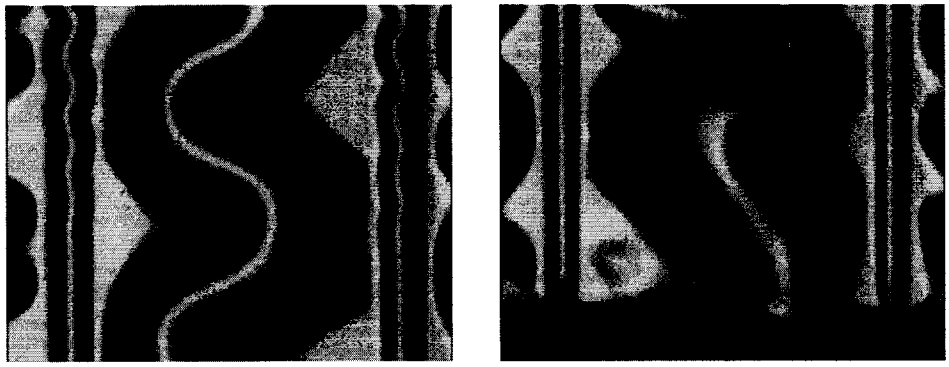

(a) Euler Buckles transforming to Telephone cords

(b) Euler Buckles at the tapered Y-Splitter section.

Figure 4.8: Euler buckles seen in te Y-splitter section of First Sample. The width of the buckled region is 250 μm.

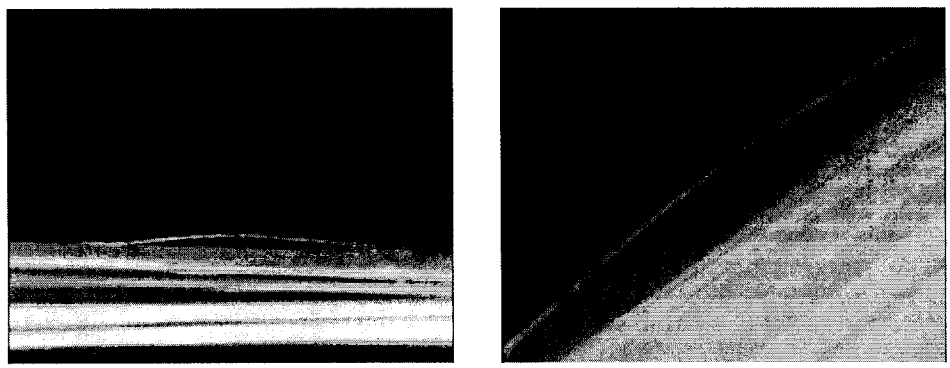

(a) End view of a cracked buckle

(b) End view (rotated) of the cracked buckle

Figure 4.9: End view of the cleaved buckle structures. The BCB layer underneath the buckle is $\sim$ 10 μm thick.

Figure 4.9 shows the cleaved ends of the buckles fabricated. The ability of these buckles to withstand cleaving and handling is still an area that needs work. However, to realize a multilayer ARROW structure similar to the one in Figure 4.3(b), it might be enough to produce compressive stresses in the lower-most layer.

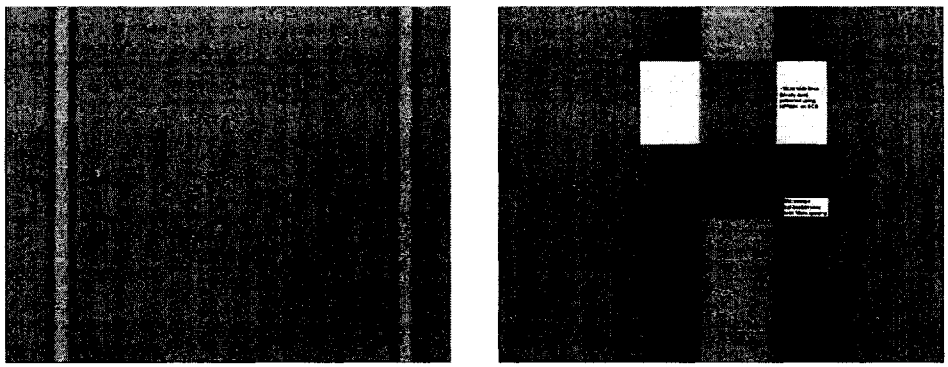

(a) Waveguides after buckle removal

(b) Waveguide after buckle removal. The ruler insert shows a width of 10 μm

Figure 4.10: Waveguides realized after the removal of delaminated buckle regions

4.3.1.1 Waveguides from Buckled films

Buckles in the larger regions completely peeled off automatically. Blowing nitrogen removed most of the remaining heavily buckled parts of the film. In some of the areas, the buckled film delaminated leaving the un-doped waveguide region.
The regions with no Ag were found to adhere excellently to BCB. They withstood cleaning with DI water, acetone agitation and even scrubbing with a cotton swab indicating strong adhesion to the BCB layer underneath. The waveguides thus produced had very rough edges, reflecting the buckle pattern of the adjacent delaminated regions. Contact profilometer measurement of height of the waveguides showed a 1.4 μm thick IG2 layer.

4.3.2 Second buckling samples

Subsequent experiments were devised to repeat the buckling on thinner IG2 film. BCB polymer produced the most consistently good results. This was partly due to the fact that it stood up well to the chemicals used in patterning of the Ag strips. Tests on different polymers are described in the next Section 4.3.3. 4 quarters of BCB coated silicon were patterned using the same mask as shown in the result of Figure 4.6.
200 nm thick IG2 was thermally evaporated onto all 4 samples. Sample 1 was kept in the dark. Sample 2 was left in ambient light. Sample 3 was exposed with white-

light for 1 hour. Sample 4 was first cooled on a thermo-electric cooler for 2 hours. No noticeable buckling was observed in Sample 1.

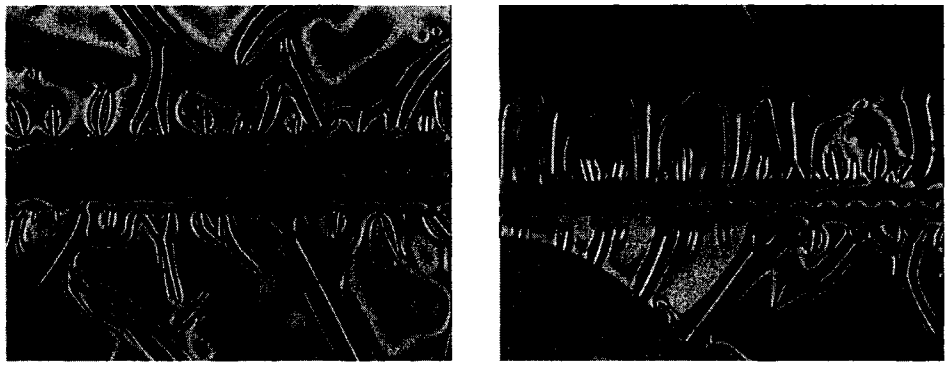

(a) Telephone cord buckles in Sample 2 left in ambient light and coated with SU-8

(b) Telephone cord buckles transforming into Euler buckles in Sample 2 left in ambient light and coated with SU-8

Figure 4.11: Buckles in a 200 nm thick IG2 film coated with SU-8 uppercladding.

Sample 2 buckled in many regions and was spin coated with a top layer of SU-8 polymer. It was found to survive the spinning and curing of SU-8 and is shown in Figure 4.11.

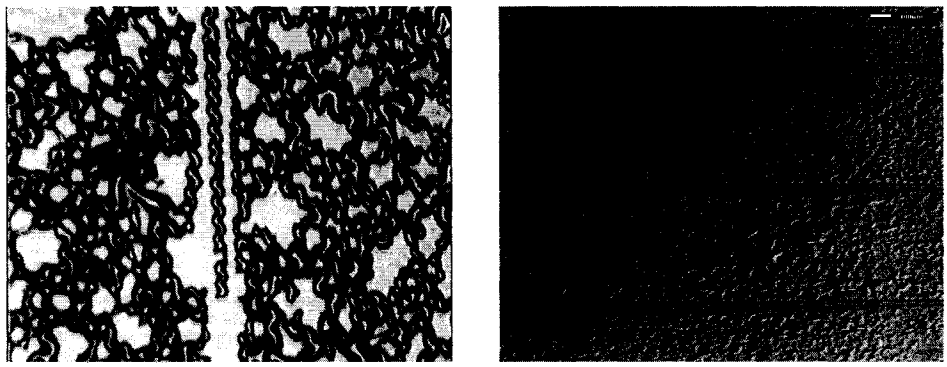

(a) Sample 3: After 1 hr of white-light exposure

(b) Sample 3: Meandering buckle modes

Figure 4.12: Sample 3 buckling

In Sample 3, the buckle formation was observed in real time while doing the white-light exposure. Film buckling started almost immediately on white light exposure indicating that the process is photo-induced.

Sample 4 (refer to Figure 4.13(a)) buckling was very slow and condensation on the

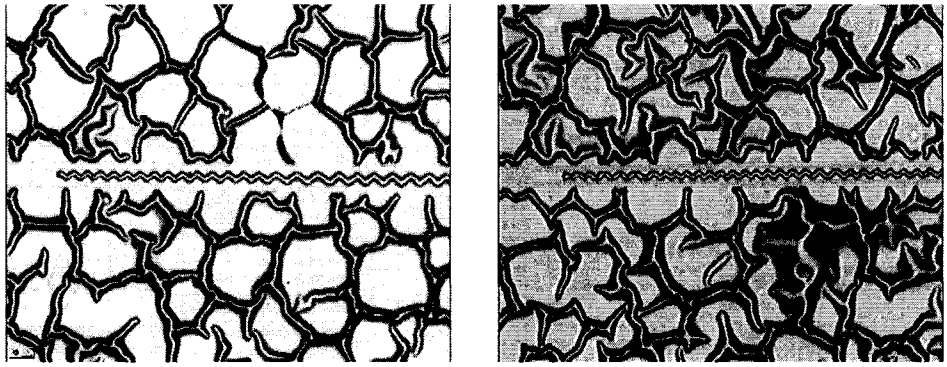

(a) Sample 4: Kept on thermo-electric cooler

(b) Sample 4: Kept on thermo-electric cooler and illuminated with white light

Figure 4.13: Sample 4 buckling

sample was observed due to cooling. Once the buckling was seen to saturate with the thermo-electric cooler, white light was exposure was done while the sample was cooled. Figure 4.13(b) shows an increase in the buckles observed on white light exposure of Sample 4.

4.3.3 Third buckling samples

A third set of experiments was done for two reasons. The first goal was to see how different polymer underlayers affected buckling. The second was to test a buckling after an upper cladding was spun on top of the unbuckled glass. Sample 1 and 2 had BCB and PAI respectively as undercladding while 3 and 4 had SU-8.

About 700 nm of IG2 was thermally evaporated onto the 4 samples (A, B, C, D). Sample A and B did not buckle even after extended exposure. Sample C was coated with SU-8 and buckling was observed during the heat curing SU-8 upper cladding. Subsequent exposure and heat/cool treatment did not produce any more buckling. Most patterned regions on Sample D readily buckled on cleaving. The unbuckled region did not buckle even after 22 hours of white light exposure. Depositing a layer of Tungsten which typically suffers from high compressive stress on top of the unbuckled samples was tried but was not successful [127]. The Tungsten layer showed large scale 'shattering' into fine strands which 'stood up' when near a electrostatically charged surface like lid of a plastic Petri dish, hand etc.

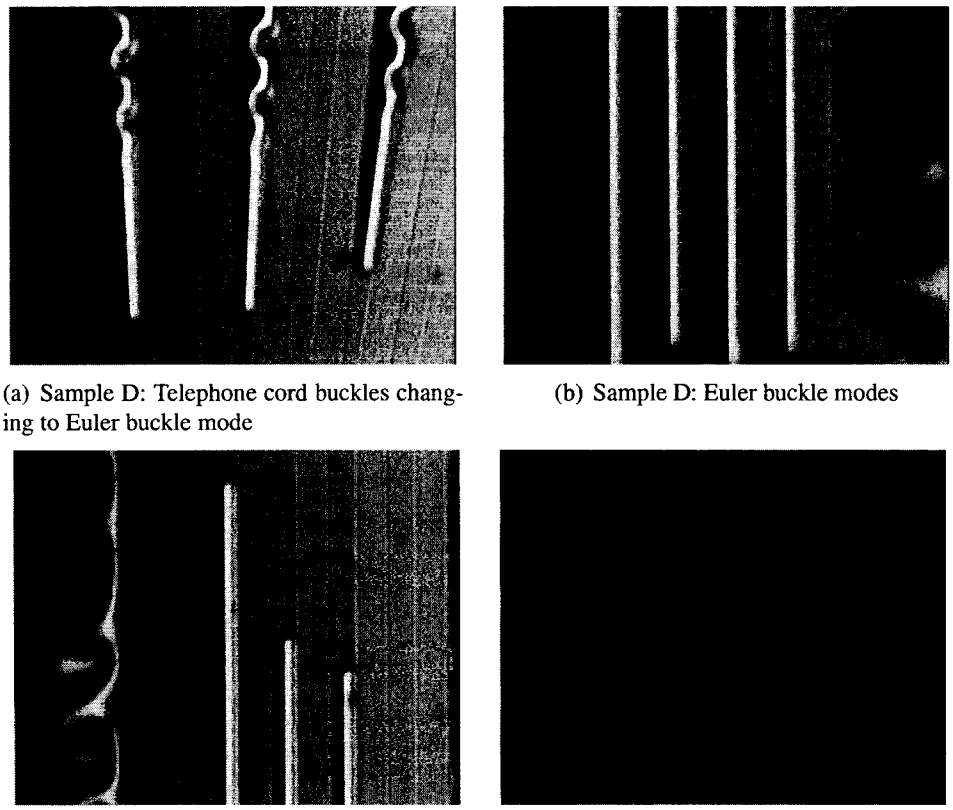

(a) Sample D: Telephone cord buckles changing to Euler buckle mode

(b) Sample D: Euler buckle modes

(c) Sample D: Anomalous termination of the Euler buckles

(d) Sample D: Telephone cord nuckles

Figure 4.14: Sample D buckling structures.

Figure 4.14 shows the Euler buckles observed. The tapering from meandering modes to uniform Euler mode is clearly seen in Figure 4.14(a). Buckles were also seen to be transmitted around a bend in a similar process and is shown in Figure 4.4.

Chapter 5

Polyamide-imide Polymer Based High-index Contrast Waveguides

This chapter describes high index contrast polymer waveguide structures that were studied in parallel with the main work described in Chapter 4. Ring resonator structures that were fabricated are also discussed. A polyamide-imide (PAI) polymer, Torlon AI-10 (sourced from Solvay Advanced Polymers) was studied as a potential core material for integrated optics.

5.1 Background on Polymers

5.1.1 Polymers in Telecommunications

Polymers have been explored as alternative materials for planar lightwave circuits in fiber systems for over 15 years. Some of the key requirements for the use of polymers in long haul fiber optic systems are:

- Extremely low loss (<0.1 dB/cm) at 1550 nm.
- Low birefringence and polarization dependent loss.
- Excellent thermal and environmental stability under standard in-use conditions.
- Low index contrast waveguides with good impedance match to standard fiber.

To date, fluoro-acrylate and silicone polymers probably have achieved the most commercial success [128].

5.1.2 Polymers for Integrated optics

Recently, polymers have been identified as a promising class of materials for photonic interconnects in computing systems (chip-to-chip, and on-chip) [129]. Some requirements on polymers for integrated optics are relaxed and some tightened relative to the polymers for telecom applications:

- Slightly higher loss can be tolerated, and there is more flexibility in choice of operating wavelength.
- Birefringence and polarization dependent losses are less critical since predefined polarization states are feasible.
- Stability at even higher temperatures is important; materials must survive during packaging-related temperature excursions (soldering at $\sim$300°C) and in-use temperatures $>$100°C.
- High index contrast waveguides are needed to enable compact optical circuits and high density optical circuits.

Polymers also offer potential for alternative fabrication techniques such as hot embossing, nano-imprint lithography [130, 131] and soft lithography [132]. Most of the works reported employed relatively low temperature polymers like polystyrene (T_g = 150°C), SU-8 epoxy, polycarbonate, PMMA etc [132].
Aromatic polyimides have the temperature stability for integration with electronics and are widely used in microelectronics [133]. Hence, they are an obvious starting point for integrated optics development in computing systems.
Nevertheless, polyimides suffer from some drawbacks. Polyimides are not traditionally melt- or solution-processable. Typically, thin films of polyimides are made from two or more precursors that are mixed and spun cast on a substrate. This is followed by imidization reaction during thermal curing [133]. Such a procedure limits the processing options for many polyimides. Another problem is that, during imidization the polymer typically undergoes molecular ordering of some sort resulting in very large intrinsic birefringence ($\sim$0.01) and optical scattering loss [133].

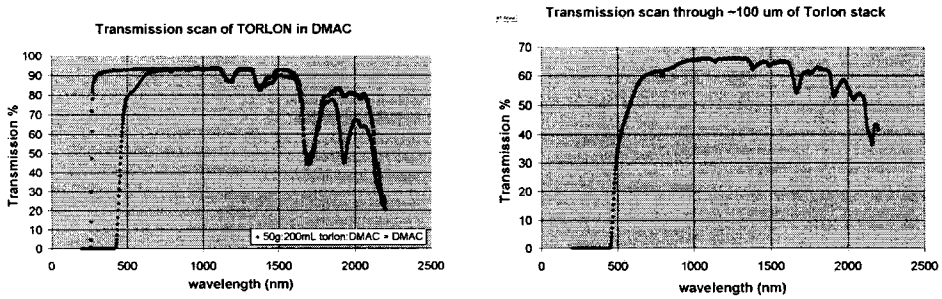

(a) Transmission through quartz cuvet of 1 mm path length filled with pure DMAc and AI-10 dissolved in DMAc

(b) Transmission scan of a stack of 10 films each of 10 μm thickness

Figure 5.1: A qualitative transmission characteristics of PAI polymer in solution and film form showing usable wavelength regions

Hence, much work has been directed at improving the processability of polyimides while maintaining their outstanding thermal stability [129, 133].

5.1.3 Promise of Polyamide-imide

Polyamide-imides or PAIs are high performance thermoplastics. One commercial PAI (Torlon, solvay advanced polymers) is widely used as an industrial material for wire enamels, automotive and aerospace parts, protective coatings on tools, and as a high temperature adhesive [117].

PAI polymers have several outstanding attributes:

- Excellent stability and mechanical properties from cryogenic temperatures up to >260°C. They have been tested in extreme Martian conditions where the mean surface temperatures is ~60°C.
- They are amongst the toughest and strongest of all polymers [117].
- They offer exceptional resistance to most organic solvents and acids. Such outstanding chemical durability allows a wide variety of processing options.
- PAI is solution and melt processable. In our work AI-10 power was dissolved in N,N-dimethyl formamide (DMF) or N,N-dimethylacetamide (DMAc) solvents and spin coated onto a wafer. Curing processes typically consists of

only solvent removal and lengthening of polymer chains unlike the imidization reaction necessary with conventional polyimides.

- They are considered to be true amorphous thermoplastics and shows low birefringence as compared to many polyimides.
- PAI has the the highest glass transition temp amongst thermoplastics (~295°C).
- Among polymers, PAI has one of the highest refractive indices at 1550nm (n~1.65), making it especially suited for research in high-index contrast polymer structures.
- They have excellent dielectric properties and radiation resistance [117].

A qualitative spectral transmission scan (using a Perkin Elmer Lambda 900 spectrophotometer) of pure DMAc and AI-10 polymer dissolved in DMAc were taken to look for absorption lines and determine their transparent wavelength bands. The plot of normalized transmission versus wavelength is shown in Figure 5.1(a). The mixture was then used for spin casting a 10 μm PAI polymer thin film. After curing the film a 100 μm thick PAI bulk sample was formed by stacking ten 10 μm films. The plot of normalized spectral transmission versus wavelength of the bulk sample is shown in Figure 5.1(b). It is clear from Figure 5.1 that PAI has similar low absorption losses at the 980 nm and 1550 nm wavelengths. Thus PAI polymers show promise as an integrated optics polymer for photonic interconnects.

5.2 PAI strip waveguides fabrication

A Si wafer was cleaned in piranha 2:1 sulfuric acid: hydrogen peroxide for 30 minutes, then rinsed in DI water. The adhesion promoter for BCB AP3000 (Dow) was spun on for 30 seconds at 3000 rpm followed by spin casting BCB 3022-63 (Dow) for 30 seconds at 5000 rpm. This produces a BCB film thickness of ~10 μm. BCB film was then hard baked at 160°C in oven under nitrogen for 1 hr.

Thin films of PAI were spun cast on the benzocyclobutene (BCB) undercladding. 25 grams of Torlon (AI-10 from Solvay) was dissolved in 100ml of DMAc for 2

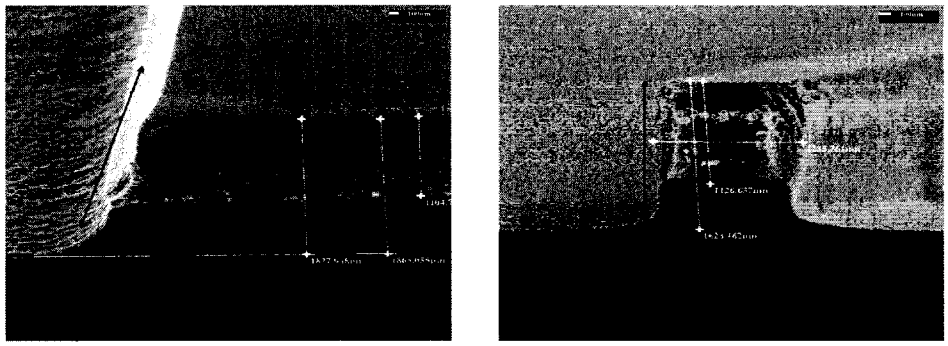

(a) PAI strip waveguides using RIE (b) PAI strip waveguides using ICPRIE

Figure 5.2: Comparison of RIE and ICPRIE sidewall verticality for the same amount of etch. Both Figures have are on the same scale. The scale insert corresponds to 100 nm.

hours and filtered through a 1 micron retention filter paper. The PAI solution was then spin cast on BCB substrate at 2500 rpm to give $\sim$ 1.5 μm thick PAI film. A soft bake for 5 min at 80°C on a hot plate was followed by hard baking in nitrogen atmosphere for 1 hour at 160°C.

Gold was patterned on PAI by a Liftoff process to act as the etch mask. A liftoff process was used since only a negative polarity mask and positive resist was available for UV lithography. Structures fabricated using E-beam lithography are described in Section 5.4.

Once the gold was patterned on top of the PAI layer, conventional Reactive Ion etching (RIE) or ICPRIE were used to etch it. The plasma etch process is described in Section A.5.2. It should be noted that the plasma needed for etching can also cause the back sputtering of the metal used as etch mask. Gold is particularly notorious for this effect but was used because it worked well as an etch mask in our case. Back sputtering is a problem since it interacts with the etch of polymer causing undesirable surface roughness.

After gold removal, BCB uppercladdings were spun on the samples and they were characterized as described in Section 5.3 below. Figure 5.2 shows the sidewall verticality achieved using RIE and ICPRIE. ICPRIE gave much more vertical sidewalls as seen in Figure 5.2(b).

(a) PAI top view 1 (b) PAI end view 1

Figure 5.3: Top and End View of light streak through PAI strip Waveguide

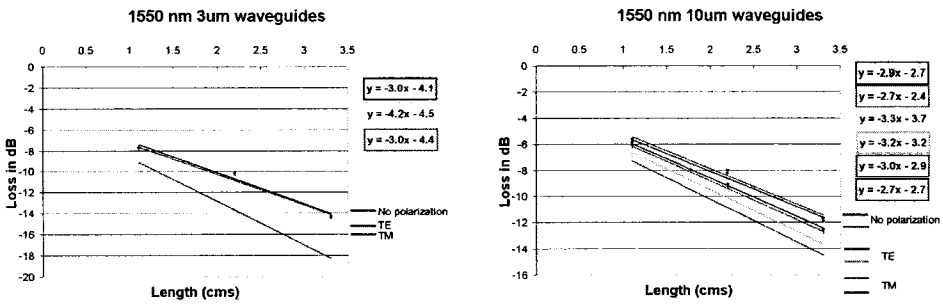

(a) PAI 3um loss 980 (b) PAI 3um loss 1550

Figure 5.4: Comparison of total insertion loss for 3 μm wide waveguide

5.3 Waveguide Loss Measurement

Very good light confinement was observed at 980 nm and 1550 nm wavelengths. The top and end views of 980 nm light coupled into the waveguide are shown in Figure 5.3.

The cut-back method was used for waveguide loss measurement (refer to Section 2.3.1). Total insertion loss was measured for non-polarized input and for TE and TM polarizations. In each of the three cases the input and output power was maximized and measured.

Two waveguides of widths 3 μm and 10 μm were characterized. The starting sample was 3.3 cm long and once the loss measurements were done, it was cleaved into 1.1 cm and 2.2 cm lengths. The cleaving was done in liquid nitrogen, since the Torlon end facet was found to be of better quality under those conditions. The samples were dipped in liquid nitrogen for 30 seconds before cleaving using a diamond

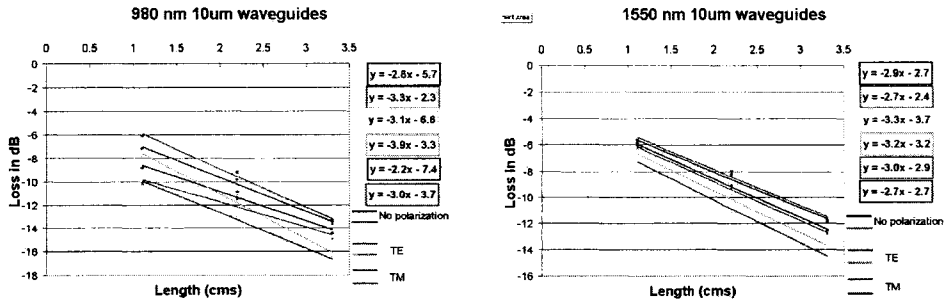

(a) PAI 10um loss 980 (b) PAI 10um loss 1550

Figure 5.5: Comparison of total insertion loss for 10 μm wide waveguide

tipped cleaver. The long (3.3 cm) sample was first characterized followed by the cut samples (1.1 cm and 2.2 cm) to get an estimate of the upper limit of propagation losses in the waveguide.

Figure 5.4 shows the losses measured in a 3 μm wide waveguide at 980 nm and 1550 nm wavelengths. The loss measurements are summarized in Table 5.1.

Table 5.1: PAI loss summary

	1550 nm (dB/cm)		980 nm (dB/cm)	
	TE	TM	TE	TM
3 μm	4.2	3.0	4.8	3.2
10 μm	3.2	2.7	3.1	2.2

The losses at 980nm seem to be considerably higher than 1550nm for TE mode while the discrepancy in losses measured for TM mode is much lower. At each of the wavelengths the TE mode shows higher loss than TM. Figure 5.8 shows typical sidewall roughness observed in PAI strip waveguides.

This makes sense since the TE modes suffer more scattering losses due to sidewall roughness than TM modes due to the way electric field is oriented [134]. Since TE modes are also less confined laterally than the TM modes, the TE fields 'interact' more with the rougher sidewalls than the TM fields (refer Section 2.2.1). This is illustrated in Figures 5.8(b).

Since there is no reason to believe that PAI has higher absorption loss at 980 nm than 1550 nm from the spectral scans (refer to Figure 5.1) it is inferred that the dominant contribution to the propagation loss is sidewall roughness (refer to Section 2.2.1).

The liftoff process for defining the RIE metal etch masks onto the polymer introduce great deal of sidewall roughness as seen in Figure 5.8(a). As expected from the basic scattering theory, shorter wavelength light is more strongly scattered. Characterization of 10 μm wide waveguides also strengthened this proposition. Two 10 μm wide waveguides were used for loss measurements. The results of the loss measurements are shown in Figure 5.5. TE modes also suffered higher losses in these wider waveguides too. The losses at 980 nm were higher than those at 1550 nm. As expected, if sidewall scattering loss makes the dominant contribution then the wider 10 μm waveguides were less lossy than 3 μm wide ones.

5.4 PAI Ring Resonators using E-Beam lithography

Having realized reasonably low-loss strip waveguides in PAI, we attempted to fabricate ring resonators using E-beam lithography.

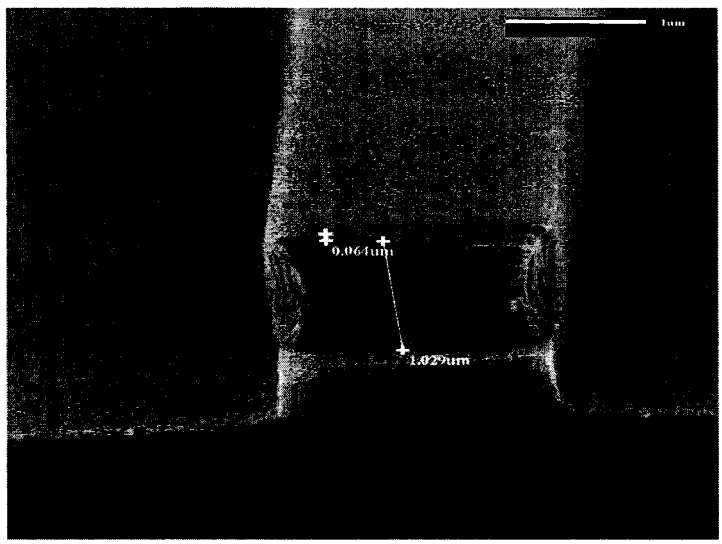

Figure 5.6: PAI strip waveguides fabricated by E-beam lithography

A PAI film was spun cast on BCB undercladding as described in Section 5.2. E-beam HSQ negative resist was spun cast at 4000 rpm for 40s and baked at 180°C for 2 minutes followed by 2 more minutes at 220°C. HSQ forms a glass-like layer on hard baking which served as the etch mask for PAI plasma etch. Polymers, like glasses (refer to Section 3.2.6), are not normally conductive enough to allow one to

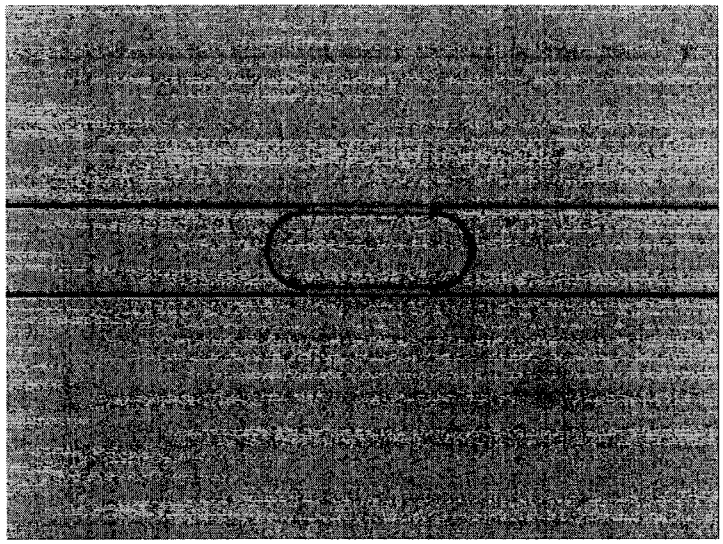

Figure 5.7: Microscope picture of the ring resonator fabricated in PAI by E-beam lithography.

focus the E-beam onto the sample properly. There is a charge build-up hindering accurate co-ordinate setting for exposure. Hence AquaSave, an antistatic layer from Mitsubishi Chemicals, was spun cast at 4000 rpm for 40s and baked at 100°C for 2 mins. E-beam exposure was used to pattern microrings and waveguides on to the sample and the exposed HSQ was developed in tetra methyl ammonium hydroxide (TMAH) for 1min.

After hard-baking on a hotplate for 5 mins at 250°C the sample was etched using ICPRIE (at 20°C) under a pressure of 1.5 mtorr and an ICP power of 150 W with forward power of 20 W. The helium backing was 10 sccm and oxygen gas set to 20 sccm.). Figure 5.6 shows the fabricated waveguides after 16 minutes of ICPRIE. HSQ forms a glass-like layer which could not be removed by any known means that would leave the PAI intact. Therefore HSQ was left on top of the waveguides in the hope that it would not cause extra loss. Stitching errors were also commonly seen while patterning long ($\sim$ 2 cm) samples using Raith 150 SEBL system (refer to Figure 5.7).

The fabricated strip waveguides were coated with BCB uppercladding layer to get an encapsulated strip waveguide structure. Light coupling experiments were performed at 980 nm which did not result in appreciable power output. It was spec-

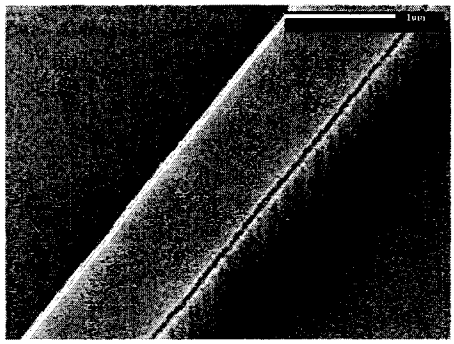

(a) Sidewall roughness in a typical PAI strip waveguide.

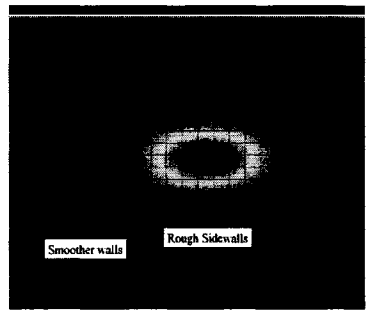

(b) Mode confinement and sidewall roughness problem.

Figure 5.8: Sidewall roughness in PAI strip waveguides

ulated that the unremoved HSQ on top of the waveguides contributed to the large losses observed. Further work needs to be done to confirm this proposition.

Chapter 6

Conclusion and Future Work

The main goal of this work was to realize filters based on microring resonators using silver doped chalcogenide glasses. Although a working microring device was not demonstrated, several fabrication challenges were identified and partially addressed. A unique stress related phenomenon was accidently realized and preliminary studies to control and reproduce the resultant structures is reported. Robust low-loss polymer (polyamide-imide) waveguides were fabricated and characterized.

The following sections describe the key observations made in this work and suggest areas for future work.

6.1 Ag doped Chalcogenide waveguides

Silver doping of As_2Se_3 was investigated to realize fully etched high index contrast strip waveguides. Direct patterning of silver doped waveguides in As_2Se_3 was found to be infeasible. It was observed that the As_2Se_3 and Ag react very rapidly, even at room temperature and in agreement with the findings mentioned in references [112, 86].

A modified lift-off process was proposed and MEA at 50°C was found to produce the best results for selectively etching undoped As_2Se_3. Strip waveguides in As_2Se_3 were fabricated for the first time to our knowledge. Both white light and UV exposure was found to be suitable for photodoping and produced similar results. Furthermore, annealing the As_2Se_3 glass was seen to produce better results than un-

annealed glass. Characterization of Ag doped strip guides showed strong guidance of 980 nm and 1480 nm light. Analysis of scattered light at 1480 nm, using pickup fiber produced an estimate for the propagation loss of $\sim$ 9 dB/cm.

Lateral diffusion of silver during photodoping was found to be a limiting factor in successful dimensional control of the structures fabricated. This agrees with the observation made in reference [99]. Another possible explanation (refer to Figure 3.19) for this widening, is also suggested. It is believed that the slanted sidewalls of the photoresist and the thin silver layer might not be sufficient to block all the light from reaching the Ag doped-undoped chalcogenide interface resulting in lateral diffusion in the upper surface of the glass. Attempts to predict and pre-compensate for lateral diffusion were not successful.

E-beam lithography was used to fabricate microring resonator filters in As_2Se_3. E-beam focussing problem due to charge accumulation on non-conductive substrates were observed. This was successfully resolved by using a commercially available water soluble anti-static layer (Aquasave).

Preliminary results indicate that MEA etchant was also suitable for selectively etching Ag doped IG2 and IG5 glasses.

Investigating the cause and control of lateral diffusion needs further study. Numerous spots were observed (refer to Section 3.2.3.2) on top of fabricated waveguides, and this problem also requires further study.

6.2 Buckling

Patterning of the silver layer underneath the $Ge_{33}As_{12}Se_{55}$ glass, originally intended to allow light to penetrate the Ag-ChG interface for better Ag dissolution, resulted in the discovery of buckled delamination structures. These buckle structures were explored with the goal of assessing their potential in making hollow waveguides. The dependence of morphology of such buckles on film thickness and width of the Ag regions was observed.

Conventional strip waveguides were also fabricated by mechanically removing the buckled regions (refer to Section 4.3.1.1). However, only short lengths of such strip

waveguides were fabricated.

Further experiments were devised with the intent of realizing microchannels from the Euler buckle modes observed. The controllability and reproducibility of these structures was attempted before and after a single upper polymer (SU-8) layer was spun cast, as described in Sections 4.3.2 and 4.3.3. Euler buckles were found to withstand the process of spin coating an upper cladding (refer to Figure 4.11).

The control of buckle morphology is not fully understood at this point and is a subject for future work.

6.3 Polymer Integrated Optics

Polyamide-imide strip waveguides encapsulated in benzocyclobutene claddings were fabricated and characterized. Cut-back loss measurements indicated higher loss at 980 nm than at 1550 nm. Also, TE modes exhibited higher losses than TM indicating that the sidewall roughness induced scattering losses were dominant (refer to Table 5.1).

E-beam lithography was used to realize strip waveguides. HSQ, a negative e-beam resist, was used as etch mask. The HSQ etch mask was not removable without damaging the PAI layer and hence it was left on top of the waveguides. The waveguides fabricated were very lossy and it is speculated that the unremoved HSQ contributed to losses.

Further work is required to address the issue of sidewall roughness due to photolithography and RIE processes. For good quality waveguides by E-beam lithography, alternative E-beam etch masks need to be studied.

Bibliography

[1] Gabriel Torres and Cassio Lima. Introduction to optical fibers. *[Online]: http://www.hardwaresecrets.com/article/154*, June 2005.

[2] RBN. Characteristics of CWDM: Roots, current status and future opportunities. *[Online]: www.rbni.com*, September 2002.

[3] Brent E. Little. Advances in microring resonators: Little Optics Inc. *Integrated Photonics Research Conference*, 2003.

[4] Tymon Barwicz and Henry I. Smith. Evolution of line edge roughness during fabrication of high-index contrast microphotonic devices. *Journal of Vacuum Science and Technology B*, 21(6):2892–2896, November/December 2003.

[5] Spin Theory. Spin coating process theory. *[Online]: http://www.cise.columbia.edu/clean/process/spintheory.pdf.*

[6] Peter Van Zant. *Microchip Fabrication.* McGraw-Hill Professional, 2004.

[7] International Telecommunication Union. *ITU-T G.692*, October 1998.

[8] Dominik G. Rabus. *Realization of Optical Filters using Ring Resonators with integrated semiconductor optical amplifiers in GaInAsP/InP.* PhD thesis, Technical University of Berlin, 2002.

[9] Bin Liu, Ali Shakouri, and John E. Bowers. Passive microring-resonator-coupled lasers. *Applied Physics Letters*, 79(22):3561–3563, November 2001.

[10] R.W. Boyd and J.E. Heebner. Sensitive disk resonator photonic biosensor. *Applied Optics*, 40(31):5742–5747, November 2001.

[11] Shanhui Fan Pierre R. Villeneuve H. A. Haus C. Manolatou, Steven G. Johnson and J. D. Joannopoulos. High-density integrated optics. *IEEE Journal of Lightwave Technology*, 17(9):1682–1692, 1999.

[12] L.C. Kimerling. Silicon microphotonics. *Applied Surface Sciience*, 159-160:8–13, 2000.

[13] G.-L. Bona, R. Germann, and B. J. Offrein. SiON high-refractive-index waveguide and planar lightwave circuits. *IBM Journal of Research and Development*, 47(2/3):239–249, 2003.

[14] U. Hilleringmann and K. Goser. Optoelectronic system integration on silicon: waveguides, photodetectors, and VLSI CMOS circuits on one chip. *IEEE Transactions on Electron Devices*, 42(5):841–846, 1995.

[15] A. V. Mule, E. N. Glytsis, T. K. Gaylord, and J. D. Meindl. Electrical and optical clock distribution networks for gigascale microprocessors. *IEEE Transactions on VLSI Systems*, 10(5):582–594, 2002.

[16] G.T. Reed. The optical age of silicon. *Nature*, 427:595–596, 2004.

[17] Jacob Scheuer, William M. J. Green, Guy DeRose, and Amnon Yariv. Low threshold two-dimensional annular bragg lasers. *Optics Letters*, 29:2641, 2004.

[18] T.F.Krauss. Photonic crystals for integrated optics. In *Proceedings Summer School on Nanoscale Linear and Non-linear Optics, Erice, Italy*, 2000.

[19] L. C. Kimerling. Photons to rescue: microelectronics becomes microphotonics. *The Electrochemical Society Interface*, 9(2):28, 2000.

[20] A. Scherer, O. Painter, J. Vuckovic, M. Loncar, and T. Yoshie. Photonic crystals for confining, guiding, and emitting light. *IEEE Transactions on Nanotechnology*, 1(1):4–11, March 2002.

[21] T. Yoshie, O. B. Shchekin, H. Chen, D.G. Deppe, and A. Scherer. Quantum dot photonic crystal lasers. *IEE Electronics Letters*, 38(17):967–968, August 2002.

[22] H. Kosaka, T. Kawashima, A. Tomita, M. Notomi, T. Tamamura, T. Sato, and S. Kawakami. Superprism phenomena in photonic crystals: toward microscale lightwave circuits. *IEEE Journal of Lightwave Technology*, 17(11):2032–2038, November 1999.

[23] J. F. Lotspeich. Explicit general eigenvalue solutions for dielectric slab waveguides. *Applied optics*, 14(2):327–335, February 1975.

[24] V. Ramaswamy. Strip loaded film waveguide. *Bell Sytems Technical Journal*, 53:697–704, 1974.

[25] R. M. Knox and P. P. Toulios. Integrated circuits for the millimeter through optical frequency range. In *Proc MRI symp submillimetre waves Fox J., Ed Brooklyn, NY: polytechnic press*, pages 497–516, Nov 1970.

[26] H. Kogelnik. *Theory of Optical Waveguides, in guided-wave optoelectronics*. Springer Verlag, 1990.

[27] R. Hauffe, U. Siebel, K. Petermann, R. Moosburger, J. R. Kropp, and F. Arndt. Methods for passive fiber chip coupling of integrated optical devices. *IEEE Transactions on Advanced Packaging*, 24(4):450–455, November 2001.

[28] Vilson R. Almeida, Roberto R. Panepucci, and Michal Lipson. Nanotaper for compact mode conversion. *Optics Letters*, 28(15):1302–1304, August 2003.

[29] P. K. Tien. Light waves in thin films and integrated optics. *Applied optics*, 10:2395–2419, 1971.

[30] Yurii A. Vlasov and Sharee J. McNab. Losses in single-mode silicon-on-insulator strip waveguides and bends. *Optics Express*, 12(8):1622–1631, April 2004.

[31] Kevin K. Lee, Desmond R. Lim, Lionel C. Kimerling, Jangho Shin, and Franco Cerrina. Fabrication of ultralow-loss Si/SiO_2 waveguides by roughness reduction. *Optics Letters*, 26(23):18881890, December 2001.

[32] Chung-Yen Chao and L. Jay Guo. Reduction of surface scattering loss in polymer microrings using thermal-reflow technique. *IEEE Photonics Technology Letters*, 16(6):1498–1500, June 2004.

[33] Robert G. Hunsperger. *Integrated Optics Theory and Technology*. Springer Verlag, 2002.

[34] E. A. J. Marcatili and S. E. Miller. Improved relations describing directional control in electromagnetic wave guidance. *Bell System Technical Journal*, 48:2161, 1969.

[35] E. A. J. Marcatili. Bends in optical dielectric waveguides. *Bell System Technical Journal*, 50(8):2103–2132, September 1969.

[36] Dietrich Marcuse. *Light Transmission Optics*. Van Nostrand Reinhold, New York, 1972.

[37] Vijaya Subramaniam, Gregory N. De Brabander, David H. Naghski, and Joseph T. Boyd. Measurement of mode field profiles and bending and transition losses in curved optical channel waveguides. *IEEE Journal of Lightwave Technology*, 15(6):990–997, June 1997.

[38] S. Iraj Najafi. *Introduction to Glass Integrated Optics*. Artech House, 1992.

[39] R. G. Walker. Simple and accurate loss measurement technique for semiconductor optical waveguides. *Electron Letters*, 21(13):581–583, June 1984.

[40] Y. Okamura, A. Miki, and S. Yamamoto. Observation of wave propagation in integrated optical circuits. *Applied optics*, 25(19):405–3408, October 1986.

[41] M. Moller, L. M. Hoffer, G. L. Lippi, T. Ackemann, A. Gahl, and W. Lange. Fabry-Perot and ring cavity configurations and transverse optical patterns. *Journal of Modern Optics*, 45(9):1913 – 1926, September 1998.

[42] K.R. Hiremath. Modeling of 2D cylindrical integrated optical microresonators. Technical report, University of Twente, June 2003.

[43] Katsunari Okamoto. *Fundamentals of Optical Waveguides*. Academic Press, 2000.

[44] J. M. Choi, R. K. Lee, , and Amnon Yariv. Control of critical coupling in a ring resonator fiber configuration: Application to wavelength selective switching, modulation, amplification and oscillation. *Optics Letters*, 26(16):405–408, August 2001.

[45] A. Yariv. Critical coupling and its control in optical waveguide-ring resonator systems. *IEEE Photonics Technology Letters*, 14(4):483–485, April 2002.

[46] S. T. Chu, W. Pan, S. Sato, T. Kaneko, B. E. Little, and Y. Kokubun. Wavelength trimming of a microring resonator filter by means of a UV sensitive polymer overlay. *IEEE Photonics Technology Letters*, 11:688–690, 1999.

[47] E. A. J. Marcatili. Dielectric rectangular waveguide and directional coupler for integrated optics. *The Bell Technical Journal*, 38:2071–2102, 1969.

[48] V. Van, T. A. Ibrahim, P. P. Absil, F. G. Johnson, R. Grover, and P. T. Ho. Optical signal processing using nonlinear semiconductor microring resonators. *IEEE Journal of Selected Topics in Quantum Electronics*, 8:705–713, June 2002.

[49] B. E. Little et al. Vertically coupled optical resonator devices over a cross-grid waveguide architecture. *United States Patent Number 6,411,752*, June 2002.

[50] L. B. Soldano and E. C. M. Pennings. Optical multi-mode interference devices based on self-imaging: Principles and applications. *IEEE Journal of Lightwave Technology*, 13:615–627, April 1995.

[51] A. Ray Hilton. Nonoxide chalcogenide glasses as infrared optical materials. *Applied optics*, 5(12):1–12, December 1966.

[52] A. Zakery and S. R. Elliot. Optical properties and applications of chalcogenide glasses: A review. *Journal of Non-Crystalline Solids*, 330:1–12, 2003.

[53] M. Frumar and T. Wagner. Ag doped chalcogenide glasses and their applications. *Current Opinion in Solid State and Materials Science*, 7:117126, 2003.

[54] V. Balan, C. Vigreux, A. Pradel, A. Llobera, C. Dominguez, M. I. Alonso, and M. Garriga. Chalcogenide glass-based rib ARROW waveguide. *Journal of Non-Crystalline Solids*, 326-327:455–459, 2003.

[55] X. H. Zhang, Y. Guimond, and Y. Bellec. Production of complex chalcogenide glass optics by molding for thermal imaging. *Journal of Non-Crystalline Solids*, 326327:519523, 2003.

[56] J.-F. Viens, C. Meneghini, A. Villeneuve, T. V. Galstian, E. J. Knystautas, M. A. Duguay, K. A. Richardson, and T. Cardinal. Fabrication and characterization of integrated optical waveguides in sulfide chalcogenide glasses. *IEEE Journal of Lightwave Technology*, 17(7):11841191, Jul 1999.

[57] V. Lyubin, M. Klebanov, A. Feigel, and B. Sfez. Films of chalcogenide glassy semiconductors: New phenomena and new applications. *Thin Solid Films*, 459:183186, 2004.

[58] D. J. Gibson and J. A. Harrington. Extrusion of hollow waveguide performs with a one-dimensional photonic bandgap structure. *Journal of Applied Physics*, 95(8):3895–3900, 2004.

[59] K. Kuriki, O. Shapira, S. D. Hart, G. Benoit, Y. Kuriki, J. F. Viens, M. Bayindir, J. D. Joannopoulos, and Y. Fink. Hollow multilayer photonic bandap fibers for NIR applications. *Optics Express*, 12(8):15101517, 2004.

[60] P. A. Thielen J. S. Sanghera L. B. Shaw, B. Cole and I. D. Aggarwal. Mid-wave IR and long-wave IR laser potential of rare-earth doped chalcogenide glass fiber. *IEEE Journal of Quantum Electronics*, 48(9):11271137, September 2001.

[61] H Tawarayama, E. Ishikawa, K. yamanaka, Y. matsouka, and H toratani. Optical properties and applications of chalcogenide glasses: a review. In *Proceedings of osa optical ampliciers their application*, 1997.

[62] A. K. Mairaj, A. M. Chardon, D. P. Shepherd, and D.W. Hewak. Laser performance and spectroscopic analysis of optically written channel waveguides in neodymium-doped gallium lanthanum sulphide glass. *IEEE Journal of Selexted Topics in Quantum Electronics*, 8(6):13811388, November/December 2002.

[63] S. Spalter, H. Y. Hwang, J. Zimmerman, G. Lenz, T. Katsufuji, S.-W. Cheong, and R. E. Slusher. Strong self-phase modulation in planar chalcogenide glass waveguides. *Optics Letters*, 27(5):363365, 2002.

[64] N. Ho, J. M. Laniel, R. Vallee, and A. Villeneuve. Photosensitivity of As-S chalcogenide thin films at 1.5 μm. *Optics Letters*, 28(12):965–967, 2003.

[65] Ray G. DeCorby, Nakeeran Ponnampalam, Mahesh M. Pai, Hue T. Nguyen, Prabhat K. Dwivedi, Thomas J. Clement, Chris J. Haugen, Jim N. McMullin, and Safa O. Kasap. High index contrast waveguides in chalcogenide glass and polymer. *IEEE Journal of Selected Topics in Quantum Electronics*, 11(2):539, March/April 2005.

[66] C. W. Slinger, A. Zakery, P. J. S. Ewen, and A. E. Owen. Photodoped chalcogenides as potential infrared holographic media. *Applied Optics*, 31(14):2490–2498, May 1992.

[67] T. Wagner and P. J. S. Ewen. Photo-induced dissolution effect in $Ag/As_{33}S_{67}$ multilayer structures and its potential application. *Journal of Non-Crystalline Solids*, 266-269:979–984, 2000.

[68] T. Wagner, G. Dale, P. J. S. Ewen, A. E. Owen, and V. Perina. Kinetics of the thermally and photoinduced solid state reaction of Ag with $As_{33}S_{67}$ films. *Journal of Applied Physics*, 87(11):7758–7767, 2000.

[69] M. Naito, M. Ishimaru, and Y. Hirotsu. Local structure analysis of GeSbTe phase change materials using high-resolution electron microscopy and nanobeam diffraction. *Journal of Applied Physics*, 95(12):81308135, 2004.

[70] J. D. Maimon, K. K. Hunt, L. Burcin, and J. Rodgers. Chalcogenide memory arrays: Characterization and radiation effects. *IEEE Transactions on Nuclear Science*, 50(6):18781884, December 2003.

[71] S. R. Ovshinsky and H. Fritzsche. Electronic conduction in amorphous semiconductors and the physics of the switching and memory phenomena. *Journal of Non-Crystalline Solids*, 2:393, 1970.

[72] Arun Madan and Melvin P. Shaw. *The physics and application of Amorphous semiconductors*. Academic Press Inc.(London) Ltd, 1988.

[73] Y. Ohmachi. Acousto-optical light diffraction in thin films. *Journal of Applied Physics*, 44(9):39283933, 1973.

[74] T. Suhara and H. Nishihara. Integrated optics components and devices using periodic structures. *IEEE Journal of Quantum Electronics*, QE-22(6):845–867, June 1986.

[75] C. B. Pedroso, E. Munin, A. B. Villaverde, J. A. Medeiros Neto, N. Aranha, and L. C. Barbosa. High Veredt constant Ga:S:La:O chalcogenide glasses for magneto-optical devices. *Optical Engineering*, 38(2):214219, 1999.

[76] D. S. Gill, R.W. Eason, C. Zaldo, H. N. Rutt, and N. A. Vainos. Characterization of GaLaS chalcogenide glass thin-film optical waveguides, fabricated by pulsed laser deposition. *Journal of Non-Crystalline Solids*, 191:321–326, 1995.

[77] C. C. Huang, D. W. Hewak, and J. V. Badding. Deposition and characterization of germanium sulphide glass planar waveguides. *Optics Express*, 12(11):25012506, 2004.

[78] K. Petkov and P. J. S. Ewen. Photo-induced changes in linear and nonlinear optical properties of chalcogenide glasses. *Journal of Non-Crystalline Solids*, 249:150–159, 1999.

[79] S. Ramachandran and S. G. Bishop. Low loss photoinduced waveguides in rapid thermally annealed films of chalcogenide glasses. *Applied Physics Letters*, 74(1):13–15, 1999.

[80] R. K.Watts, M. deWit, and W. C. Holton. Nonoxide chalcogenide glass films for integrated optics. *Applied optics*, 13(10):23292332, 1974.

[81] A. Zakery, Y. Ruan, A.V. Rode, M. Samoc, and B. Luther-Davies. Lowloss waveguides in ultrafast laser-deposited As-S chalcogenide films. *Journal of the Optical Society of America B*, 20(9):18441852, 2003.

[82] N. Ponnampalam, R. G. DeCorby, H. T. Nguyen, P. K. Dwivedi, C. J. Haugen, J. N. McMullin, and S. O. Kasap. Small core rib waveguides with embedded gratings in As_2Se_3 glass. *Optics Express*, 12(25):6270–6277, 2004.

[83] S. Zembutsu and S. Fukunishi. Waveguiding properties of (Se,S)- based chalcogenide glass films and some applications to optical waveguide devices. *Applied optics*, 18(3):393399, 1979.

[84] A. R. Hilton and D. J. Hayes. The interdependence of physical parameters for infrared transmitting glasses. *Journal of Non-Crystalline Solids*, 17:339348, 1975.

[85] R. E. Slusher, G. Lenz, J. Hodelin, J. Sanghera, L. B. Shaw, and I. D. Aggarwal. Large Raman gain and nonlinear phase shifts in high-purity As-Se chalcogenide fibers. *Journal of the Optical Society of America B*, 21(6):11461155, 2004.

[86] R. M. Bryce, H. T. Nguyen, P. Nakeeran, T. Clement, C. J. Haugen, R. R. Tykwinski, R. G. DeCorby, and J. N. McMullin. Polyamide-imide polymer thin films for integrated optics. *Thin Solid Films*, 458:233–236, 2004.

[87] A.V. Kolobov and S. R. Elliott. Photodoping of amorphous chalcogenides by metals. *Advance in Physics*, 40:625–684, 1991.

[88] T. Wagner and M. Frumar. Photoenhanced dissolution and diffusion of Ag in AsS layers. *Journal of Non-Crystalline Solids*, 116(2-3):269–276, February 1990.

[89] K. Ogusu, S. Maeda, M. Kitao, H. Li, and M. Minakata. Optical and structural properties of Ag(Cu)-As_2Se_3 chalcogenide films prepared by photodoping. *Journal of Non-Crystalline Solids*, 347:159–165, 2004.

[90] A. Wagner, D. Barr, T. Venkatesan, W. S. Crane, V. E. Lamberti, K. L. Tai, and R. G. Vadimsky. Germanium selenide: A resist for low-energy ion beam lithography. *Journal of Vacuum Science and Technology*, 19:1363–1367, 1981.

[91] Y.-C. Liang, H. Yamanaka, and K. Tada. Exposure characteristics of electron-beam induced silver doping and its application to grating device fabrication in chalcogenide glass. *Thin Solid Films*, 165:55–65, 1988.

[92] J. Fick, B. Nicholas, C. Rivero, K. Elshot, R. Irwin, K.A. Richardson, M. Fischer, and R. Vallee. Thermally activated silver diffusion in chalcogenide thin films. *Thin Solid Films*, 418:215–221, 2002.

[93] D.S. Gill, R. W. Easonm C. Zaldo, H. N. Rutt, and N. A. Vainos. Ag doped chalcogenide glasses and their applications. *Journal of Non-Crystalline Solids*, 81:71, February 1995.

[94] S. R. Elliot. Ag doped chalcogenide glasses and their applications. *Journal of Non-Crystalline Solids*, 81:71, 1986.

[95] T. I. Kosa, T. Wagner, P. J. S. Ewen, and A. E. Owen. Index of refraction of Ag-doped $As_{37}S_{67}$ films: measurement and analysis of dispersion. *Philosophical Magazine B*, 71:311–318, 1995.

[96] K. Ogusu, J. Yamasaki, S. Maeda, M. Kitao, and M. Minakata. Linear and nonlinear optical properties of Ag-As-Se chalcogenide glasses for all-optical switching. *Optics Letters*, 29(3):265–267, February 2004.

[97] Manabu Kawasaki, Junichi Kawamura, Yoshio Nakamura, and Masaru Aniya. Ionic conductivity of $Ag_x(GeSe_3)_{1-x}$ ($0 < x < 0.571$) glasses. *Solid State Ionics*, 123(1-4):259–269, July 1999.

[98] A. V. Kolobov, V. Lyubin, T. Yasuda, M. Klebanov, and K. Tanaka. Photoinduced anisotropy in vitreous As_2S_3: A reflectance difference study. *Physical review B*, 55:8788–8792, 1997.

[99] R. Dror, A. Feigel, M. Veinguer, B. Sfez, M. Klebanov, A.Arsh, and V. Lyubin. Sub-micron sculpturing on chalcogenide films. In *Proceedings of SPIE Vol. 5720 - Micromachining Technology for Micro-Optics and Nano-Optics III*, 1997.

[100] Masaaki Yamaguchi, Isamu Shimizu, and Eiichi Inoue. Diffusion of silver associated with photodoping into amorphous chalcogenides. *Journal of Non-Crystalline Solids*, 47(3):341–354, February 1982.

[101] A. Yoshikawa, O. Ochi, H. Nagai, and Y. Mizushima. A novel inorganic photoresist utilizing Ag photodoping in Se-Ge glass films. *Applied Physics Letters*, 29:677, 1976.

[102] Hyun-Yong Lee and Takafumi Yao. Wet-etching selectivity of Ag-photodoped asgeses thin films and the fabrication of a planar corrugated one-dimensional photonic crystal by a holographic method. *Journal of Non-Crystalline Solids*, 20(5):2017–2023, September/October 2002.

[103] Keijiro Suzuki, Kazuhiko Ogusu, and Makoto Minakata. Single-mode Ag-As_2Se_3 strip-loaded waveguides for applications to all-optical devices. *Optics Express*, 13(21):8634–8641, 2005.

[104] K. Ogusu, Y. Hosokawa, S. Maeda, M. Minakata, and H. Li. Photo-oxidation of As_2Se_3, Ag-As_2Se_3, and Cu-As_2Se_3 chalcogenide films. *Journal of Non-Crystalline Solids*, 351:3132–3138, 2005.

[105] Albert Polman and Frank C. J. M. van Veggel. Broadband sensitizers for erbium-doped planar optical amplifiers: review. *Journal of the Optical Society of America B*, 21(5):871–892, May 2004.

[106] The Dow Chemical Company. *CYCLOTENE 3000 Series Advanced Electronic Resins*. 2005.

[107] Tamaki Yaji, Shoichi Kurita, Yasuhiro Tejima, Ayahito Horinouchi, and Masaru Koyanagi. Integrated optical devices using amorphous As_2S_3 thin film. *IEEE Transactions on components, hybrids, and manufacturing technology*, (1):134–135, March 1983.

[108] J. Teteris. Amorphous AsSSe semiconductor resists for holography and lithography. *Journal of Non-Crystalline Solids*, 299-302:978982, 2002.

[109] K. E. Youden, T. Grevatt, R. W. Eason, H. N. Rutt, R. S. Deal, and G. Wylangowski. Pulsed laser deposition of Ga-La-S chalcogenide glass thin film optical waveguides. *Applied Physics letters*, 63(12):1601–1603, September 1993.

[110] S. A. Zenkin, S. B. Mamedov, M. D. Mikhailov, E. Yu. Turkina, and I. Yu. Yusupov. Mechanism for interaction of amine solutions with monolithic glasses and amorphous films in As-S system. *Glass physics and chemistry*, 23(5):393–399, 1997.

[111] S. Mamedov. On the macromolecular mechanism of dissolution of As_2S_3 films in organic solutions. *Thin Solid Films*, 226:215–218, 1993.

[112] M. V. Sopinskyy, P. F. Romanenko, I. Z. Indutnyy, and E. F. Venger. Formation of profiled holographic diffraction gratings using physicochemical interaction in As_2Se_3-Ag system. *Journal of Optoelectronics and Advanced Materials*, 3(2):383–388, June 2001.

[113] Huai-Yu Cheng, Chao-An Jong, Chain-Ming Lee, and Tsung-Shune Chin. Wet-etching characteristics of $Ge_2Sb_2Te_5$ thin films for phase-change memory. *IEEE Transactions on Magnetics*, 41(2):1031–1033, February 2005.

[114] F Hamed, S Gygax, and A E Curzon. Pressure contacts to Bi2212 whiskers. *Superconductor Science and Technology*, 10:857–861, 1997.

[115] T. Wagner, A. Mackova, V. Peina, E. Rauhala, A. Seppla, S. O. Kasap, M. Frumar, Mir. Vlek, and Mil. Vlek. The study of photo- and thermally-induced diffusion and dissolution of Ag in $As_{30}S_{70}$ amorphous films and its reaction products. *Journal of Non-Crystalline Solids*, 299-302(2):1028–1032, April 2002.

[116] P. Nakeeran R. G. DeCorby P. K. Dwivedi C. J. Haugen J. N. McMullin S. O. Kasap R. M. Bryce, H. T. Nguyen. Direct UV patterning of waveguide devices in As_2Se_3 thin films. *Journal of Vacuum Science and Technology A*, 22(3):1044–1047, 2004.

[117] Solvay Advanced Polymers. Torlon polyamide-imide design guide. *[Online]: http://www.solvayadvancedpolymers.com/static/wma/pdf/9/9/7/TDG 2003.pdf.*

[118] T. Wagner, V. Perina, M. Vlcek, M. Frumar, E. Rauhala, J. Saarilahti, and P.J.S. Ewen. Rutherford backscattering and kinetics study of the photo-induced solid state chemical reaction between silver and amorphous $As_{33}S_{67}$ layers. *Journal of Non-Crystalline Solids*, 212(2-3):157–165, June 1997.

[119] Tymon Barwicz, Milo A. Popovic, Peter T. Rakich, Michael R. Watts, Hermann A. Haus, Erich P. Ippen, and Henry I. Smith. Microring-resonator-based add-drop filters in SiN: fabrication and analysis. *Optics Express*, 12(7):1437–1442, April 2004.

[120] Qingbin Zheng. *Fabrication and testing of waveguides in chalcogenide glass*. PhD thesis, University of Alberta, 2004.

[121] Dianne Mitchell, Yifan Guo, and Vijay Sarihan. Methodology for studying the impact of intrinsic stress on the reliability of the electroless Ni UBM structure. *IEEE Transactions on components and packaging technologies*, 24(4):667–672, December 2001.

[122] S.W. Webb. Diamond retention in sintered cobalt bonds for stone cutting and drilling. *Diamond and Related Materials*, 8(11):2043–2052, November 1999.

[123] M. W. Moon, K. R. Lee, K. H. Oh, and J. W. Hutchinson. Buckle delamination on patterned substrates. *Acta Meterialia*, 52:3151–3159, 2004.

[124] John P. Barber, Donald B. Conkey, Jeffrey Ryan Lee, Neal B. Hubbard, Larry L. Howell, Dongliang Yin, Holger Schmidt, and Aaron R. Hawkins. Fabrication of hollow waveguides with sacrificial aluminum cores. *IEEE Photonics Technology Letters*, 17(2):363–365, February 2005.

[125] R. Bernini, S. Campopiano, and L. Zeni. Silicon micromachines hollow optical waveguides for sensing applications. *IEEE Journal of Selected Topics in Quantum Electronics*, 8:106–110, 2002.

[126] D. Bhusari, H. A. Reed, M.Wedlake, A. M. Padovani, S. A. B. Allen, and P. A. Kohl. Fabrication of air-channel structures for microfluidic, microelectromechanical, and microelectronic applications. *IEEE Journal of Microelectromechanical systems*, 10:400–408, September 2001.

[127] I. A. Weerasekera, S. I. Shah, D. V. Baxter, and K. M. Unruh. Structure and stability of sputter deposited b-tungsten thin films. *Applied Physics Letters*, 64(2):3231, 1994.

[128] H. Ma, A.K.-Y. Jen, and L.R. Dalton. Polymer-based optical waveguides: Materials, processing, and devices. *Advanced Materials*, 14(19):1339–1369, October 2002.

[129] The Microphotonics Center. Microphotonics: Hardware for the information age. Technical report, MIT, 2005.

[130] L. Jay Guo. Recent progress in nanoimprint technology and its applications. *Institute of Physics Applied Physics D*, 37:R123–R141, 2004.

[131] C.-Y. Chao and L. J. Guo. Polymer microring resonators fabricated by nanoimprint. *Journal of Vacuum Science and Technology B*, 20(6), 2002.

[132] Y. Huang, G. T. Paloczi, J. K. S. Poon, and A. Yariv. Bottom-up soft-lithographic fabrication of three-dimensional multilayer polymer integrated optical microdevices. *Applied Physics Letters*, 85(15):3005–3007, 2004.

[133] Ming Zhou. Low-loss polymeric materials for passive waveguide components in fiber optical telecommunication. *Optical Engineering*, 41(7):1631–1643, July 2002.

[134] Yurii A. Vlasov and Sharee J. McNab. Losses in single-mode silicon-on-insulator strip waveguides and bends. *Optics Express*, 12(8):1622 – 1631, April 2004.

[135] Marc J. Madou. *Fundamentals of Microfabrication: The Science of Miniaturization*. CRC Press, 2002.

[136] Michal Lipson. Overcoming the limitations of microelectronics using Si nanophotonics: solving the coupling, modulation and switching challenges. *Institute of Physics Journal of Nanotechnology*, 15:S622S627, 2004.

[137] Donald L. smith. *Thin-Film Deposition: Principles and Practice*. McGraw-Hill Professional, 1995.

[138] S.M. Sze. *Semiconductor Devices - Physics and Technology*. Wiley, 2001.

Appendix A

Microfabrication Principles

This chapter provides a brief overview of microfabrication techniques used in this work. Microfabrication, as the term suggests, is a manufacturing technology used to make integrated circuits. Over the years, the meaning of this term has extended to cover a vast spectrum of techniques used to make a variety of micro-scale devices like electronic, photonic, Micro-Electro-Mechanical Systems (MEMS), and microfluidic devices to name a few. A more detailed treatment can be found in [135].

A.1 Substrate selection

Currently, there is a great deal of interest in silicon-based photonics, for optical interconnects on and between integrated circuits [136]. This makes silicon a natural choice as an experimental platform for glass and polymer based photonics. Silicon serves as a mechanical support for the subsequent layers of material that we would use for fabricating our devices. Hence all that we are typically concerned with is the orientation of the silicon wafer and not its amount or type of doping. The silicon substrates used for this work were prime grade p-type $< 100 >$ orientation wafers having an rms surface roughness on the polished side of about 20 Å. Single crystal silicon wafers with $< 100 >$ orientation cleave along two perpendicular lines. A good cleave is of crucial importance in light coupling and Fabry-Perot loss measurement experiments.

A.2 Wafer Cleaning

The first step in any fabrication process is to clean the substrate of any dirt, grease from handling and other organic contaminants on the wafer surface. Typically, an acid Piranha etch is used for substrate cleaning. Another cleaning procedure, RCA clean, was also used in this work.

A.2.1 Piranha Clean

Acid Piranha is the trade name for a mixture of sulfuric acid and hydrogen peroxide. We use a 3:1 mixture by volume of sulfuric acid and hydrogen peroxide. This reaction is extremely exothermic and acid piranha reaches a temperature of about 120°C and increases its cleaning properties.

A.2.2 RCA clean

There are other cleaning procedures like RCA-1 clean. The name comes from the RCA laboratories where the recipe was developed. It is a 1:1:5 mixture by volume of ammonium hydroxide (NH_4OH), hydrogen peroxide (H_2O_2), and DI water (H_2O) respectively. This mixture is heated to about 75°C while cleaning the substrates. RCA-1 cleaning is revisited in Section 3.2.3.

A.3 Thin film deposition

Just as the starting point in hedge trimming is the growth of a hedge, in integrated device fabrication the first task is to deposit or grow the required material. Some crystalline materials can be grown through a method called epitaxy. However, this thesis is concerned with amorphous glass and polymer films. Typical deposition techniques are described in the following sections.

A.3.1 Spin coating

As the name suggests, this technique involves dissolving the desired material in an appropriate solvent and dispensing the solution onto a spinning substrate to obtain a thin film. This process normally requires an additional curing to get rid of the

solvent [137]. This is a cheap and simple method. We start by dispensing the solution on to the substrate carefully to get a bubble free puddle. After this, the substrate is spun at a slow speed to spread the solution over the entire substrate. The substrate is then accelerated to the desired final spin speed that corresponds to the film thickness desired.

The final stage is to drive away the solvent by heat-treating the substrate. This can

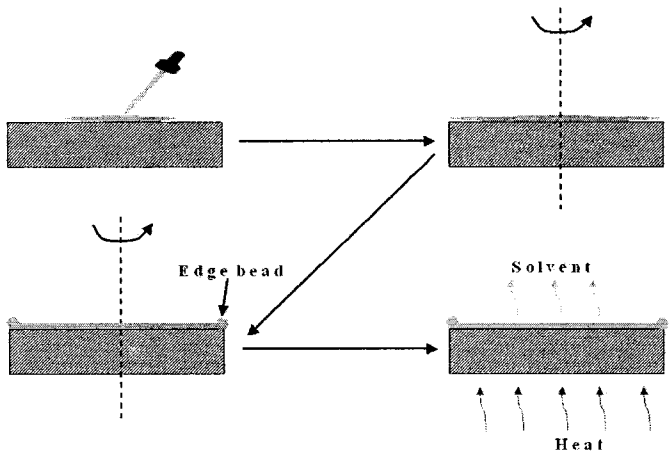

Figure A.1: Typical steps in Spin coating

be done in a controlled atmosphere or on an open hot plate. Final spin speed and the solvent evaporation rate are the crucial steps in determining the film thickness. Thicker films need careful curing procedures so as to avoid thermal shocks. Bubbles and sudden thermal shocks while curing can lead to pinholes and film peeling.

Edge beads are typically seen at the outer perimeter of top and bottom faces of the substrate. These can create problems especially in contact photolithography. They can easily be removed by an additional slow spin with a bead remover solution dispensed carefully at the edge of the substrate. Figure A.1 shows these basic steps. Some common problems associated with spin coating are shown in figure A.2

A.3.2 Thermal Evaporation

In this method the bulk material, called the target, is loaded in a suitable crucible, like a molybdenum boat, and evaporated using a resistance heater. There are other

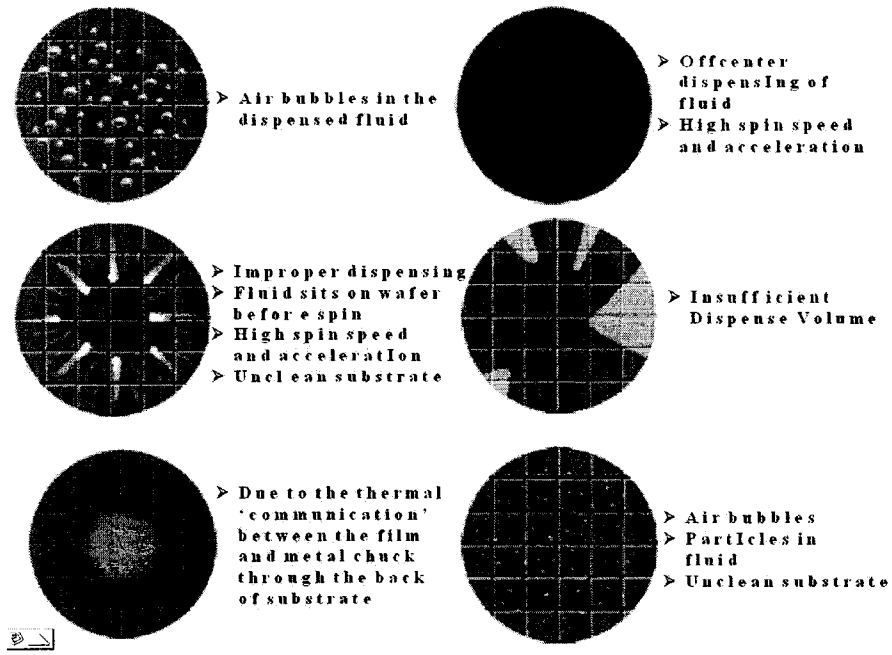

Figure A.2: Common problems observed in spin coating [5]

techniques for heating the target such as inductive and electron-beam heating. The evaporation is done in an evacuated chamber to increase the mean free path of the atoms/molecules coming off the target. The substrate to be coated is placed in the path of the vapor that emanates to obtain a thin film of the bulk material. Substrate rotation is used to increase the uniformity of the evaporated film while adhesion can be improved by substrate heating. A film thickness gauge is also incorporated to monitor the in-situ film thickness [137].

Thermal evaporation is a very good choice for the deposition of metals. Preserving the stoichiometry of a multi-component target tends to be difficult task. The target components need to have identical vapor pressures to conserve the composition in the film. Maintaining stoichiometry also requires well-controlled deposition rates. Sometimes co-evaporation [137](evaporating two materials at the same time) is used for multi-component films. Substrate heating during thermal evaporation can be used to improve the film density and adhesion to the substrate.

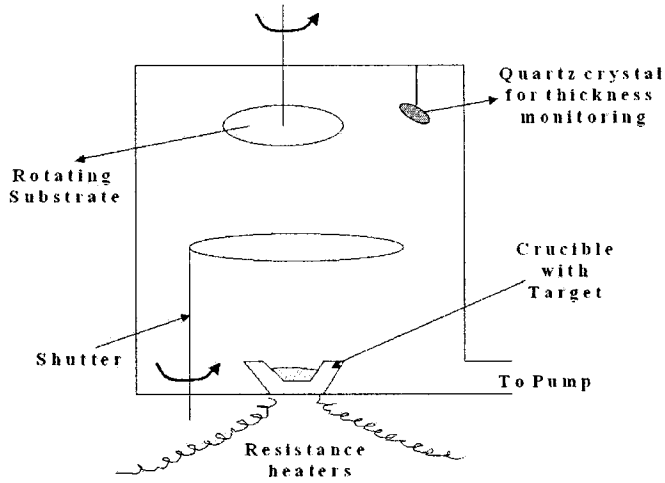

Figure A.3: Thermal evaporation [6]

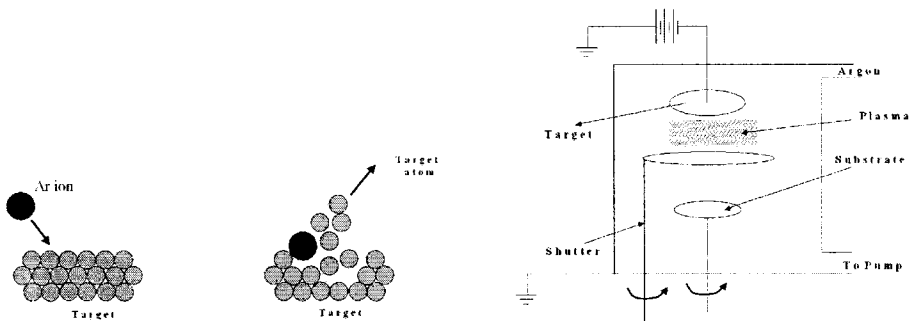

(a) Volatilization by sputtering

(b) Sputter evaporation

Figure A.4: Sputtering Illustration

A.3.3 Sputtering

Sputtering is different from thermal methods in that there is no melting of the target material. Ionizing a gas like Argon produces high-energy ions that strike the bulk target that ejects target atoms with enough energy to reach the substrate. Any material can be volatilized stoichiometrically by this method. Subsequent sputtered atoms that reach the film ideally have just enough energy to displace the surface atoms and bond nicely without causing sub-surface damage. Some of the surface atoms might be re-sputtered to produce films of good density. This reduced porosity means the atoms are tightly packed producing a compressive stress. These stresses will be revisited in Section 4.2.2 and a possible application will be discussed.

A.3.4 Pulsed Laser deposition (PLD)

This method uses laser pulses to volatilize a bulk target and typically produces films with the same stoichiometry as the target. This plume is collected onto the substrate kept at a short distance from the target. It is generally easier to obtain the desired film stoichiometry for multi-element materials using PLD than with sputtering. Unlike sputtering, PLD does not require a constant glow discharge, which can limit independent control of process parameters. The vacuum requirement is also relaxed for PLD. However depositing films on large-area substrates is a challenging task.

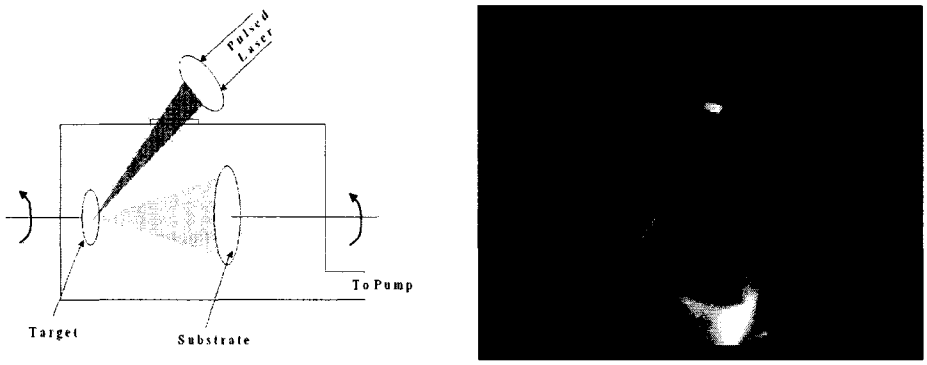

(a) Schematic of pulsed laser deposition setup (b) Pulsed laser deposition process

Figure A.5: Pulsed laser deposition

In the current work, both thermal evaporation and PLD were used to deposit thin films of chalcogenide glass. Sputtering was mainly used to deposit silver and gold films. Spin coating was used for obtaining this films of photo-resists and polymers.

A.4 Lithography

Lithography is a method of transferring desired patterns into a thin film. Traditionally, this is accomplished by selectively exposing a radiation sensitive material (i.e. a photo-resist) that has been spun on the desired substrate through a mask kept in close contact with the substrate. The photo-resist is then etched in an appropriate developer solution to obtain a replica of the mask pattern [6].

Depending on the exposure radiation source that is used there are a variety of

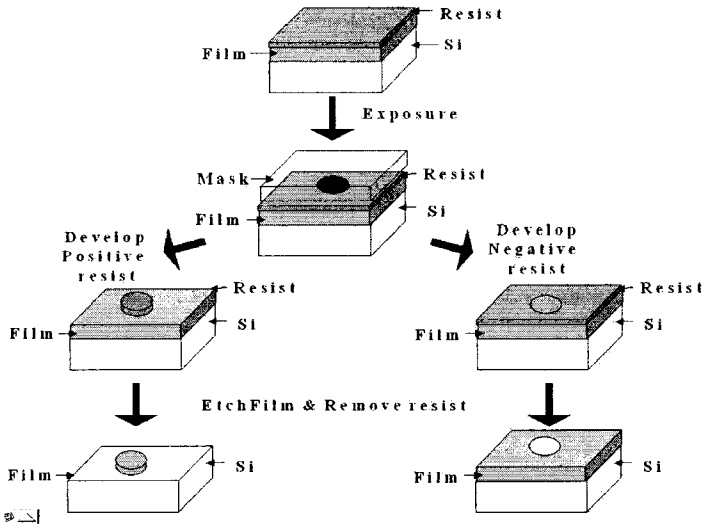

Figure A.6: Steps in Lithography

methods including photo (UV), deep ultraviolet (DUV), E-beam and X-ray lithography. However for the current work only the first three were employed. Novel lithography techniques like nano-imprint lithography have also been demonstrated recently [130]. Photolithography systems are also classified as contact, proximity and projection printing. As the names suggest, the classification is based on where the mask is placed with respect to the substrate and how the mask pattern is imaged on the resist. Contact photolithography was used in all cases for this work. The first step in lithography is spin coating the resist on to the desired sample. The substrate is then brought into intimate contact with a mask and aligned to the substrate. After UV or DUV exposure the exposed resist is developed. UV5 DUV resist was used for DUV lithography. The process involved spinning UV5 resist and baking at 135°C follwed by 2 seconds of DUV exposure though a mask. About 120 seconds developing in DUV resist developer produced very good features. In the UV lithography case which had bad contact, the resist used was HPR 504 which was baked at 120°C after spinning followed by 4 seconds UV exposure through a mask. The developing time was about 15 seconds.

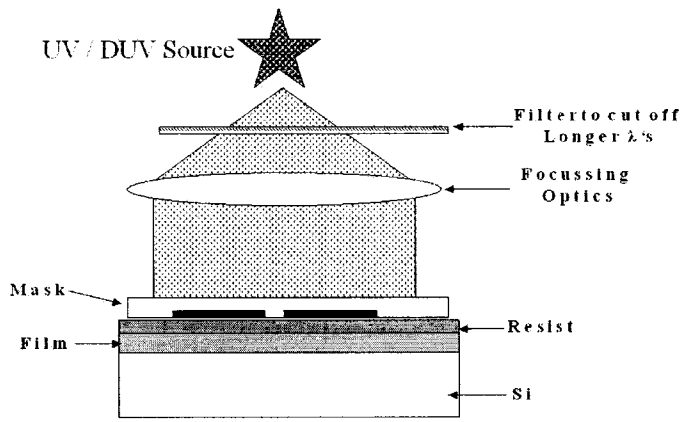

Figure A.7: Contact Lithography

A.4.1 Contact photolithography

The light source is normally a high intensity mercury arc lamp that produces several spectral lines; for example, the g-line and i-line have wavelength of 436 nm and 365 nm respectively. A filter is used to pass only the desired wavelength line. To obtain good transfer of dimensions from the mask to the resist, the light should not spread much when it passes through the features in the mask. But diffraction effects necessitate the use of lower wavelengths for smaller the mask features to be transferred accurately.

Hence, DUV sources at a wavelengths of 248 nm and lower allow for smaller feature sizes than normal UV. Each source required a different resist and developer. Alignment of the wafer with the mask and a good contact between the mask and the substrate is very important to obtain good features.

A.4.2 E-beam lithography

E-beam lithography (EBL) uses electron beam and focussing electron optics to pattern appropriate e-beam resists. In this work, Raith 150 EBL system was used. Raith 150 employs a vector scan method for writing sparse patterns while skipping unwritten areas. It allows control of exposure dose. Unlike contact photolithography, EBL is not diffraction limited and can pattern features as small as 20 nm. EBL limits the speed of fabrication but is an excellent tool for our work due to

the relative ease of incorporating design changes.

A.4.3 Photo/E-beam resists

Photoresists are radiation sensitive materials whose solubility in certain solvents changes drastically with radiation exposure. Photoresists consist of four ingredients: light sensitive polymer, solvent, sensitizers and additives. The light sensitive polymer undergoes polymerization or depolymerization when exposed to radiation. Solvent aids in making thin films of the resist. Sensitizer basically controls or modifies the chemical reactions during exposure. Additives are chemicals added to help in processing, for example, dyes. Resists respond to specific wavelengths. Some resists need to be chemically amplified for use at a different wavelength. Selection of a photoresist depends on the intended application. For example, if resists are later used as etch barriers then resist thickness and good adhesion plays a crucial role. Metal lift-off process requires resists that produce good under-cut after developing to aid in the removal of metal.

Photoresist adhesion is a major issue to consider while processing. A clean substrate is subjected to a dehydration bake. A thin coat of adhesion promoter like hexamethyldisilazane (HMDS) is applied prior to photoresist coating. After the photoresist is spun cast onto a substrate, a soft bake step is necessary to drive off the solvent. The solvent is necessary for coating the photoresist but if not removed completely by soft bake, it can absorb exposing radiation and thus affect the whole process. The temperatures and times of soft-bake are provided by the manufacturer. Over baking may result in the resist not responding to the radiation. The resist is exposed through a mask and a post-exposure bake is performed. This removes the standing wave patterns formed when the radiation reflects off the substrate and reaches the resist. Standing waves can affect the resolution and roughness of the resist sidewalls after developing. The last step is to develop the exposed resist in appropriate developer.

A.5 Etching

Etching is the term given to removal of material in microfabrication process. Two different approaches used in this work are described briefly in the sections below.

A.5.1 Wet Etching

Wet etching, as the name suggests, is a way to etch materials using chemicals in liquid form. Etch rate typically depends on the chemicals used and its temperature. This is an inexpensive process and does not require any sophisticated equipments. Wet etching causes undercutting due to the isotropy of the etch and accurate dimensional control is a tricky affair.

A.5.2 Dry Etching

Dry etching is used to obtain an anisotropic etch. Reactive Ion Etching (RIE) is one method of dry etching we used for etching polymers (refer to Chapter 5). In RIE, RF power is used to create a plasma from the gases pumped into the chamber. An electric field is applied to accelerate ions toward the surface of the samples that need to be etched [138].

Appendix B

Buckling Mask

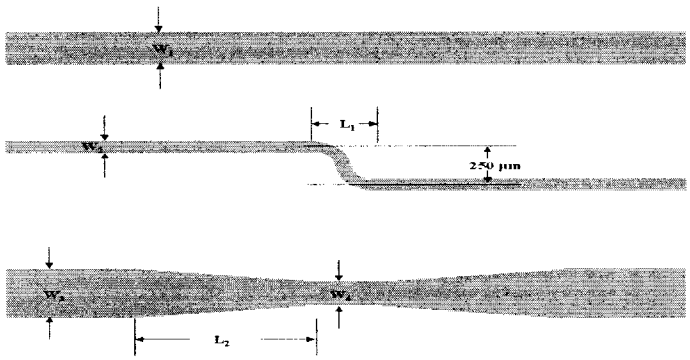

Figure B.1: Features on the Mask

Table B.1: Mask features and dimensions

Section	Waveguides		S bend			Taper		
	W_1 µm	#	W_2 µm	L_1 µm	#	W_3 µm/ W_4 µm	L_2 µm	#
I	10, 20, 40, 60, 80	5 each	10, 20, 40, 60, 80	1000	5 each	80 / 10 & 80 / 20	5000	5 each
II	- do -	- do -	- do -	500	- do -	- do -	- do -	- do -
III	- do -	- do -	- do -	250	- do -	- do -	- do -	- do -

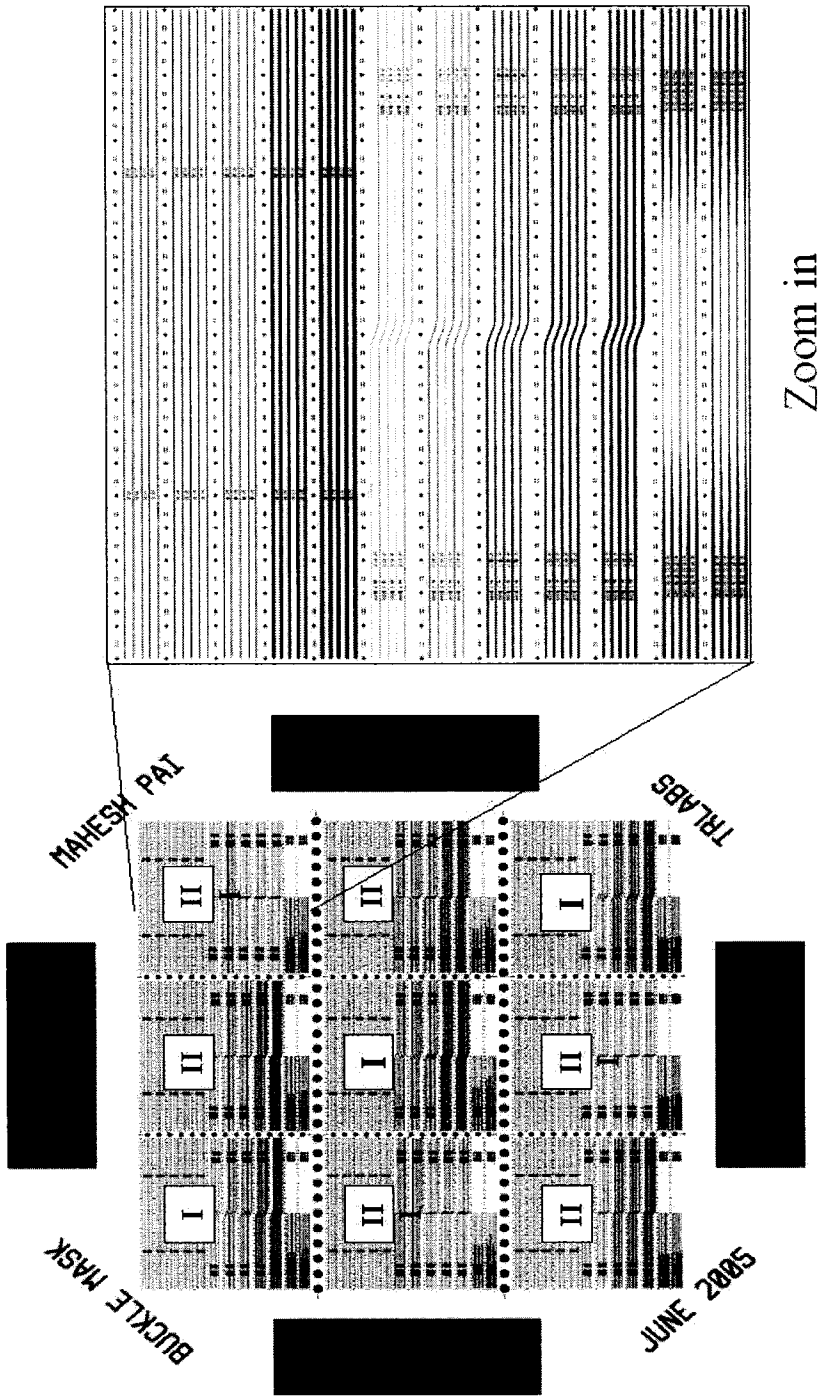

Figure B.2: Buckling Mask and a Zoom in on one of the sections